Electrodeposition of Nanomaterials: Examination of Growth at the Atomic Interfaces

by

Nhi N. Bui

(Under the Direction of John Lewellen Stickney)

Abstract

The electrochemical formation of ZnS nanofilms has been demonstrated using a derivative of the Electrochemical Atomic Layer Deposition (E-ALD), called Potential Pulse Atomic Layer Deposition (PP-ALD). Similar to E-ALD, PP-ALD focuses on the use of underpotential deposition – an electrochemical surface-limited reaction, to form materials one atomic layer at a time. By changing the potentials instead of exchanging solutions between cycles, PP-ALD can reduce the deposition time. The effects of pHs, potentials, pulse durations, intermediate pulses, and annealing temperatures were investigated to optimize the deposition conditions. Surface-limited reaction was achieved for Zn^{2+} and thiosulfate precursors. The linear correlation between the number of deposition cycles and the thickness of the deposits suggested that the growth rate can be controlled by PP-ALD. EPMA, SEM, ellipsometry, Photoelectrochemistry (PEC), and XRD were used to characterize the thin film deposits. The chemistry for growing ZnS has opened routes to forming similar compounds such as SnS and CuS, and eventually can be combined with Cu_2Se and SnSe to form a superlattice structure of $Cu_2ZnSn(S,Se)_4$– a PV absorber materials.

The atomic-level processes occurring during the electrodeposition of germanene were investigated using the Electrochemical Scanning Tunneling Microscopy and *in*

situ Surface-enhanced Raman Spectroscopy. In potential range between -0.7 V and -0.85 V (vs Ag/AgCl), Ge is first deposited in the face-center-cubic region of the Au reconstruction. At -0.9 V, Ge domains merge together to form a sheet, expelling some remaining Herringbone lines and form new Au islands that are also covered with Ge layer. Germanene domains are found to be 2-3 nm in size. Within a domain wall, honeycomb structure characteristic of germanene was observed. Formation of a second layer occurs at -1.0 V. An 8 mW 780 nm laser with 3.1 µm spot size can induce surface crystallization. The first layer of germanene forms a Raman peak at 200 cm^{-1}, whereas the second layer is at 295 cm^{-1}. It is proposed here that interaction with the Au substrate had induced some strain to the vibration mode of the first layer, shifting it to a lower energy compared to the more liberated second layer. A possible exfoliation of the deposit due to hydrogen evolution at potential more negative than -1.0 V was noticed. More basic pH has resulted in higher Raman intensity. During a cycle of Bait and Switch E-ALD, the first Te deposit is found to go underneath the Ge layers and bonds with Au substrate.

INDEX WORDS: Electrodeposition, Electrochemical Atomic Layer Deposition (E-ALD), Potential Pulse Atomic Layer Deposition (PP-ALD), Underpotential deposition (UPD), ZnS, CZTS, Cyclic Voltammetry, Photoelectrochemistry (PEC), EPMA, ellipsometry, SEM, XRD, Germanene, 2D materials, Electrochemical Scanning Tunneling Micropscopy (EC-STM), *in situ* Surface-Enhanced Raman Spectroscopy (SERS)

Electrodeposition of Nanomaterials: Examination of Growth at the Atomic Interfaces

by

Nhi N. Bui

B.A. Chem, Knox College, 2013

A Dissertation Submitted to the Graduate Faculty
of The University of Georgia in Partial Fulfillment
of the
Requirements for the Degree

Doctor of Philosophy

Athens, Georgia

2017

Electrodeposition of Nanomaterials: Examination of Growth at the Atomic Interfaces

by

Nhi N. Bui

Approved:

Major Professor: John Lewellen Stickney

Committee: Tina T. Salguero
Jeffrey L. Urbauer

Electronic Version Approved:

Suzanne Barbour
Dean of the Graduate School
The University of Georgia
August 2017

Dedication

This work is dedicated to my husband, whose constructive criticism and immense support have helped shape and refine many ideas and directions through my conversation with him. Thank you for being such a special colleague, supporter, and friend.

I also would like to thank my parents for giving me the opportunity to study abroad. Their unwavering faith and assurance have allowed me to keep moving forward and believe in the value of resilience and hard-work. To my in-laws, I am deeply grateful for their unconditional love and support. Many weekends when I come home exhausted, the warmth of family gathering and home-cooked meals have made all my tiredness disappeared.

Acknowledgments

To my advisor, Professor John Stickney: I still remembered the day when I sat in your office, worrying that I will not be allowed to join your group. Having a rough and confusing first semester has instilled so much doubt about whether I should continue to pursue the advance degree. Your kind words have given me hope to shake off any anxiety and stay around. You told me that the amount of effort I put to my work will determine how much I get out. Many times had these words played in my head when I contemplated over unsuccessful experiments. Thank you for giving me the opportunity to work in your lab, being your student, and learning about the important skills in research and instrument troubleshooting. I am forever grateful for your guidance, your patience, your cheerful personality, and especially your genuine dedication to the personal advancement of students.

I also would like to thank Dr. Tina Salguero and Dr. Jeffrey Urbauer for their invaluable time serving as my committee members. Their high standards have continuingly challenged me, helping me to improve myself and be prepared for my new adventures in the work life after grad school.

I am also deeply thankful for the instructions and companionship from former group members. I very much miss the pleasant environment when many of you were around. The lab has never been the same without you. My special thanks to Maria who has spent the entire month speed-training me on the EC-STM; to Justin for his amiable personality and enthusiasm on teaching me about XRD; and to Chu for his endless lessons about science, discipline, building instruments, writing software, and how to critically analyze any problem. Your mere presences have made all the efforts worth it and working late in the lab or over the weekends did not feel as lonely.

Table of Contents

Page

Acknowledgments v

Chapter

1 Introduction and Literature Review 1

1.1 Atomic layer deposition (ALD) and Electrochemical Atomic Layer Deposition (E-ALD) 1

1.2 Materials for photovoltaics application 2

1.3 Potential Pulse Atomic Layer Deposition (PP-ALD) 3

1.4 Cyclic voltammetry coupling with a flow cell system 4

1.5 2D materials and germanene 5

1.6 EC-STM and *in situ* SERS 6

References 8

2 Potential Pulse Atomic Layer Deposition (PP-ALD): Electrodeposition of ZnS Nanofilms 12

2.1 Abstract 13

2.2 Introduction 13

2.3 Experimental 16

2.4 Results and Discussion 18

2.5 Conclusion 38

2.6 Acknowledgments 39

References 40

3 An EC-STM Study of Germanene Growth on Au(111) from Aqueous Solution, pH 9.0 46
3.1 Abstract 47
3.2 Introduction 48
3.3 Experimental 50
3.4 Results and Discussion 51
3.5 Conclusion 68
3.6 Acknowledgments 71
References 72
4 Surface Enhanced Raman Spectroscopic Study of Germanene Layers Formed by Electrodeposition 79
4.1 Abstract 80
4.2 Introduction 81
4.3 Experimental 83
4.4 Results and Discussion 87
4.5 Conclusion 100
4.6 Acknowledgments 102
References 103
5 Conclusion and Future Studies 115
References 121

Chapter 1

Introduction and Literature Review

1.1 Atomic layer deposition (ALD) and Electrochemical Atomic Layer Deposition (E-ALD)

In nanomaterials fabrication, the technique of ALD has become increasingly important due to its principle to control the thickness precisely at the atomic level.[1] ALD is generally thought of as a gas-phased methodology that takes advantage of surface-limited chemical reaction to sequentially deposit a single layer of material at a time by exchanging gas-phased chemical precursors. With application that requires precise control of the deposition process, ALD becomes an ideal method to grow thin films.

The invention of the electrochemical variant of ALD originated from this group 27 years ago. Since then, research from the group has been focusing on developing and optimizing multiple chemical systems, such as binary compounds from group II-VI, III-V, IV-VI and other quaternary compounds.[2–9] These materials have applications in various fields such as photovoltaics, fuel cells, thermoelectrics, catalysts, etc. E-ALD is an ALD process in the liquid phase of an electrochemical environment.

The fundamental principle behind E-ALD is the use of the electrochemical surface limited reactions called underpotential deposition (UPD). UPD is a phenomenon where one element would deposit on another at a potential prior to (under) that needed for it to deposit on itself.[2–9] This happens due to the favorable change in free energy associated with compound formation or alloy with the surface. Depending on the element and the type of substrate, the UPD behavior will vary. To grow a specific compound on a substrate, the electrochemistry of individual element is investigated

through cyclic voltammetry. Once the optimal potential ranges are identified, thicker films can be made and characterized by many techniques such as ellipsometry, EPMA, SEM, EDXA, XRD, Raman, photochemistry, etc. These methods allow further optimization of the growing process, with which a slight tweak in condition can be applied to improve the film quality. The goal is to achieve good film quality while also be able to finely control the thickness of the deposit.

1.2 Materials for photovoltaics application

Incentives to pursue renewable technology such as solar cells have been growing strong and clear. Besides crystalline silicon technology, there are many budding generations of photovoltaics that promise improvement to both the film's quality and raw material resources. Thin film solar cells (TFSC) is an example of the next generation solar cells that use less amount of the materials to lower the production cost. E-ALD would be an applicable method to grow thin layer absorber of different compounds. There were some former works on CIGS and CdTe; however, some of these elements are quite toxic (Ga, Te) and not very abundant (In, Te). The motivation behind TFSC is also about selecting materials that are cheap, earth-abundant and environmental friendly. These factors lead to the pursue of growing materials such as $Cu_2ZnSn(S,Se)_4$ (CZTS), CuSe, SnS or SnSe. Since 2009, TFSCs based on CZTS-related compounds have attracted a great deal of attention as a potential low-cost alternative to the conventional absorber materials in photovoltaics.[10–15] It exhibits an optical band gap energy of 1.4-1.5 eV and a high absorption coefficient.

The growth of CZTS through E-ALD can be broken down into different sets of binary compounds such as ZnS, SnS, and CuSe. Each of these compounds would need to be optimized separately before they were to combine together into the final quartenary structure. Standing on its own as a binary compound, ZnS is a *n*-type semiconductor with a wide direct band gap in the UV range (3.5 - 3.9 eV at room tempera-

ture). With such large band gap, it has the advantage of reducing the window absorption losses, hence increases the circuit current of solar cells, making it an attractive material to be used as a window layer in heterojunction photovoltaic cells. In addition, ZnS can also be used in light emitting diodes in the blue ultraviolet region, antireflection coating, photosynthetic coatings, electroluminescent opto-electronic device, multilayer dielectric filters, sensors and lasers, and α - particle detector.

1.3 Potential Pulse Atomic Layer Deposition (PP-ALD)

To grow materials for photovoltaic application, the challenge with E-ALD is that involves multiple rinsing steps and could compromise the speed of growing micron thick films. To accommodate for speed, a variant of E-ALD was developed and called Potential Pulse Atomic Layer Deposition (PP-ALD).[16,17] Its principle is based on changing the potential rather than exchanging solutions between cycles, in order to reduce the deposition time. The chemistry of the elements is more complicated when deposited with PP-ALD, as compared to E-ALD, since all the precursors are to be prepared in the same chemical batch and only a single solution is to flow through the deposition cell. This requirement could greatly limit the choice of potential precursors since they tend to precipitate or accumulate over time if combined together. For certain chemistry to occur, the inclusion of additives is necessary. However, they could complicate the chemistry of an otherwise simple system. In the case of growing ZnS, precursor for Zn^{2+} could come from ZnO, $ZnSO_4$ or $ZnCl_2$. For S, several potential precursors are thiosulfate, thiourea, or sulfide with the use of complexing agent such as EDTA, triethanolamine, hydrazine, etc.

Chapter 2 is about the electrodeposition of ZnS nanofilms by PP-ALD. A controlled growth was achieved by investigating the effects of pH, potential, and pulse duration. The chemistry of growing ZnS can eventually be combined with those for Cu_2S and SnSe to form the superlattice structure of CZTS.

1.4 Cyclic voltammetry coupling with a flow cell system

Over the years, the set up for the electrochemical flow cell has been improved to better facilitate the deposition process. A typical set up consists of multiple solution bottles in which separated elemental precursors are prepared. These bottles mimic the gas tanks, storage of gas precursors, used in a conventional ALD system. The bottles are connected to a valve block which is a computer-controlled programmable system that determines which solution would flow through the deposition cell. After passing through the cell, solution would be collected into a waste bottle. A future improvement to this system could be a design to recycle the solutions where the majority of the species remained unused. There is also a peristaltic pump that has manually-controlled varied pump speed. In the past, the pump speed was designed to be electronically controlled and the effect could be more or less important depending on the specific chemistry of a selected system. The deposition cell also went through many design changes. In the past, when the auxiliary electrode was made by ITO, significant reduction at the working electrode would simultaneously oxidize the auxiliary, and vice versa. Due to limited electrochemical stability of ITO, such high current could damage the electrode and causes it to stop working. The current design employed Au as a more dependable electrode. The Au wire is flattened into an S-shape that positions right on top of the substrate to help prevent IR drop that could occur if the distance is large. All solution bottles are purged with nitrogen gas before each experiment to exclude oxygen. A pressurized bottles system was designed to help with better sealing, preventing the gas leakage through connections and tubing, reducing the need of purging for a prolong period, and producing a smoother flow of solution.

The interpretation of cyclic voltammetry data (CVs) is generally considered difficult due to a multitude of possibilities that can occur at the electrode surface. The coupling of CVs with the flow cell set up makes it a powerful tool to mitigate compli-

cation and allows better analysis of a complex electrochemical system. For example, blank solution can be exchanged during the investigation process while having full potential control of the surface. Removal of some active species results in a better-controlled analytical study of the mechanism of some chemical processes.

1.5 2D MATERIALS AND GERMANENE

The topic of 2D materials has become increasingly more popular in the field of material sciences. Their unique physical, electrical and chemical properties have made them attractive for application in the electronic field. With the size of the transistor continues to shrink, the demand for new materials, device design integration continues to grow and become more urgent. The search for and growth of new materials promise further improvement to the innovation process. Majority of 2D materials come from an existing 3D crystal. Some examples of those include MoS_2, WS_2, hBN, etc.[18–25] Exfoliation of such structures would result in a layered material counterpart. These materials typically consist of a layer of transition metal being sandwiched between two layers of chalcogenides. On the other hand, group IV elements including C, Si, Ge and Sn have been thought to form 2D materials analogous of graphene.[1] Silicene and Germanene have become more popular recently. The experimental results on the making of germanene are still limited. In general, germanene are formed in the Ultra-high Vaccum system (UHV) via molecular beam epitaxy (MBE). To grow germanene via electrodeposition is an interesting subject for investigation.

The electrodeposition of Ge from aqueous solution has been known to be challenging since its chemistry seems to stop after a few monolayer. A few years ago, research from this group has come up with a unique E-ALD cycle that could be used to induce the growth of Ge more than its natural limit. The method is called Bait & Switch, where Te was used as a bait for Ge to grow an extra layer, after which Te would be stript off leaving the new layer of Ge on top. Repetition of this cycle

would allow the growth of thicker Ge deposition. Characterization of these films of Ge revealed an amorphous material with the characteristic Raman peak at 270 cm^{-1}. The behavior of Ge has led to a more fundamental question such as why its chemistry would naturally stop after a few monolayers. With such a thin layer could something like germanene was forming on the surface? Further studies were needed to answer these questions.

1.6 EC-STM AND *in situ* SERS

Characterization of the germanene system requires the technique to be surface sensitive, since a few layers of Ge is expected to be less than 1nm in thickness. Electrochemical Scanning Tunneling Spectroscopy (EC-STM) is a technique that allows *in situ* probing into the dynamic electrodeposition process. The instrumental set up consists of an electrochemical cell filled with solution that covers an Au bead substrate. The scanning head controls the potential between the tip and the substrate while another a complementary system controls the potential between the substrate and its auxiliary electrode. This set up allows the imaging process to proceed simultaneously while the deposition occurs. Preparation of the Au bead single crystal requires much attention and dedication. The H_2O_2 flame has to be carefully adjusted to slowly melt the bead, raising the liquid level up and down around the facet level, in order to form a flat uniform Au(111) facet. The Au bead is attached to a flat Au plate with the Au(111) facet facing up, hanging by a slim wire. This allows the melting process to occur only on the bead with minimal deformation of the Au plate. With the bead facing upward, the STM tip is positioned normal to the facet surface for the engagement of the tip to occur successfully. The process to make the tip for each imaging attempts has been well-documented and is described in details in the chapters about germanene.

Surface-enhanced Raman Spectroscopy has been considered a powerful probe used for detecting the vibrational signal of very minute features.[26–31] The enhancement effect could come from both the localized plasmon and polariton. The irregularity of the surface creates some large fields that allow photon to interact more strongly and for a prolong period of time with the surface, resulting in the enhancement of the signal. For a system that is only one nm thick, such as Ge electrodeposition, an exponential increase in the photon output is necessary. *In situ* SERS were set up with a newly designed flow cell designated for spectroscopy experiments. The concept of a regular flow cell is kept with some modification to allow light penetration and size-fitting in a standard microscope.

References

(1) Johnson, R. W.; Hultqvist, A.; Bent, S. F. A brief review of atomic layer deposition: from fundamentals to applications. *Materials Today* **2014**, *17*, 236–246.

(2) Gregory, B. W.; Stickney, J. L. Electrochemical Atomic Layer Epitaxy (ECALE). *Journal of Electroanalytical Chemistry* **1991**, *300*, 543–561.

(3) Villegas, I.; Stickney, J. L. Preliminary Studies of Gaas Deposition on Au(100), (110), and (111) Surfaces by Electrochemical Atomic Layer Epitaxy. *Journal of the Electrochemical Society* **1992**, *139*, 686–694.

(4) Colletti, L. P.; Teklay, D.; Stickney, J. L. Thin-Layer Electrochemical Studies of the Oxidative Underpotential Deposition of Sulfur and Its Application to the Electrochemical Atomic Layer Epitaxy Deposition of Cds. *Journal of Electroanalytical Chemistry* **1994**, *369*, 145–152.

(5) Colletti, L. P.; Stickney, J. L. Optimization of the growth of CdTe thin films formed by electrochemical atomic layer epitaxy in an automated deposition system. *Journal of the Electrochemical Society* **1998**, *145*, 3594–3602.

(6) Venkatasamy, V.; Jayaraju, N.; Cox, S. M.; Thambidurai, C.; Mathe, M.; Stickney, J. L. Deposition of HgTe by electrochemical atomic layer epitaxy (EC-ALE). *Journal of Electroanalytical Chemistry* **2006**, *589*, 195–202.

(7) Venkatasamy, V.; Jayaraju, N.; Cox, S. M.; Thambidurai, C.; Stickney, J. L. Studies of Hg((1-x))Cd(x)Te formation by electrochemical atomic layer deposition and investigations into bandgap engineering. *Journal of the Electrochemical Society* **2007**, *154*, H720–H725.

(8) Kim, J. Y.; Stickney, J. L. Ultrahigh vacuum surface studies of the electrochemical atomic layer deposition of indium telluride on n-type GaAs(100). *Journal of Physical Chemistry C* **2008**, *112*, 5966–5971.

(9) Gebregziabiher, D. K.; Kim, Y. G.; Thambidurai, C.; Ivanova, V.; Haumesser, P. H.; Stickney, J. L. Electrochemical atomic layer deposition of copper nanofilms on ruthenium. *Journal of Crystal Growth* **2010**, *312*, 1271–1276.

(10) Nakada, T.; Hongo, M.; Hayashi, E. Band offset of high efficiency CBD-ZnS/CIGS thin film solar cells. *Thin Solid Films* **2003**, *431*, 242–248.

(11) Sarswat, P. K.; Free, M. L.; Tiwari, A. A Study of Increased Resistivity of FTO Back Contact for CZTS Based Absorber Material Grown by Electrodeposition-Annealing Route. *Transparent Conducting Oxides and Applications* **2011**, *1315*, 83–88.

(12) Khalil, M. I.; Bemasconi, R.; Magagnin, L. CZTS layers for solar cells by an electrodeposition-annealing route. *Electrochimica Acta* **2014**, *145*, 154–158.

(13) Tan, K.; Lin, P.; Tan, J. Y.; Wu, L. S.; Wang, G.; Jin, S. P.; Lin, Y. X. The film morphology evolution and growth simulation of Cu2ZnSnS4 (CZTS) solar cells during electrodeposition. *2015 Ieee 42nd Photovoltaic Specialist Conference (Pvsc)* **2015**.

(14) Tlemcani, T. S.; Benamar, E.; El Moursli, F. C.; Hajji, F.; Edfouf, Z.; Taibi, M.; Labrim, H.; Belhorma, B.; Aazou, S.; Schmerber, G.; Bouras, K.; Sekkat, Z.; Dinia, A.; Ulyashin, A.; Slaoui, A.; Abd-Lefdil, M. Deposition Time Effect On The Physical Properties Of Cu2ZnSnS4 (CZTS) Thin Films Obtained By Electrodeposition Route Onto Mo-coated Glass Substrates. *Proceedings of the Emrs 2015 Spring Meeting - Symposium C on Advanced Inorganic Materials and Structures for Photovoltaics* **2015**, *84*, 127–133.

(15) Shin, S.; Park, C.; Kim, C.; Kim, Y.; Park, S.; Lee, J. H. Cyclic voltammetry studies of copper, tin and zinc electrodeposition in a citrate complex system for CZTS solar cell application. *Current Applied Physics* **2016**, *16*, 207–210.

(16) Czerniawski, J. M.; Stickney, J. L. Electrodeposition of In_2Se_3 Using Potential Pulse Atomic Layer Deposition. *Chemistry of Materials* **2016**.

(17) Czerniawski, J. M.; Perdue, B. R.; Stickney, J. L. Potential Pulse Atomic Layer Deposition of Cu_2Se. *Chemistry of Materials* **2016**, *28*, 583–591.

(18) Editorial As thin as it gets. *Nature Materials* **2017**, *16*, 155–155.

(19) Handschin, C.; Makk, P.; Rickhaus, P.; Liu, M. H.; Watanabe, K.; Taniguchi, T.; Richter, K.; Schonenberger, C. Fabry-Perot Resonances in a Graphene/hBN Moire Superlattice. *Nano Letters* **2017**, *17*, 328–333.

(20) Jia, Y. L.; Wan, H. Q.; Chen, L.; Zhou, H. D.; Chen, J. M. Facile synthesis of three dimensional MoS2 porous film with high electrochemical performance. *Materials Letters* **2017**, *195*, 147–150.

(21) Khan, A. F.; Down, M. P.; Smith, G. C.; Foster, C. W.; Banks, C. E. Surfactant-exfoliated 2D hexagonal boron nitride (2D-hBN): role of surfactant upon the electrochemical reduction of oxygen and capacitance applications. *Journal of Materials Chemistry A* **2017**, *5*, 4103–4113.

(22) Molle, A.; Goldberger, J.; Houssa, M.; Xu, Y.; Zhang, S. C.; Akinwande, D. Buckled two-dimensional Xene sheets. *Nature Materials* **2017**, *16*, 163–169.

(23) Moore, C.; Movia, D.; Smith, R. J.; Hanlon, D.; Lebre, F.; Lavelle, E. C.; Byrne, H. J.; Coleman, J. N.; Volkov, Y.; McIntyre, J. Industrial grade 2D molybdenum disulphide (MoS2): an in vitro exploration of the impact on cellular uptake, cytotoxicity, and inflammation. *2d Materials* **2017**, *4*.

(24) Schue, L.; Stenger, I.; Fossard, F.; Loiseau, A.; Barjon, J. Characterization methods dedicated to nanometer-thick hBN layers. *2d Materials* **2017**, *4*.

(25) Zheng, C. X.; Zhang, Q. H.; Weber, B.; Ilatikhameneh, H.; Chen, F.; Sahasrabudhe, H.; Rahman, R.; Li, S. Q.; Chen, Z.; Hellerstedt, J.; Zhang, Y. P.; Duan, W. H.; Bao, Q. L.; Fuhrer, M. S. Direct Observation of 2D Electrostatics and Ohmic Contacts in Template-Grown Graphene/WS2 Heterostructures. *ACS Nano* **2017**, *11*, 2785–2793.

(26) Vanduyne, R. P.; Haushalter, J. P. Surface-Enhanced Resonance Raman-Spectroscopy of Adsorbates on Semiconductor Electrode Surfaces - Tris (Bipyridine) Ruthenium(II) Adsorbed on Silver-Modified N-GaAs(100). *Journal of Physical Chemistry* **1983**, *87*, 2999–3003.

(27) Zou, S. Z.; Weaver, M. J. Surface-enhanced Raman scattering of ultrathin cadmium chalcogenide films on gold formed by electrochemical atomic-layer epitaxy: Thickness-dependent phonon characteristics. *Journal of Physical Chemistry B* **1999**, *103*, 2323–2326.

(28) Gichuhi, A.; Boone, B. E.; Shannon, C. Resonance Raman scattering and scanning tunneling spectroscopy of CdS thin films grown by electrochemical atomic layer epitaxy - thickness dependent phonon and electronic properties. *Journal of Electroanalytical Chemistry* **2002**, *522*, 21–25.

(29) McFarland, A. D.; Young, M. A.; Dieringer, J. A.; Van Duyne, R. P. Wavelength-scanned surface-enhanced Raman excitation spectroscopy. *Journal of Physical Chemistry B* **2005**, *109*, 11279–11285.

(30) Rath, S.; Sen, S.; Nozaki, S.; Tona, M.; Ohtani, S.; Jain, K. P. Detection of Low-Density Ge Nanoparticles Using Surface-Enhanced Raman Spectroscopy. *Advanced Science Letters* **2009**, *2*, 377–380.

(31) Carim, A. I.; Gu, J. S.; Maldonado, S. Overlayer Surface-Enhanced Raman Spectroscopy for Studying the Electrodeposition and Interfacial Chemistry of Ultrathin Ge on a Nanostructured Support. *ACS Nano* **2011**, *5*, 1818–1830.

Chapter 2

Potential Pulse Atomic Layer Deposition (PP-ALD): Electrodeposition of ZnS Nanofilms [1]

[1] Bui, N.; Cheng, W.; Mubeen, S.; Stickney, J. To be submitted to ACS journal Chemistry of Materials.

2.1 Abstract

Control of growth at the atomic level is desirable for the formation of high-quality thin films. The present study focuses on the electrochemical growth of nanofilms of ZnS, a compound semiconductor with a wide direct band-gap of 3.5 - 3.9 eV. Conventional electrodepostion of ZnS is difficult, partially because of the material's low hydrogen overpotential. The method used in this study is referred to as Potential Pulse Atomic Layer Deposition (PP-ALD) - a variant of Electrochemical Atomic Layer Deposition (E-ALD). PP-ALD uses a single solution containing precursors to each element, but as with ALD, makes use of surface limited reactions to control stoichiometry and growth. Cyclic voltammetry (CV) was performed in solutions of ZnO and $Na_2S_2O_3$, to investigate the electrochemistry of Zn^{2+} and ${S_2O_3}^{2-}$ ions. ZnS deposition was then studied in a solution containing both ions. The effects of pH, potential, and pulse duration on the film properties were investigated so as to optimize deposition conditions. The composition, morphology, thickness, structural and optical properties of the ZnS nanofilms were characterized using EPMA, SEM, ellipsometry, XRD and photoelectrochemistry (PEC).

2.2 Introduction

Electrochemical atomic layer deposition (E-ALD) has been used to form a variety of compound semiconductors and metallic nanofilms over the last 27 years. Its main principle has been to use surface-limited reactions to obtain layer by layer growth.[1–3] Electrochemical surface-limited reactions are referred to as underpotential deposition (UPD), a phenomenon where one element deposits on a second at a potential prior to that needed to deposit the element on itself, as a result of the free energy of formation of a surface compound or alloy.[1,2,4] By using electrochemical reactions, it is possible to form many materials without the usual high temperatures and annealing.

For a photovoltaic (PV) production method to be competitive, it must be scalable, inexpensive, and fast. Electrodeposition could be an applicable process if it can also provide control over deposit structures and composition. In these aspects, E-ALD has been considered as an electrochemical methodology that provides good control, however, with the drawback of a long deposition time. Its process involves alternation of solutions for the deposition of every compound layer, making the procedure "tedious" for the growth of the micron-thick absorber-layer films needed for photovoltaic application. The high volume production of PV is thus a challenge to the present E-ALD.

The present report concerns a variant of E-ALD intended to increase the deposition rate, while maintaining the use of surface limited reactions for control over deposition structure and composition. While E-ALD was based on each atomic layer being formed from its precursor solution at an underpotential, thus requiring the alternation of the solutions with each compound monolayer, PP-ALD is based on the use of a single solution, much as co-deposition is, but with the addition of potential changes at time scales consistent with the growth of compound monolayers. Co-deposition, on the other hand, is based on a single solution but with the choice of a single potential or current density for deposition. PP-ALD has been previously demonstrated in studies to grow Cu_2Se and In_2Se_3.[4,5]

The concept of PP-ALD was inspired by Sequential Monolayer Deposition (SMD) – a method initially proposed by Sailor et al.[6] SMD added control over the composition and thickness to a traditional codeposition by scanning the potential to oxidize off any excess bulk element. The result is a facile process in which only monolayer amount of material is deposited per cycle. Another versatile deposition style credited for the creation of PP-ALD is pulsed electrodeposition; and there have been many of its versions proposed and investigated.[7–25] The central idea is to add some time to replenish the depletion layer and prevent the formation of undesirable morphologies.

Providing the atomic layer control on top of these benefits is what PP-ALD offers. The present study exemplifies the formation of ZnS based on the principle of PP-ALD to form an atomic layer by layer growth deposit. PP-ALD gives a range of parameters that can be optimized to obtain high quality films, such as number of pulses, variation of cathodic, anodic, and intermediate potentials, and pulse duration.

What makes the implementation of PP-ALD harder than E-ALD is its requirement for all the components to be prepared in the same batch. In E-ALD, precursors can be separated into different bottles, thus avoid any complexity through potential chemical interaction among the elements prior to the deposition. In pulse electrodeposition, however, that factor becomes important and has to be taken into account when selecting precursors and studying their chemistry. A simple sulfur source such as S^{2-} could not be used without complexing agents because it would simply precipitate with Zn^{2+}. This led us to examine other sulfur precursors such as thiosulfate, thiourea, or formamidine disulfide. The present study investigated the use of Zn and thiosulfate as precursors for the PP-ALD of ZnS.

ZnS is a semiconductor with a wide direct band-gap in the UV range of 3.5 - 3.9 eV at 300 K.[26,27] Unlike CdS with limiting band-gap energy of 2.4-2.5 eV,[28] ZnS has the advantage of reducing the window absorption losses, making it an attractive material to be used as a window layer in photovoltaics. High volume production of ZnS in place of CdS buffer layer in CIS/CIGS and CZTS devices is deemed to be more environmental friendly.[29] In addition, the chemistry for growing ZnS can eventually be combined with those for Cu_2Se_2 and SnS to form a superlattice structure of $Cu_2ZnSn(S,Se)_4$ (CZTS) - a PV absorber material. Containing nontoxic earth-abundant elements such as Cu, Zn and Sn, CZTS offers the opportunity of low cost production as compared to using In and Ga in CIGS. The kesterite compound exhibits an optical band-gap of 1.4-1.5 eV and a high absorption coefficient.

Many other applications for ZnS had been reported. For instance, nanostructures of ZnS doped with Ni_2^+ could be used as a photocatalyst toward H_2 evolution.[30] Brayek et al. showed that ZnS coated ZnO nanorods could exhibit a photocurrent enhancement effect by effectively lowering the carrier recombination rate, thus improving the efficiency of the materials for water oxidation.[31] Several studies also reported the high field enhancement effect of ZnS nanowires that made them attractive for FET applications.[32–34] ZnS and Au-ZnS nanostructures could also be used as highly sensitive biosensors in glucose oxidase system.[35] or got decorated with carbon nanotube to be made into DNA sensors.[36] Nanocrystals of ZnSe/ZnS:Mn/ZnS is an attractive phosphor material to be used in alternative current thin-film electroluminescent (AC-TFEL) devices.[37] Tang et al. showed a study of ZnS in conjunction with $AgInS_2$ as a suitable material for cell imaging application.[38] ZnS could also be used as UV-light sensors[39,40] and in many other applications.[26,41,42]

2.3 Experimental

CVs and PP-ALD deposits were made with an electrochemical flow cell whose design has been optimized over many years. The set up consists of multiple solution bottles containing the elemental precursors and connecting to a valve block that determines which solution flows into the deposition cell. The potentiostat is hooked up to a computer to automate sequences for making deposits. More details of the hardware were described in many of the past references and could be obtained from the company Electrochemical ALD L.C. (Athens, GA).[4,5] The reference electrode used in all experiments was Ag/AgCl (3 M NaCl) purchased from Bioanalytical Systems Inc. (West Lafayette, IN). Gold substrates were made commercially by the company Evaporated Metal Films (Ithaca, NY). Each slide consisted of 100 nm-thick Au film on a 5 nm-thick Ti adhesion layer on glass. Before each experiment, gold slide was rinsed

throughoutly with acetone followed by ultra-pure water. Each slide was then submerged in concentrated nitric acid for 30 sec followed by a final rinse with ultra-pure water. 18 MΩ nanopure water standard (Millipore Advantage 10) was used to clean all the glassware, Au slides and to prepare the solutions. All solution bottles were cleaned with Nochromix for an hour followed by multiple rinse with 18 MΩ H_2O. To electrochemically clean the substrate, before each experiment, cyclic voltammetries of gold substrate were performed between -0.2 V and 1.4 V in 0.1 M H_2SO_4. In every CVs presented, the electrode surface was kept at 0.78 cm^2. Conversion between charge and monolayer was used to quantify the compound growth rate. A monolayer is defined as one adsorbate per Au substrate atom, which is about 1.2 x 10^{15} atoms per cm^2.

Precursor concentrations of ZnO and $Na_2S_2O_3$ were kept at 1 mM and the electrolyte used was 0.1 M $NaClO_4$. All solutions, valves and tubing were purged with nitrogen before and during experiments to exclude oxygen. Solution mixture was made by first sonicating ZnO in 70% $HClO_4$ for about 1 hour. The dissolved Zn^{2+} was then transferred to a solution containing acetate buffer. It is important that the solution got adjusted to pH $\sim$ 4 prior to the addition of thiosulfate in order to prevent formation of colloidal S. Final adjustment of pH to 4.8 was done with NaOH. Such protocol allowed the solution mixture to be stable for weeks as there was no colloidal S observed.

Electron probe Microanalysis (EPMA) analysis were done with a 10 KeV accelerating voltage, 15 nA beam current and 10 µm beam diameter. The instrument was a JEOL 8600 Superprobe. X-ray diffraction was performed on a PANalytical X'PERT Pro with an open Eulerian cradle utilizing a 1.54 Å Cu K_α source and a parallel plate collimator. Thickness measurement from spectroscopic ellipsometry was obtained with a J.A. Woolam M-200 V. The analysis was done using a B-Spline model for Au sub-

strate. The input refractive index for ZnS was 2.34. SEM images were taking with a Field Emission Scanning Electron Microscope, FEI Teneo, at 20 kV.

Photoelectrochemical measurements were used to determine the bandgap and the conductivity type. Light from a Xenon lamp would first go through a monochromator, being chopped and modulated by a lock-in-amplifier (SRS10830) before entering the cell where the substrate was positioned normal to the light source. The cell was set up with a three-electrode configuration. Voltage signal from the sample induced by the light was collected by the potentiostat before being modulated by the lock-in-amplifier. The liquid junction was created by using 0.1 M Na_2S/polysulfide solution at pH 11 as redox couple. The cell was kept in a dark box to avoid any ambient light interference.

2.4 Results and Discussion

2.4.1 Selection of a good pH range to work with both elements

The effect of pH on the electrodeposition was investigated to ensure the stability and reactivity of both precursors prior to and during the deposition process.[43] Figure 2.1a showed the UPD potential of Zn on Au with respect to pH. From pH 3.0 to 9.4, Zn deposition was independent of the acid concentration as the UPD potential remained at -0.6 V. Potential shifted negatively to -0.8 V at pH 13.0 with sharper peaks being observed at more basic pH. Oxidation and reduction of Zn UPD were highly reversible on Au. Regarding its chemical stability, Zn solution at pH 13.0 precipitates into $Zn(OH)_2$ after 2-3 days. On the other hand, highly acidic solution ($pH < 3$) makes Zn difficult to be deposited due to hydrogen evolution. Compare to other group II elements, Zn has a relatively low E^0.[44] The choice of pH for Zn can fall within the range of 3.0 – 9.4. The surface coverage resulted from a Zn UPD on Au was about 0.19 ML assuming a ML was $192\,\mu C/e^-/cm^2$.

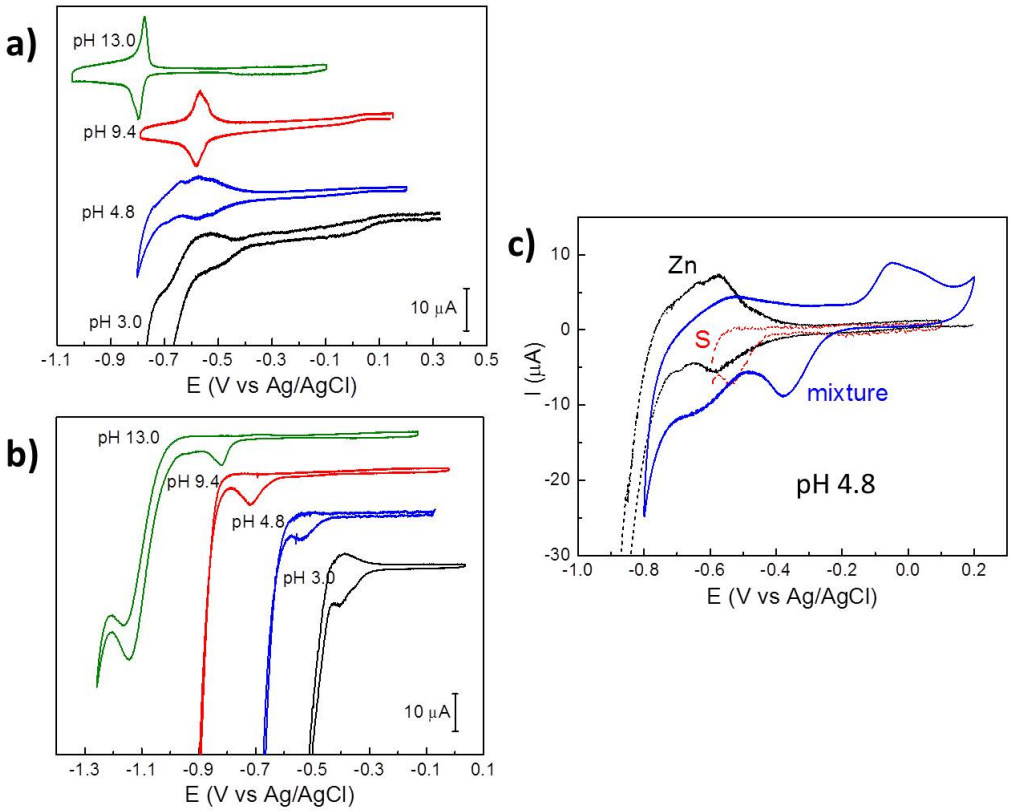

Figure 2.1: pH study of individual precursors and their mixture (a) CVs of Zn^{2+} at different pH. Solutions contain 1 mM ZnO and 0.1 M NaClO4 as electrolyte. Acetate buffer is used for pH 4.8 and ammonia buffer is used for pH 9.4. The UPD potential of Zn remains the same from pH 3.0 to 9.4. (b) Dependence of $S_2O_3{}^{2-}$ CVs on pH. Solutions contain 1 mM $Na_2S_2O_3$ and 0.1 M $NaClO_4$. At OCP, thiosulfate spontaneously disproportionates to form a layer of S on Au. Reductive stripping of S layer shifts negatively with more basic pH. Suspension of colloidal S occurred at pH < 3. At pH 9.4, ZnS deposit does not seem to form. (c) CVs of Zn^{2+}, $S_2O_3{}^{2-}$, and their mixture at pH 4.8. ZnS formation is more favorable and thermodynamically stable than their individual component on Au substrate.

The chemistry of thiosulfate is more complex and not well-understood. Formation of S from thiosulfate is through a disproportionation process proposed by the following equation:

$$S_2O_3{}^{2-} + 2\ H^+ \rightarrow S + SO_3 + H_2O$$

Unlike in S^{-2} solution where an oxidative UPD of S was electrochemically observed, there was no apparent oxidative peak of S UPD in thiosulfate solution. Instead, the formation of S can be monitored indirectly by first letting the thiosulfate disproportionate and then examining the reductive stripping of S to S^{2-} species. Figure 2.1b showed that the reduction of S monolayer to S^{2-} from Au shifted negatively as the solution became more basic. The open circuit potential (OCP) of thiosulfate was more positive than the S reduction, suggesting that the precursor can disproportionate spontaneously on Au to produce an initial layer of S.[45] There is an additional peak at -1.1 V in pH 13.0 that could be a decomposition of thiosulfate into sulfide ($S_2O_3{}^{2-}$ to S^{2-}). Such peak not being observed at less basic pH might be due to early occurrence of hydrogen evolution. The stability and reactivity of thiosulfate solution varied significantly by pH. At highly acidic pH (< 3), thiosulfate decomposed into colloidal S and could be used to codeposit ZnS at an overpotential (typically more than 1 V) where bulk Zn would form.[28] This approach, however, is more prone to inconsistent in the deposit composition.[10] Adjusting to more basic solution would reduce S precipitation; however, at pH 9.4, the thiosulfate disproportionation rate seems to be insufficient to form ZnS compound. The chemistry of thiosulfate is the limiting factor to the selection of pH. The optimal condition is at pH 4.8 where both elements can be put together to make deposit using PP-ALD. S UPD on Au was about 0.10 ML of surface coverage.

Figure 2.11c summed up the CVs of individual elements and the mixture at pH 4.8. It is notable that Zn^{2+} reduction on a layer of S occurred at 0.2 V less negative than Zn UPD of Au. This suggested that the formation of ZnS was favorable and

could form more readily than Zn on Au. The oxidative stripping of Zn from S was also not as reversible as Zn from Au, indicating that the compound became more stable once it formed. A similar observation was made from previous study on the E-ALD of ZnS using S^{2-} as sulfur source.[46]

2.4.2 Window opening cyclic voltammetry of individual elements and the mixture

Figure 2.2a and b show full CVs of Zn and thiosulfate at pH 4.8. In Figure 2.2a, the negative window opening of Zn solution shows a completion of UPD process at -0.8 V, and a bulk deposition at -1.2 V. The negative background suggests strong interference from hydrogen evolution. Figure 2.2b shows the positive window opening of thiosulfate. The OCP was around -0.1 V. The reduction peak at -0.55 V corresponds to the previously mentioned S single layer stripping from Au substrate. As the electrode was scanned positively to 0.3 V, an oxidation was observed, indicating the formation of soluble polysulfide $S_8{}^{2-}$ species.[45] This process was intermixed with the insoluble bulk S deposition at further positive potential. The reduction of bulk S from the surface formed a new peak at -0.4 V, which only appeared when the electrode was oxidized previously. The anodic process required more charge than its cathodic counterpart, due to the formation of polysulfide that escaped the electrode.

Figures 2.3a and b show both positive and negative window openings of the mixture. The OCP was around 0 mV. In Figure 2.3a, -0.8 V was selected to be the negative end of the working window. As the positive end expands after every cycle, the reduction peak corresponding to bulk S stripping shifted from -0.4 V on Au to -0.7 V when the substrate became ZnS. This complements with the earlier observation that the once the compound forms, it gets harder to strip the S off reductively from the compound. Similar conclusion can be made from the negative window openings

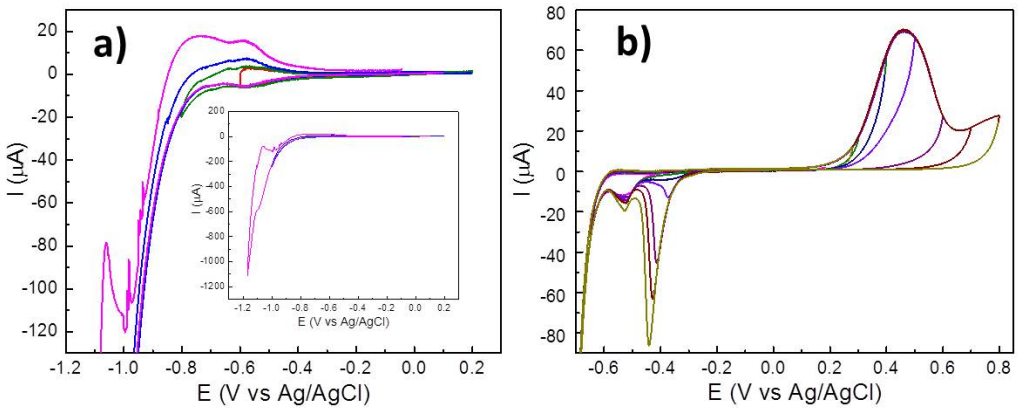

Figure 2.2: Complete CVs of individual elements at pH 4.8 (a) Negative window opening of Zn (b) Positive window opening of thiosulfate.

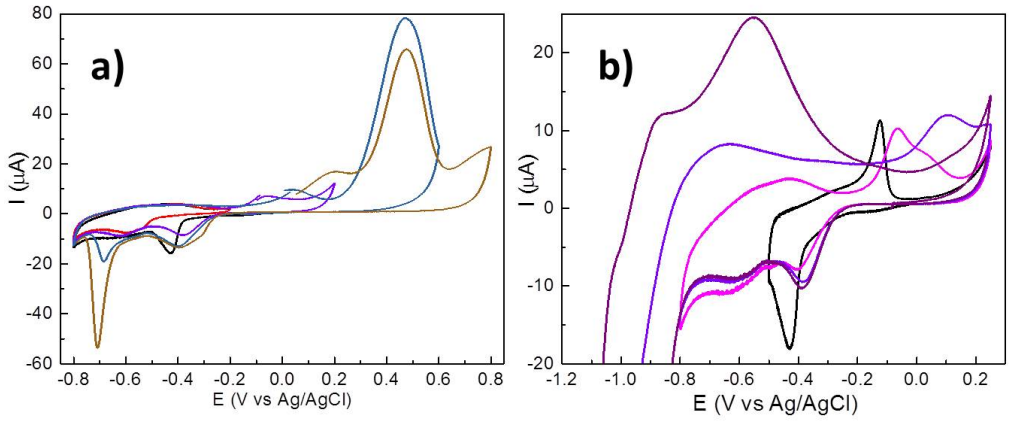

Figure 2.3: Window opening experiments in a Zn thiosulfate mixture at pH 4.8. (a) Positive window opening showing that it is harder to strip bulk S off. (b) Negative window opening showing that Zn removal from the compound is also more difficult.

of the mixture. As the compound grows after every cycle, the oxidation of Zn shifts positively as it becomes more stable.

2.4.3 Selection of UPD potentials to deposit each element

An optimal deposition potential is one that only puts down a submonolayer amount of material from each pulse. In order to select the cathodic potential, deposits were made with a constant anodic bias while varying the reductive potential. The growth rate and elemental ratio of each deposit were determined with EPMA. The film thickness obtained from ellipsometry and the atomic percentage of each element from EPMA both supported the same trend.

Figure 2.4a showed the effect of changing the cathodic potential on the growth rate and the elemental ratio of different deposits. Each film was made from 1400 cycles alternating between a cathodic and an anodic pulse. The anodic potential was held at 0.3 V for 0.5 s while the cathodic potential was varied in the duration of 0.5 s. According to the CV of thiosulfate on Au (Figure 2.2b), 0.3 V is where oxidative UPD of S has been completed and it is right at the onset of thiosulfate oxidation into polysulfide. The UPD region for Zn deposition was identified to be around -0.75 and -0.8 V, in which the thickness of the deposits did not change much. Potential more positive than UPD resulted in incomplete formation of Zn monolayer, leading to little to no deposit (-0.725 V and -0.70 V). On the other hand, potential more negative than UPD could induce some Zn bulk deposition and thus caused the growth rate to increase (-0.85 V and -0.90 V). The use of more negative potential also created a roughening effect in surface morphology. Deposit formed at -0.90 V displayed a whitish powdery appearance unlike the reflective surfaces of the rest of the samples. Such coarsening effect could be due to the physical evolution of hydrogen occurred at the surface that hindered a conformal coating of the compound. Any defect site could

potentially give rise to more hydrogen bubble formation and further exacerbated the roughening process.

Figure 2.4b describes the dependence of growth rate and elemental ratio on the anodic potential. The cathodic potential was selected from Figure 4a to be at -0.8 V. Pulse duration was kept at 0.5 s. No deposit formed at the anodic potential of 0 V, suggesting that a more positive bias was necessary for the formation of new S layer. The codeposition of ZnS at -0.8 V would stop at 1.5 ML unless an anodic potential was applied to form new layer S (See Supporting Information 2.5). The UPD range to deposit S is between 0.2 V and 0.3 V. Potential above 0.3 V is where polysulfide and bulk S start to deposit (Figure 2.2b), thus is not ideal for surface-limited reaction. Note that for all deposits, the Zn:S ratio remained around 1.0 - 1.2 regardless of the potential used. This suggested that the deposition of one element was influencing the other. Once Zn formed on the surface at the cathodic potential, the anodic potential allowed thiosulfate to disproportionate accordingly to form stoichiometric compound.

2.4.4 Pulse duration study: Effects on growth rate and Zn:S

The study of pulse duration provides insight into the time frame of the deposition process. A pulse should not be too short to avoid incomplete reaction, but also not too long to be efficient. The effect of the cathodic duration on the growth rate and the Zn:S ratio was studied in Figure 2.6a. Each deposit was made from 1000 pulses. Anodic potential was at 0.3 V for 0.5 s and cathodic potential was at -0.8 V for various durations. Changes in the cathodic duration did not result in an increase in thickness, as expected for a surface-limited process. This result showed that deposits could be made faster by decreasing the pulse duration. However, at 0.3 s, the surface started to become roughening from the remaining inequilibrium. The smoothest deposit was made at 2 s pulse duration in which the surface appeared very reflective.

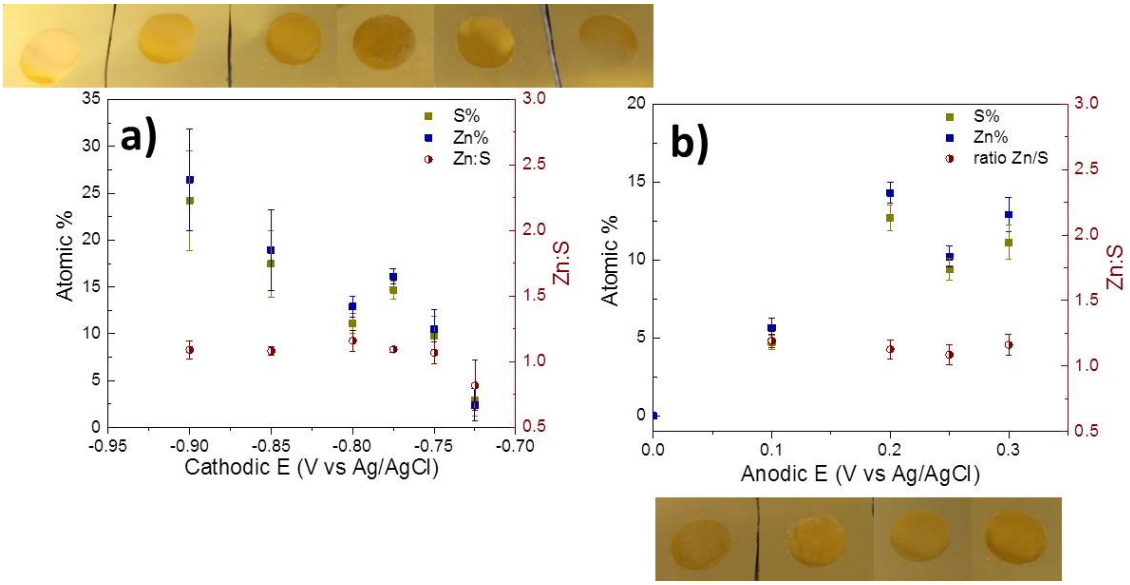

Figure 2.4: Optimizing the UPD potentials to deposit submonolayer amount of material from each pulse. Each deposit was made from 1400 cycles alternating between cathodic and anodic pulses. Each pulse's duration was kept at 0.5 s. (a) Dependence of growth rate and elemental ratio on the cathodic potential. Anodic potential was held at 0.3 V. UPD of Zn ranges from -0.75 to -0.8 V. (b) Effect of anodic potential on growth rate and elemental ratio. Cathodic potential was held at -0.8 V. UPD of S ranges from 0.2 to 0.3 V.

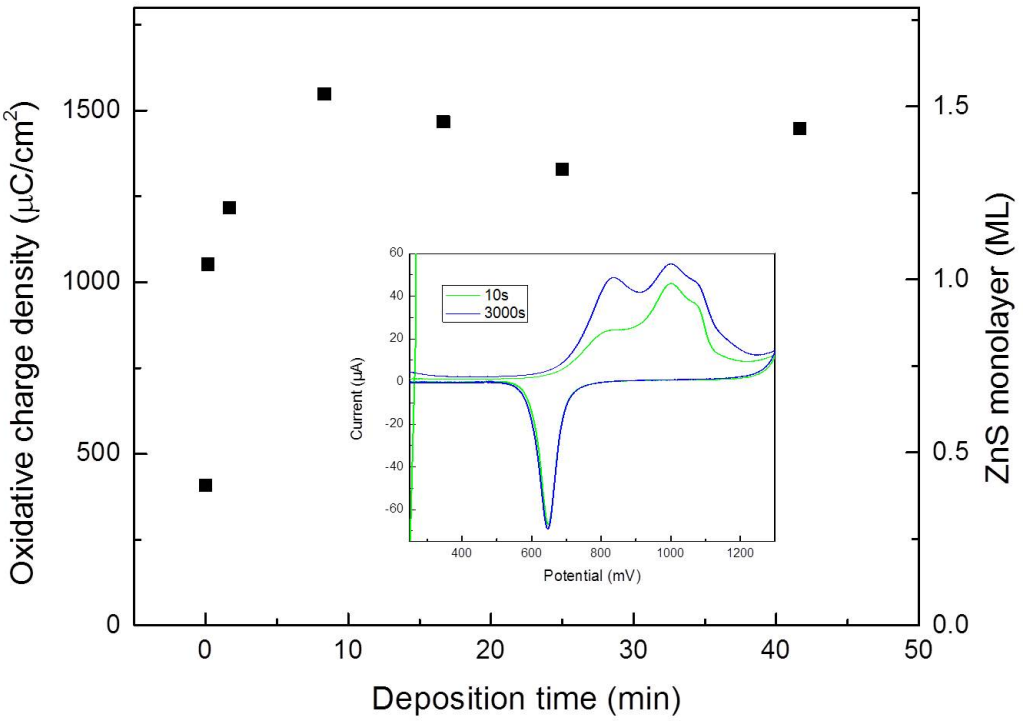

Figure 2.5: Oxidative stripping charge density from the codeposition of ZnS at -0.8 V at varying times. The maximum coverage was 1.5 ML assuming an 8 e^- process. No further growth was observed after 10 minutes of holding.

Extending the anodic duration at 0.3 V resulted in a slight increase in thickness (Figure 2.6b). This could be due to the potential selected being too close to the onset of the polysulfide formation. When the anodic potential got changed to -0.25 V, the samples' thicknesses became independent of the total pulse duration, indicating that surface-limited reactions were successfully achieved for both elements (Figure 2.6c).

2.4.5 Pulsed Potential - Atomic Layer Deposition

Ability to control thickness

A schematic of the PP-ALD of ZnS was demonstrated in Figure 2.7a. The first UPD layer S was spontaneously deposited at OCP. This was followed by an applied cathodic potential to deposit only a UPD amount of Zn. The next anodic pulse would strip off any excess Zn that had not bind to previous S layer while forming a new layer of S on the surface. This positive bias was necessary for the continual growth of the compound. Repetition of these steps resulted in a conformal layer of ZnS formed only through surface-limited reaction. Figure 2.7b showed an example of a simple pulse profile consisted of one cathodic pulse and one anodic pulse per cycle. The graph of current potential as a function of time gave forth to a preliminary estimation of how much charge was put down each cycle.

To quantify the growth rate, oxidative charge from ZnS stripping was quantified as a function of the number of pulse cycle (Figure 2.8a). The charge was converted into the number ZnS monolayer in which 126 µC corresponded to a ML of ZnS per e^- and it was assumed to be an 8 e^- process. The linear regression showed a growth rate of 0.03 ML per pulse. In addition, spectroscopic ellipsometry was used to determine the thickness of thicker samples (Figure 2.8b). Similarly, a linear correlation between the samples' thicknesses and the number of pulses was also observed. The growth rate was around 0.013 nm per pulse. The d-spacing of ZnS, according to the literature,

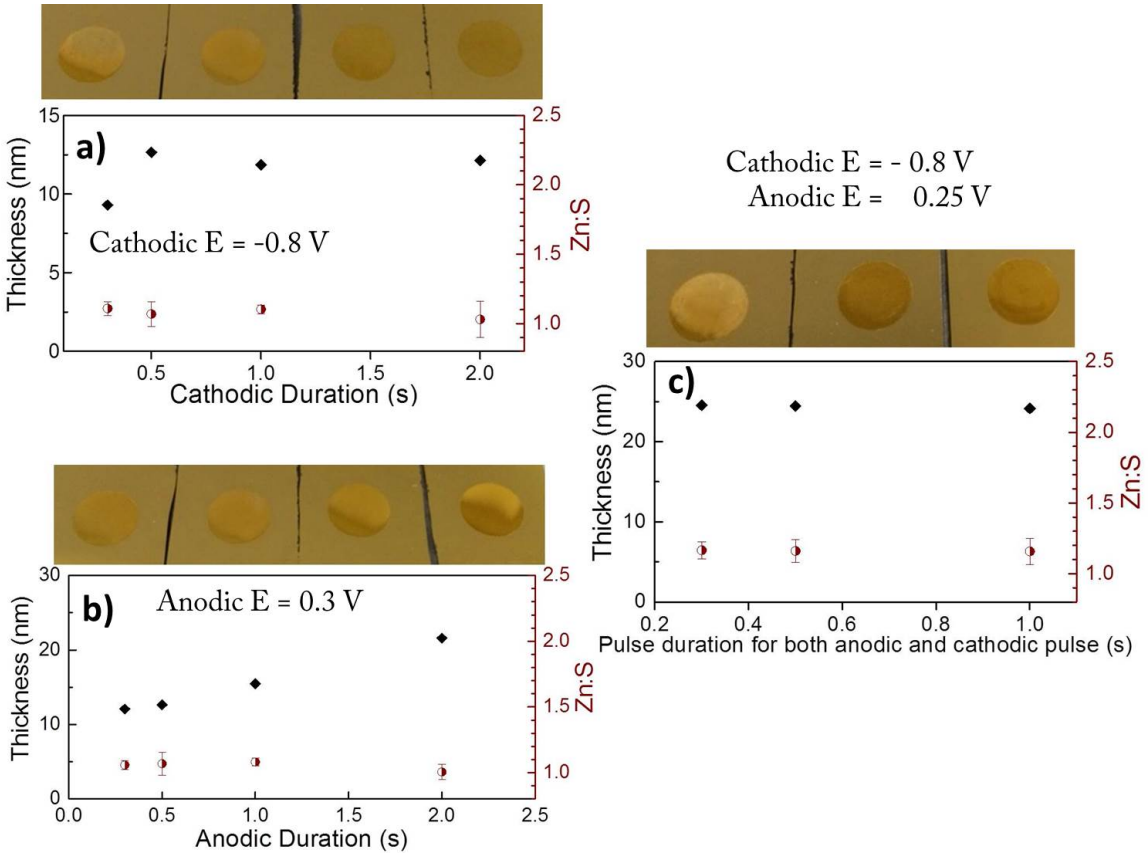

Figure 2.6: Pulse duration studies. Each deposit was made of 1000 pulses. In (a) and (b), anodic E = 0.3 V and cathodic E = -0.8 V. In (c), anodic E = 0.3 V. Atomic percentages obtained from EPMA and the thickness from ellipsometry supported the same trends. (a) Dependence of cathodic duration on growth rate and elemental ratio. Anodic duration = 0.5 s at. (b) Effect of changing the anodic duration at -0.3 V. Cathodic duration = 0.5 s.

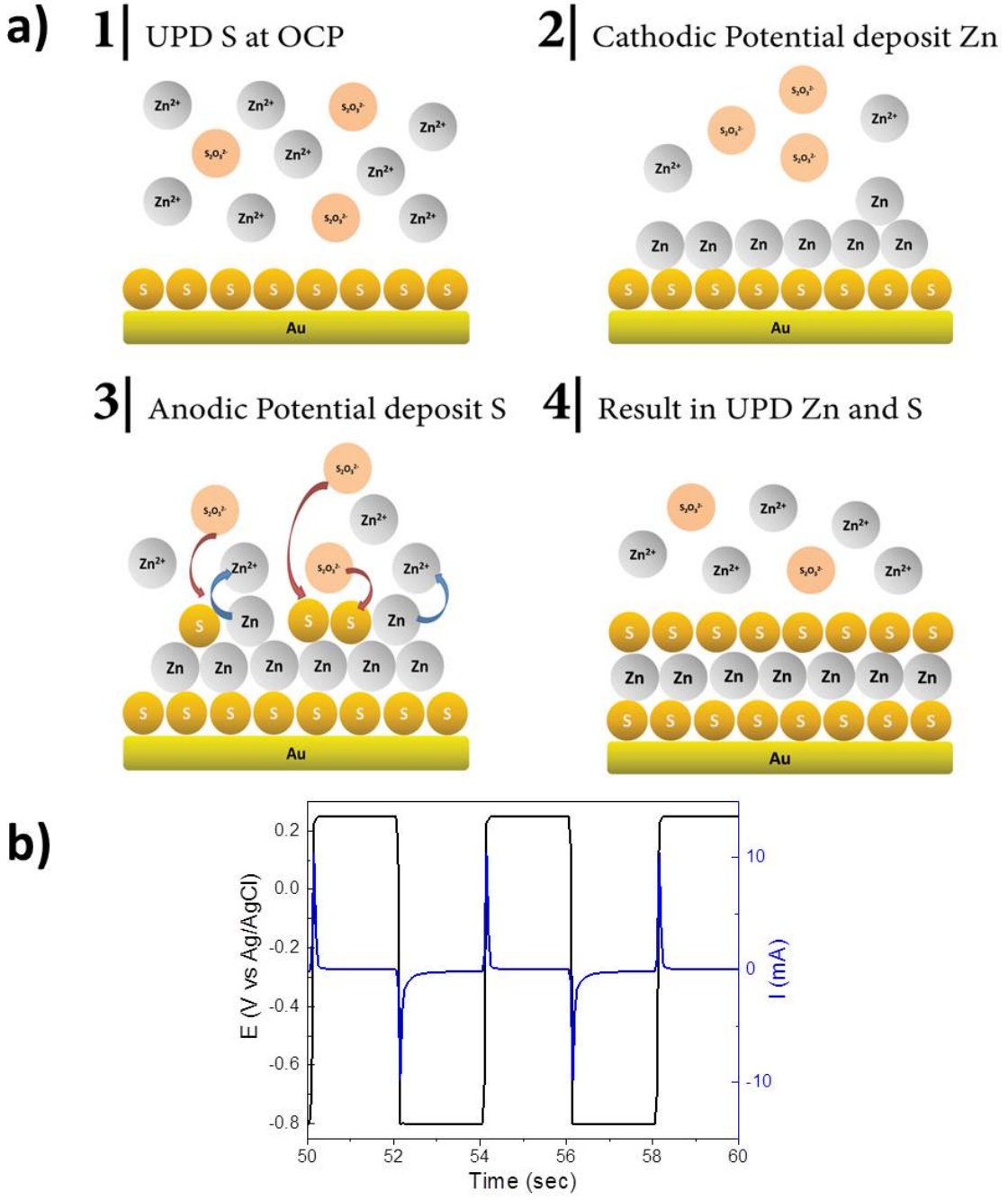

Figure 2.7: (a) Schematic representation of the PP-ALD of ZnS. (b) Example of several deposition cycles. Cathodic E = -0.8 V for 2 s and anodic E = 0.25 V for 2s. Cycles were repeated multiple times to obtain the sample thickness desired.

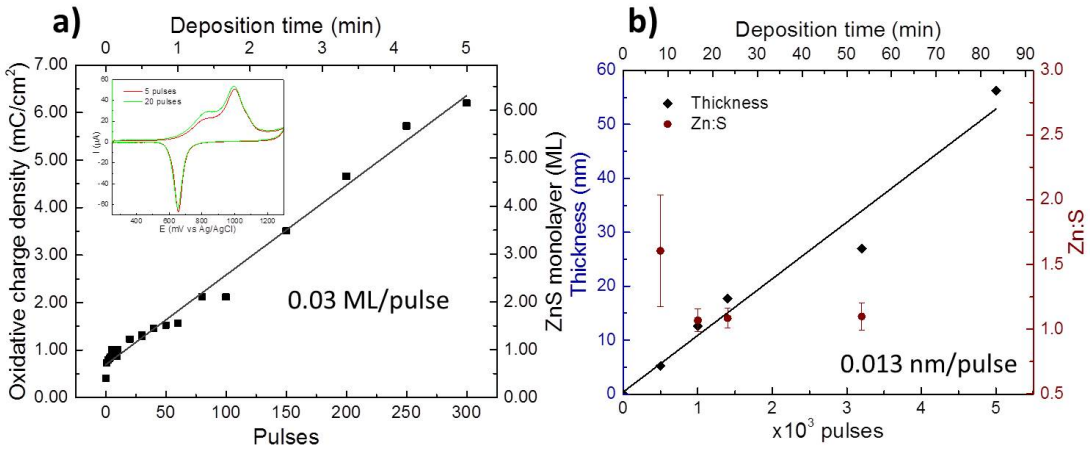

Figure 2.8: Control of thickness by PP-ALD. (a) Oxidative charge density stripping of ZnS showing the dependence of growth rate on the number of cycles. E cathodic = -0.8 V for 0.5 s. E anodic = 0.25 V for 0.5 s. (b) Spectroscopic ellipsometry data showing ZnS deposits' thicknesses as a function of pulse number.

was 0.1344 nm. The dependence of growth rate on the number of pulses indicated the compound's thickness could be controlled by PP-ALD.

Intermediate pulse study

SEM was used to study the surface morphology of the ZnS deposits. Figure 2.9a shows an example of a sample made from 5000 cycles consisting of a 2 s cathodic pulse of -0.8 V and another 2 s anodic pulse of 0.25 V. Many clusters with varying sizes (10 – 100 nm) were observed. Heating the substrate to 200 °C did not improve the surface morphology, as can be seen in Figure 2.9b. However, an addition of some rest potentials between the cathodic and anodic pulses could significantly reduce the number of clusters from the surface (Figure 2.9c and d). Figure 2.9c shows the surface of a sample made from an intermediate pulse profile consisting of a 2 s cathodic pulse of -0.8 V, follows by a 1 s rest potential at -0.7 V, and another 2 s anodic pulse of 0.25 V, follows by a 1 s rest potential at 0 V. Figure 2.9d uses a similar pulse profile to one in 2.9c, but with all the pulse duration shortened in half. Some clusters reappeared, but their density and sizes were lower than those in 2.9a or 2.9b. The effect of the rest potential could be seen as equivalent to rinsing the surface with the blank solution between cycles in an E-ALD process. With PP-ALD, simply pulse the potentials between the oxidation and reduction processes without any rinsing step could cause some reactive species in proximity to the surface to precipitate and land on the surface, forming random clusters.

Characterization with Photoelectrochemistry and XRD

The bandgap of all ZnS deposits grown by the present method were measured to be around 3.50 eV, as expected from the literature (Figure 2.10a). The conductivity type was determined from two methods: the Mott-Schottky plot and photochemistry. Photocurrent was detected only at the positive bias, indicating that holes are the

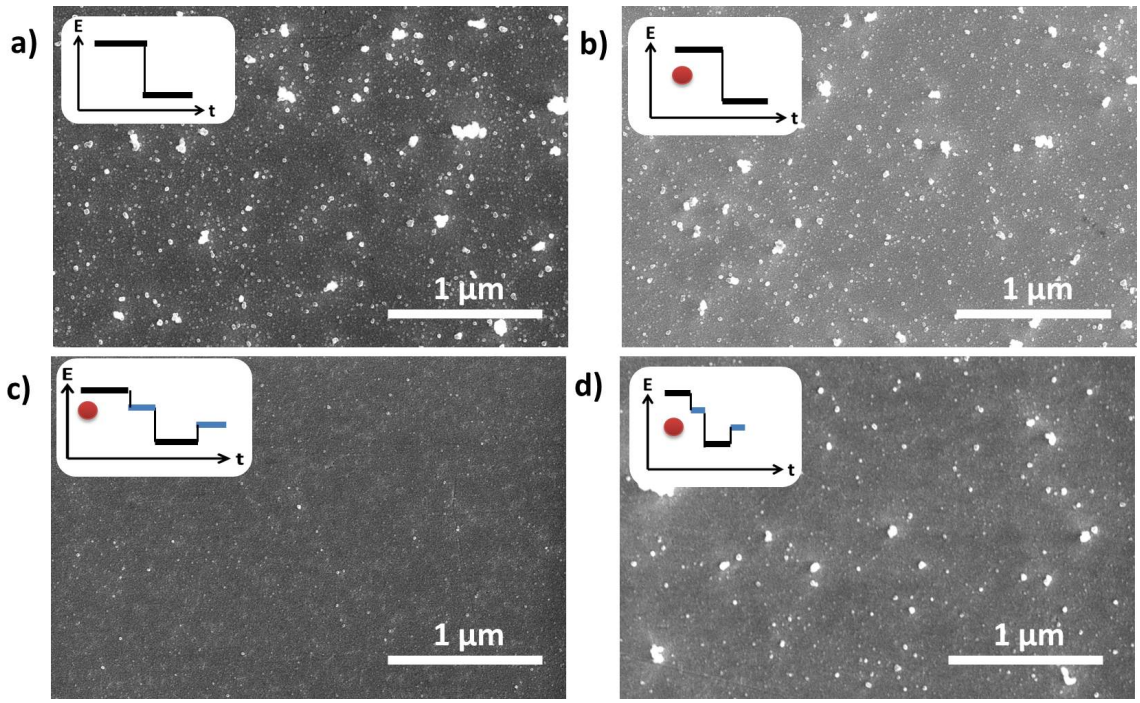

Figure 2.9: Rest potentials were used to improve the surface morphology of ZnS deposits. SEM images from samples made from 5000 cycles consisting of (a) 2 s cathodic pulse of -0.8 V and 2 s anodic pulse of -0.25 V, (b) is (a) after heating to 200 °C, (c) 2 s cathodic pulse of -0.8 V, 1 s rest potential at -0.7 V, 2 s anodic pulse of -0.25 V, and 1 s rest potential at 0 mV, heated to 200 °C (d) 1 s cathodic pulse of -0.8 V, 0.5 s rest potential at -0.7 V, 1 s anodic pulse of -0.25 V, and 0.5 s rest potential at 0 mV, heated to 200 °C.

minority carriers (Figure 2.10b). The positive slope in the Mott-Schottky plot also suggested that the ZnS films are n-type semiconductor (Supplemental Information 2.12).

The XRD pattern showed a broad peak of ZnS at 2θ around 28.2, indicating the formation of small nanocrystals (Figure 2.11). The thicknesses of these films were around 20 nm from ellipsometry. The broad peak could be the result of averaging several different ZnS structures. For instance, both sphalerite(111) and wurtzite(002) could display patterns at around 28 2θ. Similar to the result from SEM in Figure 2.9b, annealing the samples did not seem to change the quality of the deposit. There was no substantial difference between different annealing temperatures in terms of morphology, atomic % and the elemental ratio.

Mechanism of S formation was still not clear

Attempt had been made to codeposit Zn and S in the potential range of Zn UPD. Without the formation of a new layer of S, the deposit was terminated with a Zn surface and cannot grow more than 1.5 ML. Figure 2.5 from Supplemental information illustrated a series of experiments investigating into the codeposition of ZnS at -0.8 V. The intention was to have only a UPD amount of Zn grows on a monolayer of S formed spontaneously when the solution is in contact with the Au substrate. Oxidative charge density was quantified by integrating the peak corresponded to ZnS oxidation with correction that took into account Au oxidation. According to Figure 2.5, the compound did not continue to grow once the surface was covered with 1.5 ML of ZnS. This result led to the conclusion that the anodic pulse to form new S layer was necessary for the continuing growth of ZnS compound.

A similar approach to codeposit ZnS was proposed by Demir et al.[47] Instead of thiosulfate, Na2S in combination with $EDTA^{2-}$ were used as an alternative S precursor. Concentration of Zn^{2+} and $EDTA^{2-}$ was finely tuned so that the deposition

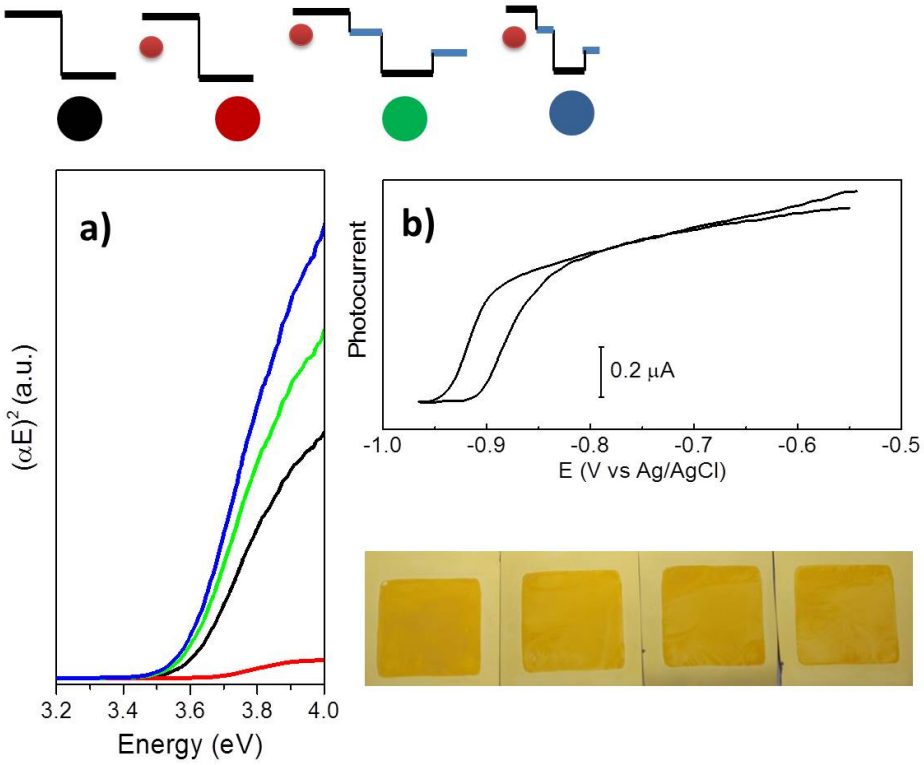

Figure 2.10: Bandgap and conductivity measurements from photoeletrochemistry. (a) Bandgap from the same samples described in Figure 2.9. (b) Representative plot of a conductivity-type measurement.

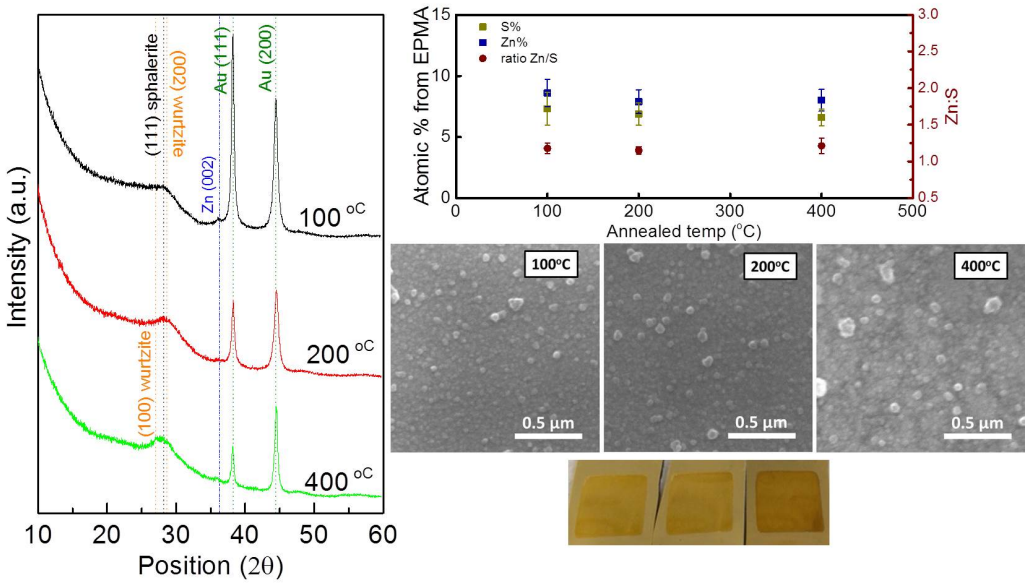

Figure 2.11: Annealing study at different temperatures. Results were obtained from XRD, EPMA and SEM. XRD suggests the formation of nanocrystal size of ZnS. At 400 °C, the surface seemed to crack, causing a slight discoloration. Negligible difference in the atomic % and the elemental ratio was observed at different annealing temperatures.

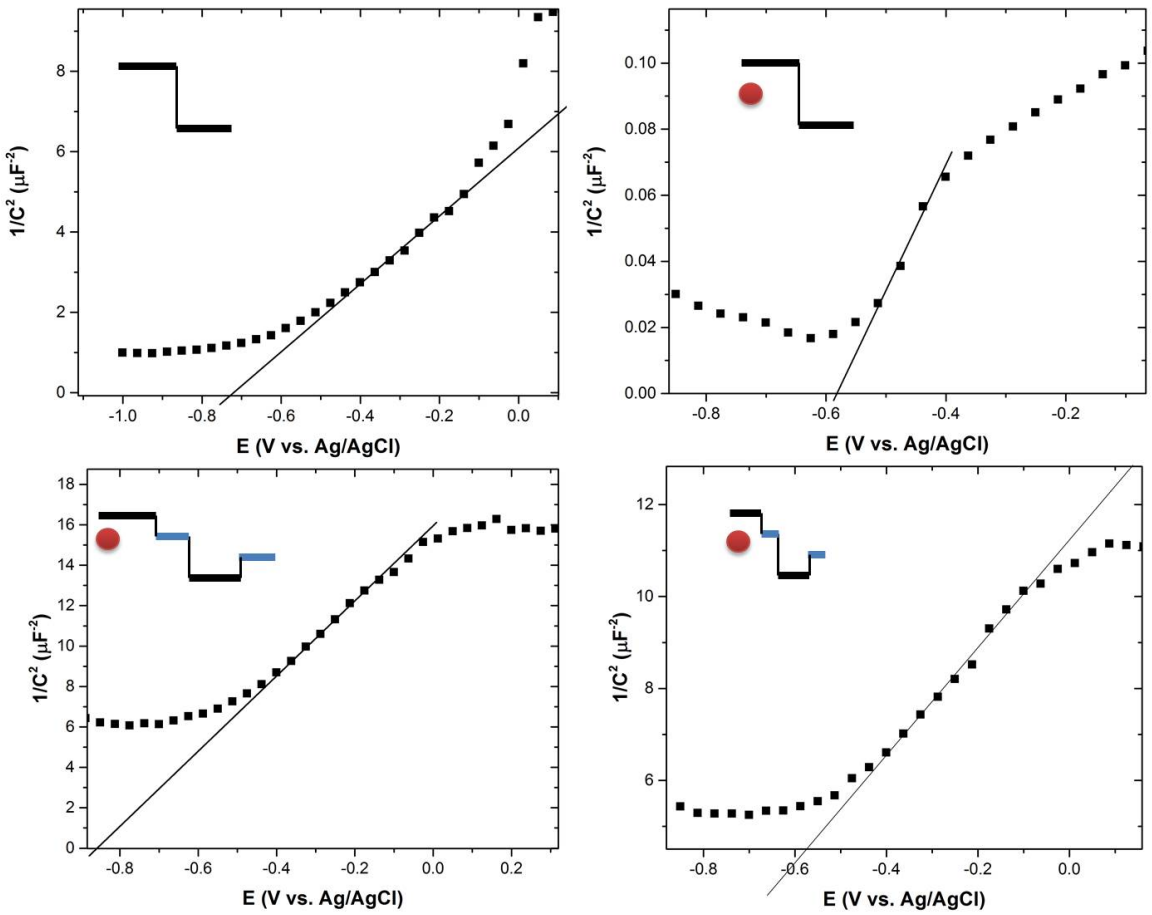

Figure 2.12: Mott-Schottky curves of ZnS films. Electrolyte was 0.5 M K_2SO_4 at pH 6.

potential of Zn and S would occur at potential, allowing them to codeposit at an atomically controlled level. This style of codeposition resulted in very high-quality ultrathin film, albeit limited by the growth speed for thicker material application.

2.5 Conclusion

The electrodeposition of ZnS is typically done by codepositing both precursors from solution contained acidic thiosulfate as a source of colloidal S. The decomposition product of thiosulfate such as S^{2-} or colloidal S can react with the bulk Zn deposited. This approach, however, has very limited ability to control the growth of the compound, and the surface of these deposits also tends to be rough due to disruption from hydrogen evolution. Avoiding such negative potential would allow the deposit to grow at a more controllable rate, preserving the integrity of the surface.

The concept of PP-ALD was demonstrated by growing ZnS nanofilms. Similar to E-ALD, PP-ALD provides the ability to control the deposition rate and obtain the desired film thickness. By tuning into the UPD potentials of individual element, only a surface-limited amount would be deposited at a time. Cyclic voltammetry was used to study the electrochemical behaviors of Zn^{2+} and thiosulfate precursors. The pH selection was made based on the limited stability and reactivity of thiosulfate. Characterization of thicker deposits was done with EPMA, ellipsometry, SEM, photochemistry and XRD. Thickness of the films can be finely controlled by changing the number of cycles repeated. Addition of some rest potentials between cycles could improve the surface morphology. The ZnS films exhibit a band gap around 3.50 eV and n-type conductivity. XRD patterns showed a broad ZnS peak, suggesting the formation of small nanocrystals.

2.6 Acknowledgments

Support from the National Science Foundation, DMR # 1410109, is gratefully acknowledged.

References

(1) Stickney, J. L.; Villegas, I.; Suggs, D. W.; Gregory, B. W. Electrochemical Atomic Layer Epitaxy (ECALE). *Abstracts of Papers of the American Chemical Society* **1991**, *201*, 289–Coll.

(2) Stickney, J. L. Ii-Vi Compound Semiconductor Thin-Film Electrodeposition by Ecale. *Abstracts of Papers of the American Chemical Society* **1995**, *210*, 297–Inor.

(3) Gregory, B. W.; Stickney, J. L. Electrochemical Atomic Layer Epitaxy (ECALE). *Journal of Electroanalytical Chemistry* **1991**, *300*, 543–561.

(4) Czerniawski, J. M.; Perdue, B. R.; Stickney, J. L. Potential Pulse Atomic Layer Deposition of Cu_2Se. *Chemistry of Materials* **2016**, *28*, 583–591.

(5) Czerniawski, J. M.; Stickney, J. L. Electrodeposition of In_2Se_3 Using Potential Pulse Atomic Layer Deposition. *Chemistry of Materials* **2016**.

(6) Kressin, A. M.; Doan, V. V.; Klein, J. D.; Sailor, M. J. Synthesis of Stoichiometric Cadmium Selenide Films Via Sequential Monolayer Electrodeposition. *Chemistry of Materials* **1991**, *3*, 1015–1020.

(7) Caballero-Briones, F.; Palacios-Padros, A.; Sanz, F. CuInSe2 films prepared by three step pulsed electrodeposition. Deposition mechanisms, optical and photoelectrochemical studies. *Electrochimica Acta* **2011**, *56*, 9556–9567.

(8) Chaudhari, S.; Palli, S.; Kannan, P. K.; Dey, S. R. Pulsed electrodeposition of Cu_2ZnSnS_4 absorber layer precursor for photovoltaic application. *Thin Solid Films* **2016**, *600*, 169–174.

(9) Endo, S.; Nagahori, Y.; Nomura, S. Preparation of $CuInSe_2$ thin films by the pulse-plated electrodeposition. *Japanese Journal of Applied Physics Part 2-Letters* **1996**, *35*, L1101–L1103.

(10) Fathy, N.; Ichimura, M. Photoelectrical properties of ZnS thin films deposited from aqueous solution using pulsed electrochemical deposition. *Solar Energy Materials and Solar Cells* **2005**, *87*.

(11) Guo, M.; Zhu, X. R.; Li, H. J. Comparative study of Cu_2ZnSnS_4 thin film solar cells fabricated by direct current and pulse reverse co-electrodeposition. *Journal of Alloys and Compounds* **2016**, *657*, 336–340.

(12) Gurav, K. V.; Kim, Y. K.; Shin, S. W.; Suryawanshi, M. P.; Tarwal, N. L.; Ghorpade, U. V.; Pawar, S. M.; Vanalakar, S. A.; Kim, I. Y.; Yun, J. H.; Patil, P. S.; Kim, J. H. Pulsed electrodeposition of Cu_2ZnSnS_4 thin films: Effect of pulse potentials. *Applied Surface Science* **2015**, *334*, 192–196.

(13) Hennayaka, H. M. M. N.; Lee, H. S. Structural and optical properties of ZnS thin film grown by pulsed electrodeposition. *Thin Solid Films* **2013**, *548*, 86–90.

(14) Hu, S. Y.; Lee, W. H.; Chang, S. C.; Cheng, Y. L.; Wang, Y. L. Pulsed Electrodeposition of $CuInSe_2$ Thin Films onto Mo-Glass Substrates. *Journal of the Electrochemical Society* **2011**, *158*, B557–B561.

(15) Kim, M. J.; Lim, T.; Park, K. J.; Kim, S. K.; Kim, J. J. Pulse-Reverse Electrodeposition of Cu for the Fabrication of Metal Interconnection II. Enhancement of Cu Superfilling and Leveling. *Journal of the Electrochemical Society* **2013**, *160*, D3088–D3092.

(16) Klochko, N. P.; Myagchenko, Y. O.; Melnychuk, E. E.; Kopach, V. R.; Klepikova, E. S.; Lyubov, V. N.; Khrypunov, G. S.; Kopach, A. V. Prospects for the pulsed electrodeposition of zinc-oxide hierarchical nanostructures. *Semiconductors* **2013**, *47*, 1123–1129.

(17) Mandati, S.; Sarada, B. V.; Dey, S. R.; Joshi, S. V. Pulsed Electrodeposition of $CuInSe_2$ Thin Films with Morphology for Solar Cell Applications. *Journal of the Electrochemical Society* **2013**, *160*, D173–D177.

(18) Mandati, S.; Sarada, B. V.; Dey, S. R.; Joshi, S. V. Photoelectrochemistry of $Cu(In_Ga)Se-2$ thin-films fabricated by sequential pulsed electrodeposition. *Journal of Power Sources* **2015**, *273*, 149–157.

(19) Murali, K. R.; Vasantha, S.; Rajamma, K. Properties of pulse plated ZnS films. *Materials Letters* **2008**, *62*, 1823–1826.

(20) Murali, K. R.; Balasubramanian, M. Influence of pulse reversal on the performance of pulse electrodeposited copper indium sulphide solar cells. *Journal of Materials Science-Materials in Electronics* **2013**, *24*, 3575–3580.

(21) Nomura, S.; Nishiyama, K.; Tanaka, K.; Sakakibara, M.; Ohtsubo, M.; Furutani, N.; Endo, S. Preparation of CuInSe2 thin films on Mo-coated glass substrates by pulse-plated electrodeposition. *Japanese Journal of Applied Physics* **1998**, *37*, 3232–3237.

(22) Pagnanelli, F.; Altimari, P.; Bellagamba, M.; Granata, G.; Moscardini, E.; Schiavi, P. G.; Toro, L. Pulsed electrodeposition of cobalt nanoparticles on copper: influence of the operating parameters on size distribution and morphology. *Electrochimica Acta* **2015**, *155*, 228–235.

(23) Valdes, M. H.; Vazquez, M. Pulsed electrodeposition of p-type $CuInSe_2$ thin films. *Electrochimica Acta* **2011**, *56*, 6866–6873.

(24) Xue, Z.; Li, X. L.; Yu, D. M. Bi_2Se_3/Bi multiple heterostructure nanowire arrays formed by pulsed electrodeposition. *Superlattices and Microstructures* **2014**, *74*, 273–278.

(25) Zanettini, S.; Bissoli, F.; Nasi, L.; Ranzieri, P.; Gilioli, E. Low temperature pulsed electron deposition and characterization of ZnS films for application in solar cells. *Crystal Research and Technology* **2011**, *46*, 881–884.

(26) Fang, X. S.; Zhai, T. Y.; Gautam, U. K.; Li, L.; Wu, L. M.; Yoshio, B.; Golberg, D. ZnS nanostructures: From synthesis to applications. *Progress in Materials Science* **2011**, *56*, 175–287.

(27) Tang, H. P.; Kwon, B. J.; Kim, J.; Park, J. Y. Growth Modes of ZnS Nanostructures on the Different Substrates. *Journal of Physical Chemistry C* **2010**, *114*, 21366–21370.

(28) Chassaing, E.; Naghavi, N.; Bouttemy, M.; Bockelee, V.; Vigneron, J.; Etcheberry, A.; Lincot, D. Electrodeposition Mechanism of Indium Sulfide and Indium Oxi(hydroxi)sulfide Thin Films from In(III)-thiosulfate Acidic Aqueous Solutions. *Journal of the Electrochemical Society* **2012**, *159*, D347–D354.

(29) Nakada, T.; Hongo, M.; Hayashi, E. Band offset of high efficiency CBD-ZnS/CIGS thin film solar cells. *Thin Solid Films* **2003**, *431*, 242–248.

(30) Bang, J. H.; Hehnich, R. J.; Suslick, K. S. Nanostructured ZnS: Ni_2^+ photocatalysts prepared by ultrasonic spray pyrolysis. *Advanced Materials* **2008**, *20*, 2599–2603.

(31) Brayek, A.; Chaguetmi, S.; Ghoul, M.; Ben Assaker, I.; Souissi, A.; Mouton, L.; Beaunier, P.; Nowak, S.; Mammeri, F.; Chtourou, R.; Ammar, S. Photoelectrochemical properties of nanocrystalline ZnS discrete versus continuous coating of ZnO nanorods prepared by electrodeposition. *Rsc Advances* **2016**, *6*, 30919–30927.

(32) Chen, S. M.; Li, L.; Wang, X.; Tian, W.; Wang, X. B.; Tang, D. M.; Bando, Y.; Golberg, D. Dense and vertically-aligned centimetre-long ZnS nanowire arrays:

ionic liquid assisted synthesis and their field emission properties. *Nanoscale* **2012**, *4*, 2658–2662.

(33) Fang, X. S.; Bando, Y.; Shen, G. Z.; Ye, C. H.; Gautam, U. K.; Costa, P. M. F. J.; Zhi, C. Y.; Tang, C. C.; Golberg, D. Ultrarine ZnS nanobelts as field emitters. *Advanced Materials* **2007**, *19*, 2593–+.

(34) Lu, F.; Cai, W. P.; Zhang, Y. G.; Li, Y.; Sun, F. Q.; Heo, S. H.; Cho, S. O. Fabrication and field-emission performance of zinc sulfide nanobelt arrays. *Journal of Physical Chemistry C* **2007**, *111*, 13385–13392.

(35) Du, J.; Yu, X. P.; Di, J. W. Comparison of the direct electrochemistry of glucose oxidase immobilized on the surface of Au, CdS and ZnS nanostructures. *Biosensors & Bioelectronics* **2012**, *37*, 88–93.

(36) Rajesh; Das, B. K.; Srinives, S.; Mulchandani, A. ZnS nanocrystals decorated single-walled carbon nanotube based chemiresistive label-free DNA sensor. *Applied Physics Letters* **2011**, *98*.

(37) Wood, V.; Halpert, J. E.; Panzer, M. J.; Bawendi, M. G.; Bulovic, V. Alternating Current Driven Electroluminescence from ZnSe/ZnS:Mn/ZnS Nanocrystals. *Nano Letters* **2009**, *9*, 2367–2371.

(38) Tang, X. S.; Yu, K. A.; Xu, Q. H.; Choo, E. S. G.; Goh, G. K. L.; Xue, J. M. Synthesis and characterization of $AgInS_2$-ZnS heterodimers with tunable photoluminescence. *Journal of Materials Chemistry* **2011**, *21*, 11239–11243.

(39) Fang, X. S.; Bando, Y.; Liao, M. Y.; Gautam, U. K.; Zhi, C. Y.; Dierre, B.; Liu, B. D.; Zhai, T. Y.; Sekiguchi, T.; Koide, Y.; Golberg, D. Single-Crystalline ZnS Nanobelts as Ultraviolet-Light Sensors. *Advanced Materials* **2009**, *21*, 2034–2039.

(40) Peng, Q. A.; Jie, J. S.; Xie, C.; Wang, L.; Zhang, X. W.; Wu, D.; Yu, Y. Q. Nano-Schottky barrier diodes based on Sb-doped ZnS nanoribbons with controlled p-type conductivity. *Applied Physics Letters* **2011**, *98*.

(41) Wang, X. F.; Xie, Z.; Huang, H. T.; Liu, Z.; Chen, D.; Shen, G. Z. Gas sensors, thermistor and photodetector based on ZnS nanowires. *Journal of Materials Chemistry* **2012**, *22*, 6845–6850.

(42) Wang, X. F.; Huang, H. T.; Liang, B.; Liu, Z.; Chen, D.; Shen, G. Z. ZnS Nanostructures: Synthesis, Properties, and Applications. *Critical Reviews in Solid State and Materials Sciences* **2013**, *38*, 57–90.

(43) Salles, R. C. M.; de Oliveira, G. C. G.; Diaz, S. L.; Barcia, O. E.; Mattos, O. R. Electrodeposition of Zn in acid sulphate solutions: pH effects. *Electrochimica Acta* **2011**, *56*, 7931–7939.

(44) Echendu, O. K.; Weerasinghe, A. R.; Diso, D. G.; Fauzi, F.; Dharmadasa, I. M. Characterization of n-Type and p-Type ZnS Thin Layers Grown by an Electrochemical Method. *Journal of Electronic Materials* **2013**, *42*, 692–700.

(45) Lay, M. D.; Varazo, K.; Stickney, J. L. Formation of sulfur atomic layers on gold from aqueous solutions of sulfide and thiosulfate: Studies using EC-STM, UHV-EC, and TLEC. *Langmuir* **2003**, *19*, 8416–8427.

(46) Colletti, L. P.; Thomas, S.; Wilmer, E. M.; Stickney, J. L. Thin layer electrochemical studies of ZnS, ZnSe, and ZnTe formation by electrochemical atomic layer epitaxy (ECALE). *Electrochemical Synthesis and Modification of Materials* **1997**, *451*, 235–244.

(47) Oznueluer, T.; Erdogan, I.; Demir, U. Electrochemically induced atom-by-atom growth of ZnS thin films: A new approach for ZnS co-deposition. *Langmuir* **2006**, *22*, 4415–4419.

Chapter 3

An EC-STM Study of Germanene Growth on Au(111) from Aqueous Solution, pH 9.0 [1]

[1] Bui, N.; Jung, J.; Reber, T.; Stickney, J. To be submitted to ACS Nano.

3.1 Abstract

Germanene is a 2D material whose structure and properties are of great interest for integration with Si technology. Preparation of germanene experimentally remains a challenge because unlike graphene, bulk germanene does not exist, thus germanene cannot be directly exfoliated and is mostly grown using molecular beam epitaxy (MBE) in UHV. The present report uses electrodeposition in an aqueous $HGeO_3^-$ solution, at pH 9. Germanene deposition has been limited to 2-3 monolayers, thus greatly restricting a number of applicable characterization methods. Moreover, these layers seem to be only stable in vacuum or under potential control in solution. The *in situ* technique of EC-STM was used to follow Ge deposition on Au(111) as a function of potential. Previous work by this group at pH 4.5 resulted in germanene growth. However, no buffer was used in that study, resulting in changes in surface pH during deposition. Use of pH 9 has reduced hydrogen formation and stabilizing the surface pH, allowing systematic characterization of germanene growth vs. potential. Initial germanene nucleated at defects in the Au(111) herringbone (HB) reconstruction. Subsequent growth proceeded down the face-center-cubic (fcc) troughs, slowly relaxing the HB. The resulting honeycomb (HC) structure displayed an average ring-to-ring distance of 0.41 ± 0.06 nm. Continued growth resulted in the addition of a second layer on top, formed initially by nucleating around small islands and subsequent lateral 2D growth. Near atomic resolution of the germanene layers displayed small coherent domains, 2-3 nm, of the HC structure composed of 6-membered rings. Domain walls were based on defective, 5- and 7-member rings, which resulted in small rotations between adjacent HC domains.

3.2 Introduction

Research concerning silicene and germanene continues to bring forward new understandings into their growth and properties.[1–5] With its high carrier mobility, topological insulating behavior, gapless edges, and monolayer size, germanene integration into Si technology is of great interest to the electronics industry.[6,7] Since its first introduction in 2009, germanene has been extensively studied from both theoretical[8,9] and experimental perspectives. A number of *ab initio* calculations have consistently suggested that a free-standing sheet of germanene should adopt some low-buckled structure, every other atom 0.06-0.07 nm higher than the other half,[6,10–13] and a bond distance of around 0.24 nm.[6,10,12] However, when germanene is supported on a substrate, a small variation in Ge-Ge distance was observed, not just in this study but also in others. For instance, germanene grew on Au(111) substrate seems to adopt a slightly longer bond distance of 0.256 nm.[14,15]

Generally, germanene is deposited using molecular beam epitaxy (MBE) on a metal substrate that has a lattice constant similar to germanene (a = 0.406 nm[13]). Germanene has been successfully grown on Au(111), Pt(111), Al(111), SiGe, Ge2Pt, and HOPG.[14–21] UHV has provided a clean, oxygen-free environment for the growth of germanene, preventing oxidation and contamination. However, UHV is seldom considered a scalable technology for production. Electrodeposition is a low-cost, scalable technique that can operate at low (room) temperature and at atmospheric pressure. The authors have been working on the development of electrochemical atomic layer deposition (E-ALD) for about 30 years. E-ALD is based on the principles of atomic layer deposition (ALD), where deposits are formed an atomic layer at a time, using surface limited reactions. Electrochemical surface limited reactions are referred to as underpotential deposition (UPD), where an atomic layer of an element is deposit prior to (under) the potential needed to deposit the element on itself. E-ALD is the com-

bination of UPD with ALD, which allows atomic level control in the electrochemical growth of nanofilms.[22]

The development of germanene electrodeposition was an outgrowth of research into design of an E-ALD cycle for the growth $Ge_xSb_yTe_z$, a phase change material, by this group.[23] At that time, questions were raised about the UPD growth of Ge. Most UPDs result in some fraction of a monolayer (ML), where a ML is defined in this report as one adsorbate for every substrate surface atom. Ge resulted in 2-3 ML, which remained an unexplained result until detailed studies using electrochemical scanning tunneling microscopy (EC-STM) were performed with the knowledge that germanene might be forming.[24] Unlike electrodeposition of Ge, bulk metal deposits are generally not limited. There are passivation processes that are limited to a few ML, but they tend to involve the oxidation of a surface, while Ge was formed by reduction from a GeO_2 solution. The amount of Ge deposited was also a function of pH, with pH 9.0 resulting in the highest Ge coverage.[23,25,26] The limited reactivity of Ge ions has been documented in studies using non-aqueous media as well.[27–29] There have been a number of studies concerning Ge electrodeposition since 1950.[23,27–49] Among them are in situ EC-STM studies by Enders et al., where the growth of Ge from ionic liquids and non-aqueous solutions were performed.[27–29] The studies presented here involved aqueous solutions, which greatly simplified the Ge deposition as highly-pure water is readily available.

Previous reports by this group of germanene electrodeposition on Au were performed at pH 4.5, with no buffer. The hydrogen evolution reaction (HER) at the potentials needed to deposit germanene limited the ability to obtain EC-STM images during the growth process. In addition, the absence of a buffer and the HER resulted in surface pH changes during the deposition, making identification of optimal conditions for germanene formation difficult to establish. For instance, to image the deposits in former reports, the potential was scanned back positively to where deposits could be

imaged in the absence of the HER, but negative enough that the germanene was not oxidized. This approach allows a transient capture of germanene on the surface, but with little reproducibility and high uncertainty in the potential at which the process had occurred. Even when using this strategy, the extensive HER during germanene deposition and the changes in surface pH made imaging challenging. Those issues suggested the use of a borate-buffered solution, pH 9.0, in the present study where imaging was performed during deposition as a function of potential. The resulting EC-STM images revealed the initial stages in germanene formation, as well as formation of the first honeycomb (HC) structure layer, and the growth of a second.

3.3 Experimental

3.3.1 Electrochemical Scanning Tunneling Microscopy (EC-STM)

All EC-STM images were collected under constant current mode (height mode) using Nanoscope III (Digital Instruments, Santa Barbara, CA). The electrochemical cell was set up with a three-electrode configuration. An Au wire was used as an auxiliary electrode and all potentials were referenced to an Ag/AgCl (3M NaCl) . The working electrode was an Au bead, carefully melted and annealed under H_2 atmosphere to create Au(111) facets. After each experiment, the Au bead was stored in concentrated nitric acid to remove any residuals. Tungsten wires, 0.25 mm diameter, were etched in 0.6 M KOH at 16 V AC for use as STM tips. The tips were coated with nail polish leaving only the apex exposed to solution. An O-ring sealed Plexiglas cover was placed on top of the cell and the scanning head, allowing maintenance of an inert N_2 environment. Height was checked using that expected for an Au step height, while x-y distances were compared with lines in a pristine Au Herringbone reconstructed surface. Ge solutions were made from 99.999% GeO_2 from Alfa Aesar. Electrolyte was 99.99% $KClO_4$ trace metal basis from Aldrich. $Na_2B_4O_7$ buffer was from Baker Analyzed ACS Reagent, 99.5%. Before the STM cell was assembled, solutions were

purged with nitrogen to exclude oxygen. Glassware cleaning and solution preparation were made use of 18 MΩ H_2O.

3.3.2 Cyclic Voltammetry (CV)

Cyclic voltammetry in GeO_2 solution was performed using a flow cell. The working electrode was 100 nm thick polycrystalline Au on 5 nm of Ti, on glass. Cleaning of Au slides was performed electrochemically in 0.1 M sulfuric acid solution. The GeO_2 solution was 1 mM, with 50 mM $KClO_4$, and 50 mM $Na_2B_4O_7$ buffer, to maintain the pH at 9.0.

3.4 Results and Discussion

3.4.1 Cyclic voltammetry

Figure 3.1 displays cyclic voltammograms (CVs) for a polycrystalline Au electrode in a pH 9.0 GeO_2 solution. The potential was scanned from OCP (0.1 V) to different negative window limits, where the potential was held for 500 sec. Ge deposition was a slow process, so the 500 sec was used to establish some form of equilibrium at the window limit potentials. The oxidation peak at -0.15 V corresponded to the dissolution of Ge in contact with the Au substrate, which might be thought of as UPD, though it was formed at an overpotential, -0.9 V. After holding at -0.95 V, a second oxidation peak appeared at -0.75 V. Subsequent STM images indicated that the -0.75 V peak corresponded to oxidation of small, 1-3 nm, islands, which served as nucleation sites for the growth of a second layer of germanene. Holding at -1.0 V resulted in a third oxidation peak, at -0.4 V, and sharpening of the other two oxidation peaks. STM images of deposits formed at -1.0 V displayed a nearly complete second layer of germanene.

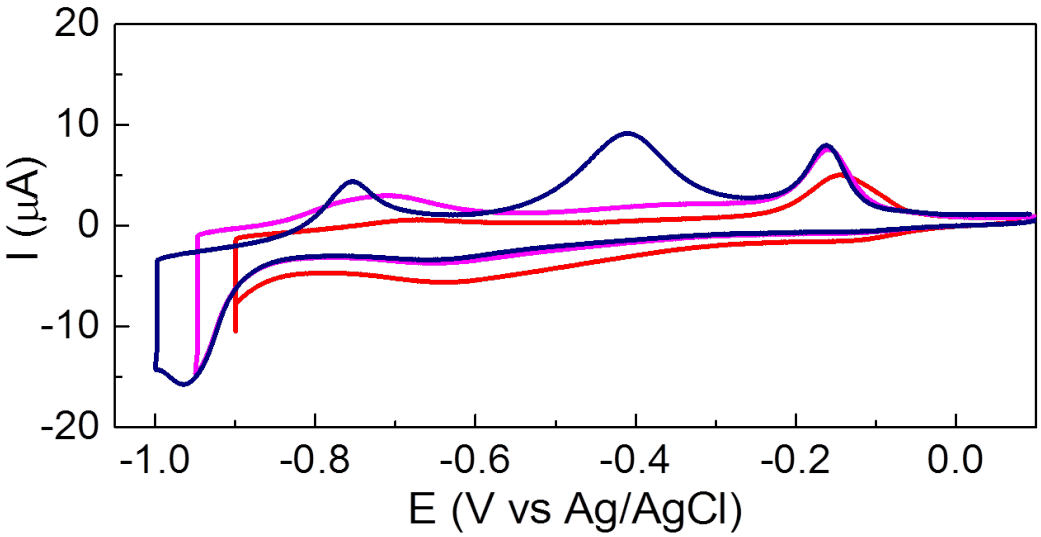

Figure 3.1: Cyclic voltammograms of a polycrystalline Au electrode in Ge solution at pH 9.0. Surface area was measured to be 0.268 cm^2. Scan rate was 10 $mV.s^{-1}$. The open circuit potential (OCP) was at 0.1 V. At each negative window limits, potential was held for 500 sec. Honeycomb structure of Germanene-like species was observed at -0.9 V. A 50 mV decrease in potential led to formation of small islands with 1.5 – 3 nm range in diameter and average height of 0.23 ± 0.01 nm. When the negative window opening reached -1.0 V, a third oxidative peak appeared at -0.4 V which corresponded to the dissolution of the second layer.

3.4.2 *In situ* STM RESULTS

Negative of -0.3 V, the Au(111) reconstructed into the ($22x\sqrt{3}$) herringbone (HB). Figure 3.2 displays examples of the Au(111) HB in the $HGeO_3^-$ solution. At potentials from -0.4 to -0.6 V there was no evidence of Ge deposition. In Figure 3.2(a), the Au step height was measured at 0.24 ± 0.01 nm. The distance between the corrugation lines separating face-center-cubic (fcc) and hexagonal-close-packed (hcp) domains was 2.2 ± 0.3 nm, while the corrugation in the HB structure was 0.02 ± 0.01 nm, consistent with literature values.[29,50]

From the voltammograms in Figure 3.1, it is clear that the kinetics of Ge electrodeposition were slow. While the OCP of the Au electrode in the pH 9.0 $HGeO_3^-$ solution was near 0.1 V, the deposition of Ge was not observable with STM until the potential was held at -0.7 V or below. At -0.7 V, Ge began to selectively deposit in fcc regions of the HB, near defects or bends (Figure 3.3a, b). At -0.8 V, Ge deposits grew along the fcc lines (Figure 3.3c), altering HB features. In some areas of the surface, it was either that the HB reconstruction did not form initially, or Ge deposition was accelerated. The pit with the triangular feature shown in Figures 3.3d-f is an example, as the higher surrounding terraces showed the HB with small domains of deposited Ge, but the bottom of the pit showed only deposited Ge. There are two other features of these images (Figures 3.3d-f) to take note of. First, the triangular feature appears to be missing a distinguishable step edge on the left, in contrast to the expected layered structure of the underlying Au(111) surface. Second, Figures 3.3e and f show small sets of Ge rings deposited in the pit, suggestive of germanene formation. The presence of a sheet of germanene would explain the missing Au step edge in the triangle. In the larger HB covered terraces (Figure 3.3), the slow kinetics of germanene deposition may result from the need to relax the HB reconstruction. Thus the absences of the HB in pits should accelerate germanene deposition (Figures 3.3d-f).

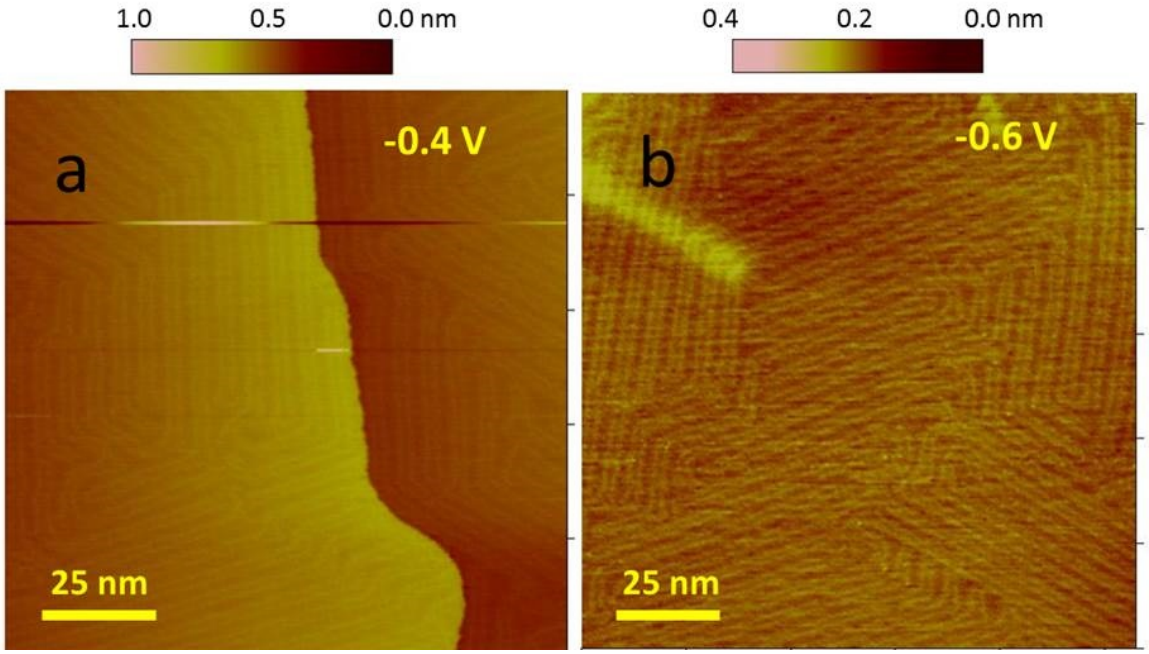

Figure 3.2: 22 x $\sqrt{3}$ Herringbone lines from pristine Au reconstruction observed in Ge solution at pH 9.0 for E from -0.4 V to -0.6 V. Au reconstruction starts at E < -0.3 V. (a) E = -0.4 V showing Au step height of 0.240 ± 0.008 nm. (b) E = -0.6 V. Distance between Herringbone lines was 2.2 ± 0.3 nm. Height between the higher and lower atoms was 0.02 ± 0.01 nm.

At this early stage of deposition, Figure 3.3f, the sheet of the germanene HC structure is made up of small coherent 2-3 nm domains, which might be considered a form of molecular germanene. The domains were partially connected, as there were areas between without the characteristic HC structure. The sizes of the molecules vary, as do their orientations with respect to each other and to the surface. It was assumed here that individual molecules were initiated at nucleation sites and grew laterally until they encountered neighboring molecules. Their growth appears to involve addition of Ge atoms to unhindered molecule edges by electroreduction, until steric effects became too great and adjacent molecules bond.

Figure 3.4a is the Au(111) surface after 45 min at -0.7 V. A few lines from the HB still remained, but they had changed directions and were bending as the germanene coverage increased. Germanene rings are evident between sets of HB lines (fcc regions). The HB hcp ridges appeared to prevent lateral expansion of germanene from the fcc domains. The remaining images, Figures 3.4b-d, were obtained at -0.8 V, but with a few series of short 3-s pulses to -0.9 V, showing a great increase in the deposition kinetics. In Figure 3.4b, small germanene bridges appeared to grow across the remaining HB hcp ridges. The short potential steps eventually resulted in covering most of the surface (Figures 3.4c and d), although germanene HC was still absent from a few patches. The germanene HC structure is clearly evident in Figure 3.4d.

Figures 3.5a-d display the surface when shifting the potential from -0.8 V to -0.9 V, over 11 min. During the initial stage at 0.9 V (Figure 3.5b), the germanene domains slowly displaced the remaining HB features, resulting in small islands at 1.5 – 3 nm in diameter and 0.23 $\pm$ 0.01 nm in height. Au atoms extruded from the relaxing HB appeared to produce roughly 4% of a ML of extra Au on the surface. HC structure of germanene was also observed on those Au islands. A complete first layer of germanene would typically form in less than 10 min at -0.9 V.

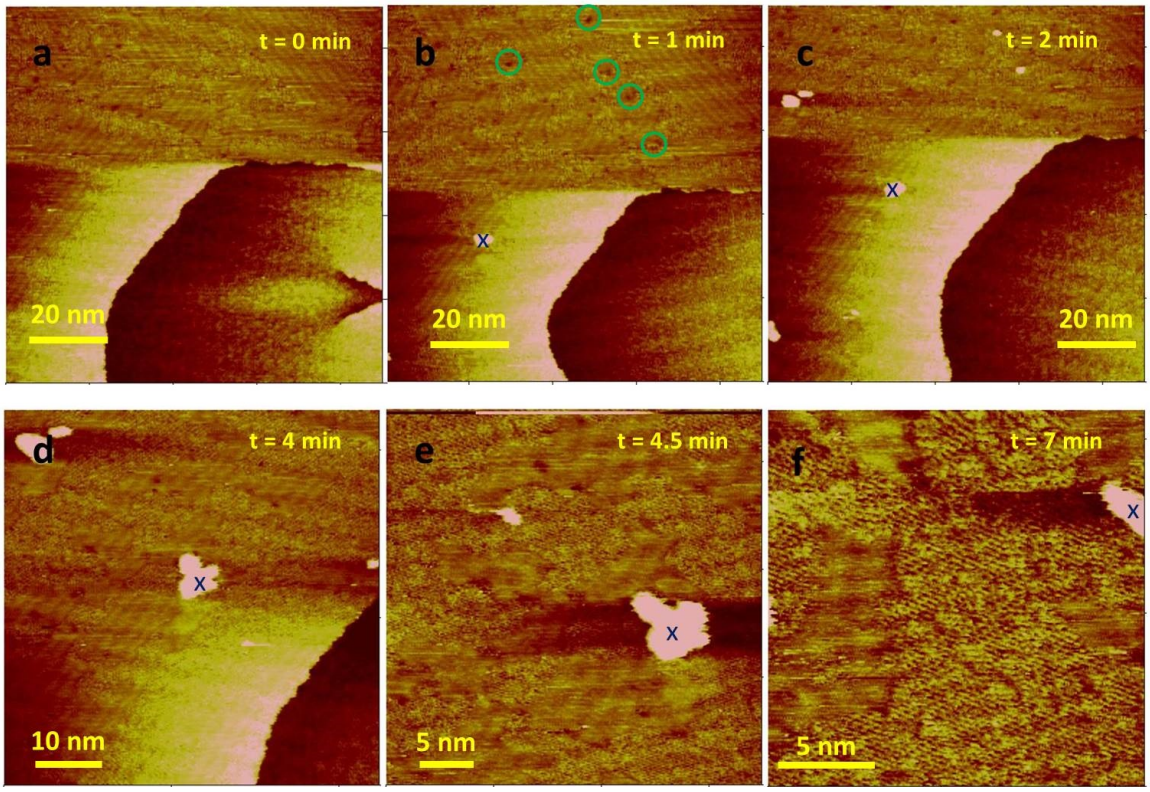

Figure 3.3: Images as the potential was decreased from -0.7 V to -0.85 V. Ge deposits formed slowly, only between ridges of HB. (a) E = 0.7 V, t = 0 min. (b) E = -0.7 V, t = 1 min. (c) E = -0.8 V, t = 11 min. In the region where there was no reconstruction initially, Ge deposited more readily. Images (d), (e), and (f) were of the same area at -0.85 V, but with increasing magnification. Small rings of germanene are evident in image (f).

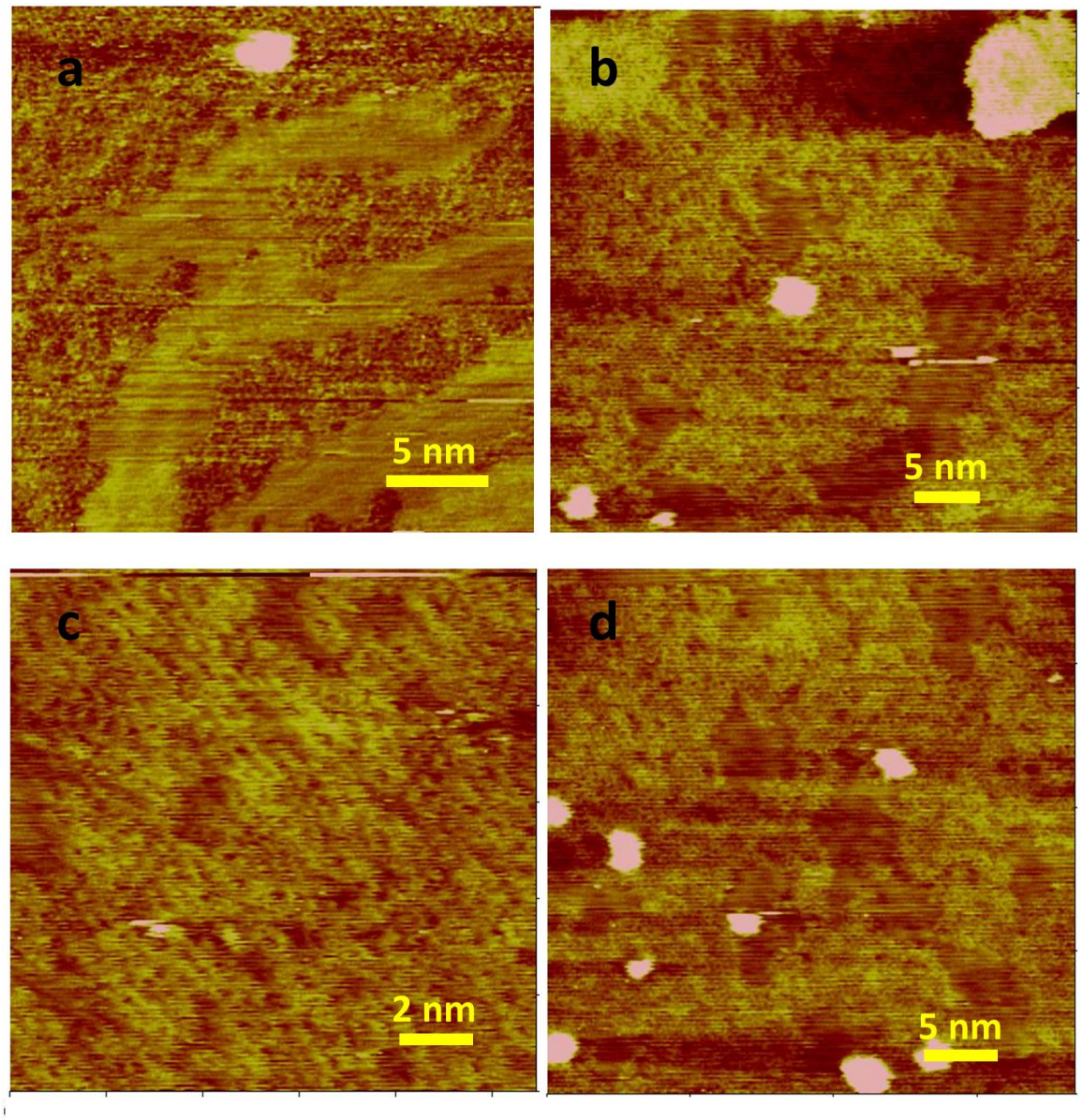

Figure 3.4: HB lines became more disordered as more Ge deposited. (a) E = -0.7 V, t = 45 min, showing "molecular" germanene, which formed only in the fcc region of the Au HB reconstruction. The germanene was disorder and did not appear to have a sufficient overpotential to replace the HB hcp Au ridges. (b), (c), (d) E = -0.8 V. An increasing number of short pulses to -0.9 V were applied from (b) to (d) which eventually removed the HB lines and covered the surface with germanene.

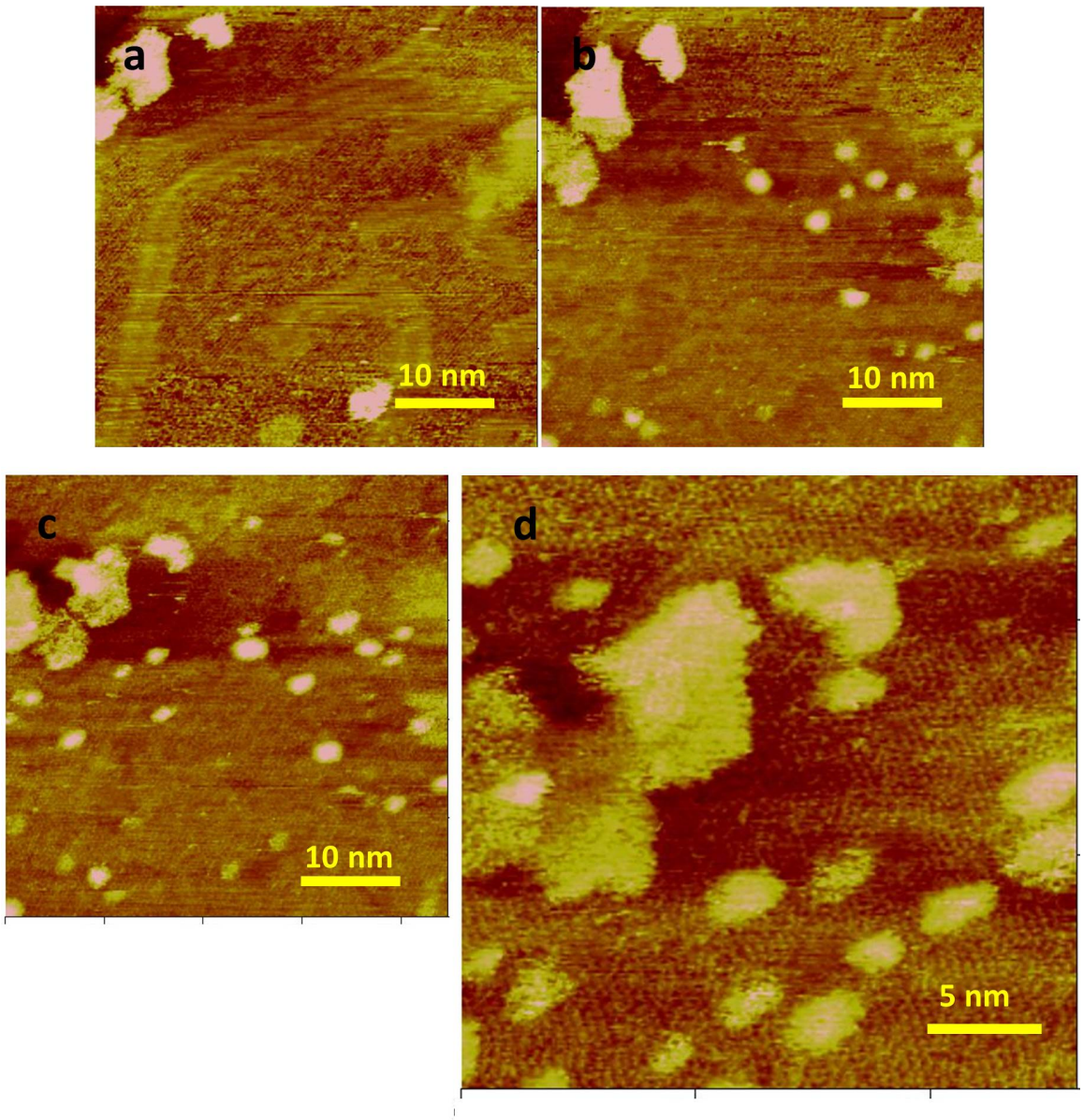

Figure 3.5: Transition from a first layer of germanene on the Au(111) surface, with some evidence of the HB reconstruction, to the nucleation of islands of second layer germanene. (a) E = -0.8 V, t = 0 min. (b) E = -0.9 V, t = 2 min. (c) E = -0.9 V, t = 3 min. (d) E = -0.9 V, t = 11 min.

In addition to the germanene covered Au(111) islands, there were some smaller and slightly lower islands (showing mostly as yellow in Figure 3.5). The authors believe them to have been nucleation of a second germanene layer. Those small germanene islands appeared to move from image to image, which is consistent with the weak forces keeping them on the first layer of germanene. The density of the small germanene islands was somewhat dependent on the tip potential. The more negative the tip potential, the closer the tip approached the surface, and the higher the coverage of the germanene islands, which was previously observed by Endres et al. in their study of Ge deposition in ionic liquids.[29] Those results suggested that the islands might be germanene formed on the tip, and transferred onto the surface during imaging.

Characterization of the first germanene layer, as formed at -0.9 V, revealed hexagonal arrays of six-membered rings, consistent with the HC structure (Figure 3.6). However, their coherence lengths were short range (2-3 nm), due to the ring rotations occurring at the domain walls, where defects with five-, seven- or eight-membered rings would form. Previous in situ surface X-ray diffraction studies of similar deposits indicated the presences of the layers, but the low coherence lengths prevented identification of the unit cell.

The deposit formed at -0.9 V suggests that when the coherent domains come together and bond, their orientation are seldom positioned or rotated to facilitate formation of six-membered rings, thus preventing the formation of larger domain of coherent HC germanene. The contact orientations between molecules of germanene end up creating the defect rings with sizes other than six during bond formation, resulting in the observed disorder in the germanene layers. In the coherent domains with the HC structure, the ring-to-ring distance was measured to be 0.41 ± 0.06 nm, using the FFT inverse space of the surface image at -0.9 V (Supporting Information). The lattice constant for a free-standing sheet of germanene was predicted to be around 0.41 nm, which corresponds to an interatomic distance of 0.24 nm.[6,10–13]

Several studies also suggest that germanene grown on Au adopted a slightly longer bond length compared to that of a free-standing sheet, the result of a slightly higher interaction energy with the Au surface lattice.[14,15] Besides those islands that formed from Au atoms displaced by relaxation of the HB reconstruction, or any Ge transferred from the tip, the first germanene layer would be consistent formation of Ge UPD on the Au surface. Longer exposure to -0.9 V did not induce further growth.

Figures 3.7a-c were recorded over a 5-min period, where the potential was held at -0.9 V, and the surface was repeatedly imaged. The number of small islands increased from one to eight. It is proposed by the authors that the germanene deposited on the tip, which was negative of -0.9 V, and periodically transferred to the surface, producing the small islands of second layer germanene. In Figure 3.8 the potential was stepped from -0.9 V (Figures 3.8a and b) to -1.1 V (Figure 3.8c). In the two minutes between Figure 3.8a and 3.8b there was an increase in the number of small germanene islands formed at the top of the image. In Figure 3.8c the potential was stepped to -1.1 V near the top of the downward scan. At the top of the scan the islands can be seen to grow laterally, while toward the bottom of the image the deposits has become very disordered, with three or more layers of germanene in some spots, and a chaotic distribution of very small particles over the surface.

Subsequent studies indicate that deposition at -1.0 V result in a slower growth and smoother germanene layers. Figure 3.9a is an image of a Au(111) surface equilibrated at -0.9 V in the $HGeO_3^-$ solution, to cover the substrate with a smooth first layer of germanene, though it does displays a number of the small islands previously discussed. No other growth was evident. Figure 3.9b is an image of the growth of the second layer of germanene, 14 min after stepping negative to -1.0 V. The second layer covers about 75% of the surface with 10 nm islands. The second layer growth at -1.0 V was 2D and slow, as opposed to deposits grown at -1.1 V where the surface became covered with 1-3 nm clusters, multiple layers thick and chaotic (Figure 3.8c). Figure

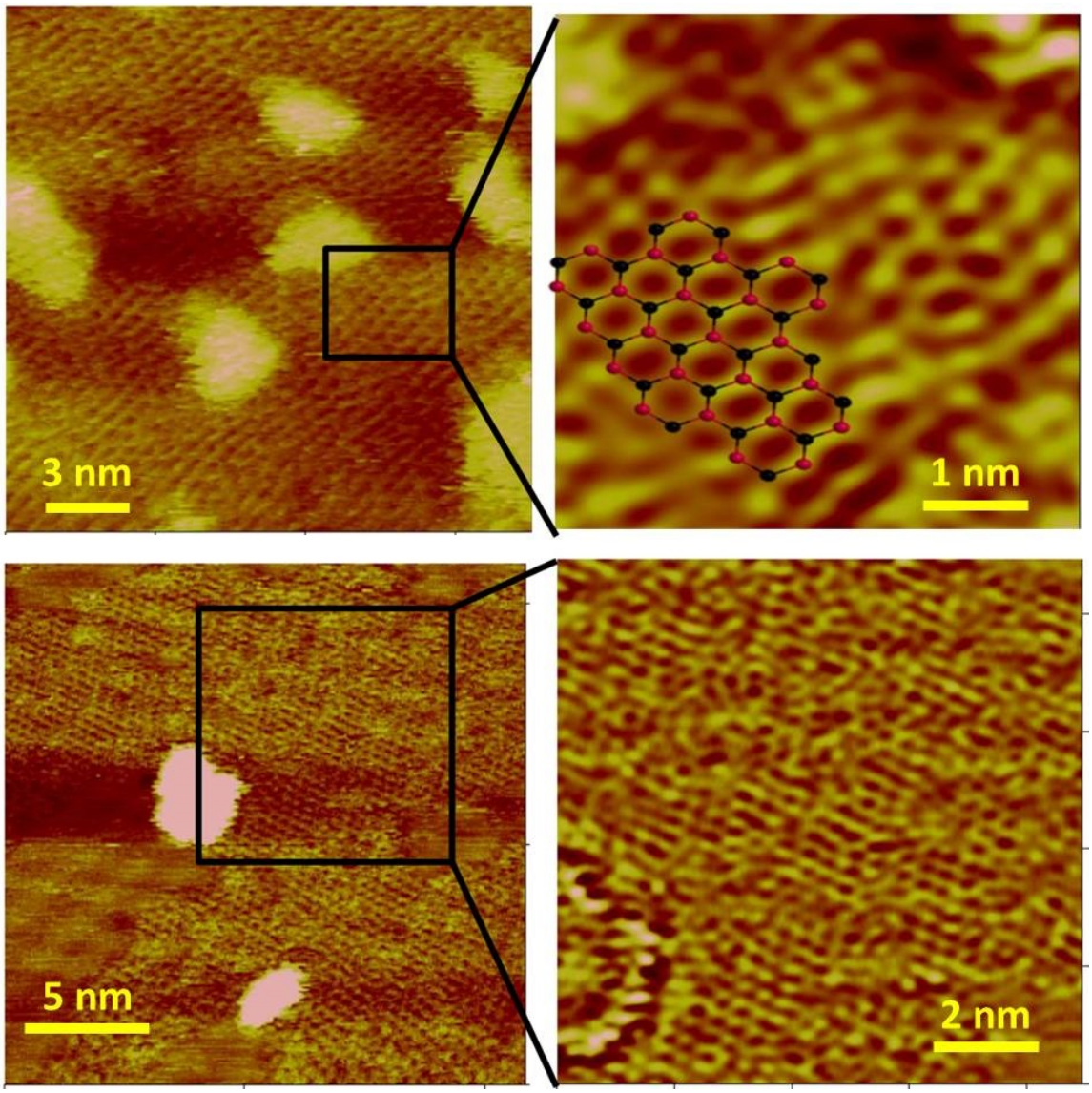

Figure 3.6: At -0.9 V, a complete first layer of germanene was formed. Near atomic resolution images showed distinct honeycomb structure with a ring separation of 0.41 ± 0.06 nm. Rotations between coherent domains resulted from the presences of domain walls consisting of 5 and 7 membered rings, rather than ideal 6, the result of an initially high density of nucleation sites. As the nuclei grew laterally, steric issues resulted in the formation of the alternate ring sizes and rotations between coherent domains.

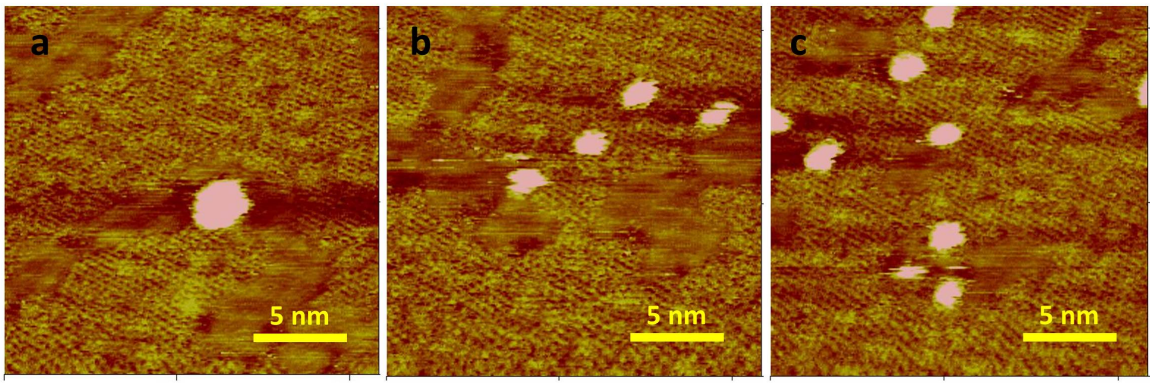

Figure 3.7: E = -0.9 V: (a) t = 0 min, (b) t = 3 min, and (c) t = 5 min. A number of small, similarly sized, islands formed on the surface as the surface was repeatedly scanned. They appear to be germanene transferred to the surface from the tip, and moved during imaging.

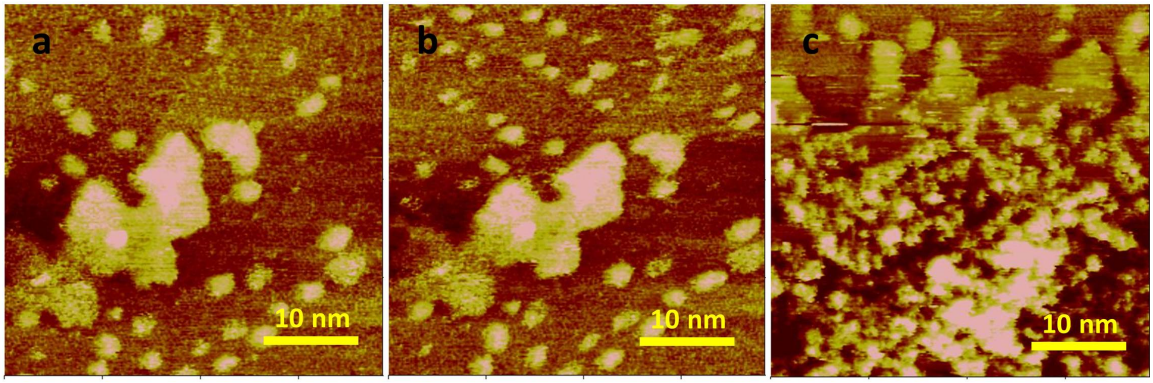

Figure 3.8: Increasing number of small islands during growth at -0.9 V. Stepping the potentials to -1.1 V resulted in faster, more chaotic growth and roughening. (a) E = -0.9 V, t = 0 min. (b) E = -0.9 V, t = 2 min. (c) E = -1.1 V, t = 3 min.

3.9c is the surface after two more minutes at -1.0 V. Some small areas of first layer germanene can still be seen, but second layer has covered the majority of the surface. Similar to the growth of the first germanene layer, the germanene islands of the second layer appear to have had some difficulty connecting with each other at the edges to complete a second sheet. Figure 3.9d shows further 2D growth of the second layer after 3 more minutes at -1.0 V. Lines in yellow on the upper terrace are suggestive of the formation of third layer germanene, a process that continues in Figures 3.9e and f.

At -0.9 V the first layer of germanene grows in, eventually covering the Au and all nucleation sites available. The second layer develops and expands at -1.0 V, as noted above, following a 2D mechanism. In the absence of available Au sites during second layer growth, nucleation is built upon the small Au islands formed during relaxation of the HB reconstruction. Moreover, similar to the electrodeposition on HOPG and graphene, unless there are defects or oxidized sites, growth does not generally take place on the basal plane but instead occurring at edge sites. As a result, with the Au surface already covered by first layer germanene, growth of the second layer at -1.0 V starts both at expelled Au islands and edge sites. In addition, formation of a junction between two germanene islands may be limited by their ability to align and bond with each other. Instead, it would be much more likely for a $HGeO_3^-$ ion to encounter a second layer germanene edge site and be reductively deposited.

The above discussion raises questions about growth of a third layer of germanene. Visual inspection of 3.9d-f suggests "fish scales" to the authors. It was assumed here that the first and second layers of germanene were only held together weakly by van der Waals forces. If bonding between islands was not as favored as 2D edge growth, a new second layer island might get inserted and sandwiched between the first layer and another second layer island, creating the observed "fish scales". The insertion would take place at island edges, accounting for the line features that look like a third layer

in Figures 3.9d-f. Figure 3.9g is a larger image over the area displayed in Figures 3.9e and f. It shows a denser packing where the surface was previously scanned, suggesting that the STM tip had some effect on second layer germanene growth, under the conditions used. Figure 3.9h was of the area not imaged previously, and it looks closer to the disconnected islands in Figure 3.9c. Comparison of Figures 3.9g and 3.9h clearly shows that tip has somewhat facilitated the growth of germanene second layer. Given the tendency for the tip to leave small germanene islands on the first layer (Figures 3.7 and 3.8) and the mobility of those islands, the higher density of the second layer where imaging was repeated is understandable.

Figure 3.10 displays images of a surface formed at -1.0 V, similar to those in Figures 9, and potential was then stepped to -1.1 V and -1.2 V (Figures 3.10b and c) over 5 min. The deposition process involves growth of some third layer germanene islands, as well as a series of 5 nm pits. The coarsening of the surface in Figures 3.10b and c was triggered by the increasingly reductive potentials applied, which expedited the deposition rate and interleaving of the growing germanene islands. At the same time, hydrogen evolution increased at those lower potentials, possibly producing small bubbles on the surface at spots with better access to the Au substrate. Bubble evolution would explain pit formation, if they lifted germanene flakes from the surface. Figure 3.10 suggests that higher quality deposits result at less negative potentials where growth is slower (Figure 3.9), and hydrogen evolution is minimized, limiting disruption of the weakly held second germanene layer.

Figure 3.11 shows the first layer of germanene with a few of the smaller second layer islands, and their oxidation. Figure 3.11a was taken at -0.7 V, prior to significant oxidation of the surface, and shows the 6-member ring HC structure with 2-3 nm coherent domains of germanene. At -0.6 V, the HC structure was still present, but with considerably increased disorder (Figure 3.11b). The disordering increased further by -0.4 V (Figure 3.11c), unfortunately with decreased image clarity. Overall, the majority

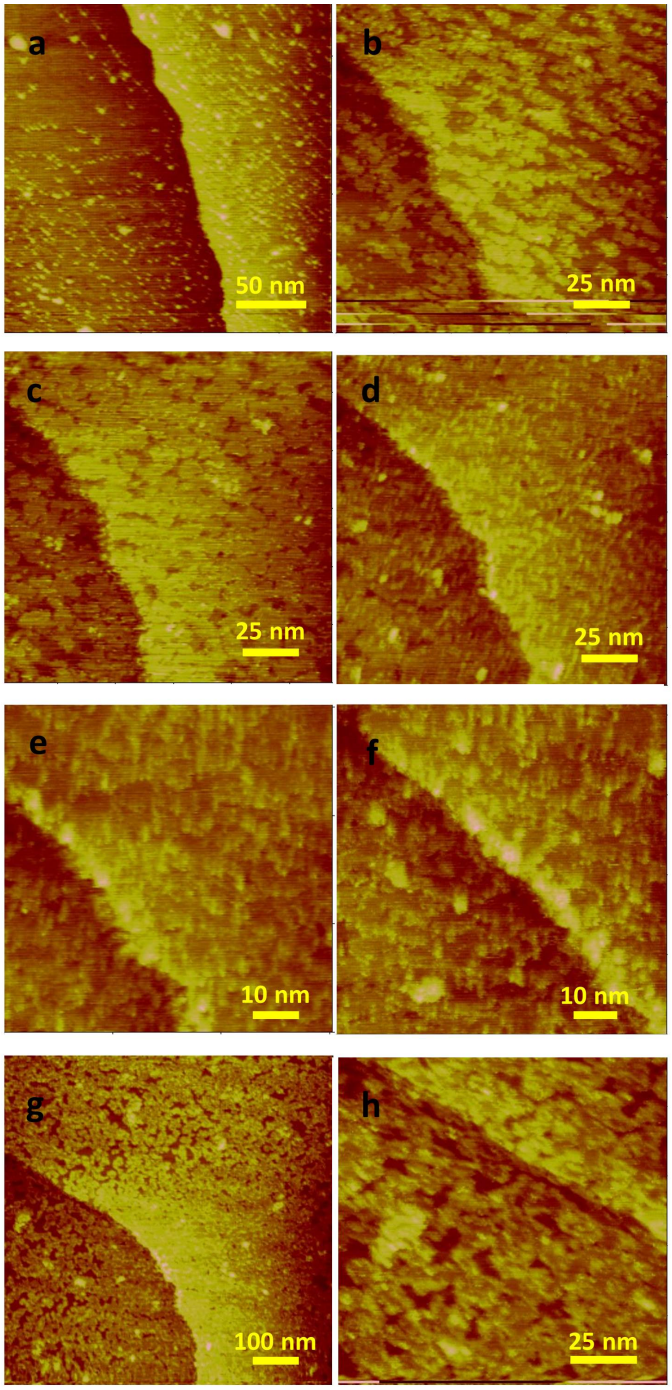

Figure 3.9: Ge second layer formation from -0.9 V to -1.0 V. (a) E = -0.9 V, t = 0 min. (b) E = -1.0 V, t = 14 min after stepping to -1.0 V. Image shows lateral expansion of second layer germanene islands, till they cover 75% of the surface. (c) E = -1.0 V, t = 16 min. (d) E = -1.0 V, t = 19 min. Lines at the edges of second layer islands begin to appear, giving a "scalar" appearance associated with insertion of second layer islands under other second layer islands. (e) E = 1.0 V, t = 21 min. (f) E = -1.0 V, t = 24 min. (g) E = -0.9 V, t = 35 min, an enlargement of the area imaged in (f). (h) E = -1.0 V, t = 40 min is an area which had not previously been imaged. Figures (g) and (h) indicate that higher coverages are formed under areas which were repeatedly scanned, suggesting a tip effect.

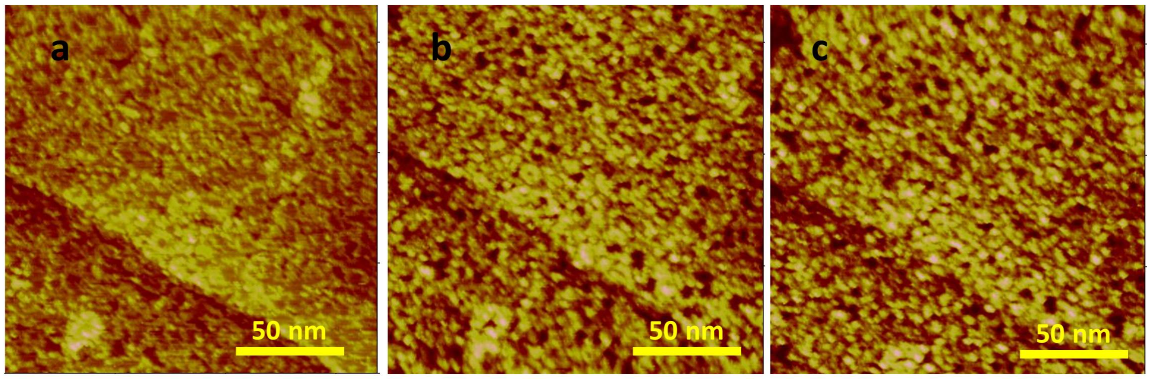

Figure 3.10: Transition to the hydrogen evolution region by shifting the potential from -1.0 V to -1.2 V. (a) E = -1.0 V, t = 0 min. (b) E = -1.1 V, t = 2 min. (c) E = -1.2 V, t = 5 min. The small pits appear to be where hydrogen bubbles were formed.

of the germanene was still present at -0.4 V, but the disorder suggest oxidation did take place, possibly forming a material analogous to graphene oxide. Figure 3.11c also displayed a step edge where a layer of germanene appeared to cover a portion of the step.

3.5 Conclusion

Growth of Germanene in pH 9.0 aqueous solution containing $HGeO_3^-$ ions was investigated using *in situ* STM. The presences of a borate buffer shifted the hydrogen evolution reaction negatively and prevented changes in the surface pH during deposition. Germanene grew slowly at potentials between -0.7 and -0.8 V, and selectively. Most of the surface supported the HB reconstruction, and germanene grew first at defects and in the fcc region of the HB on the Au(111) substrate. Evidence was presented suggesting that in areas of the surface not covered by the HB, the growth of germanene was accelerated, such as the bottom of small pits. The kinetics on the HB were much slower, with germanene growth following the fcc domains. At -0.9 V, germanene was able to also grow into the hcp domains of the HB, forming sheets composed of small coherent "molecular" germanene, 2-3 nm in size, connected to each other, but rotated. The coherent molecular germanene, composed of 6-membered rings, were surrounded by defects in the form of 5 and 7 membered rings, which were responsible for small rotations between coherent domains of germanene. The first germanene layer showed a lattice constant of 0.41 ± 0.06 nm, corresponding to a Ge-Ge distance of 0.24 nm, which was consistent with theoretical calculation of germanene.[10, 16, 18] Subsequent deposition at -1.0 V produced a second layer of germanene, which grew by nucleating at the edges of small islands. It is suggested here that bonding between individual islands was less favorable, and that islands would sometimes grow under or over the edges of adjacent islands, depending on the tunneling conditions. Use of more negative deposition potentials resulted in roughening and disordering of the deposit, as well

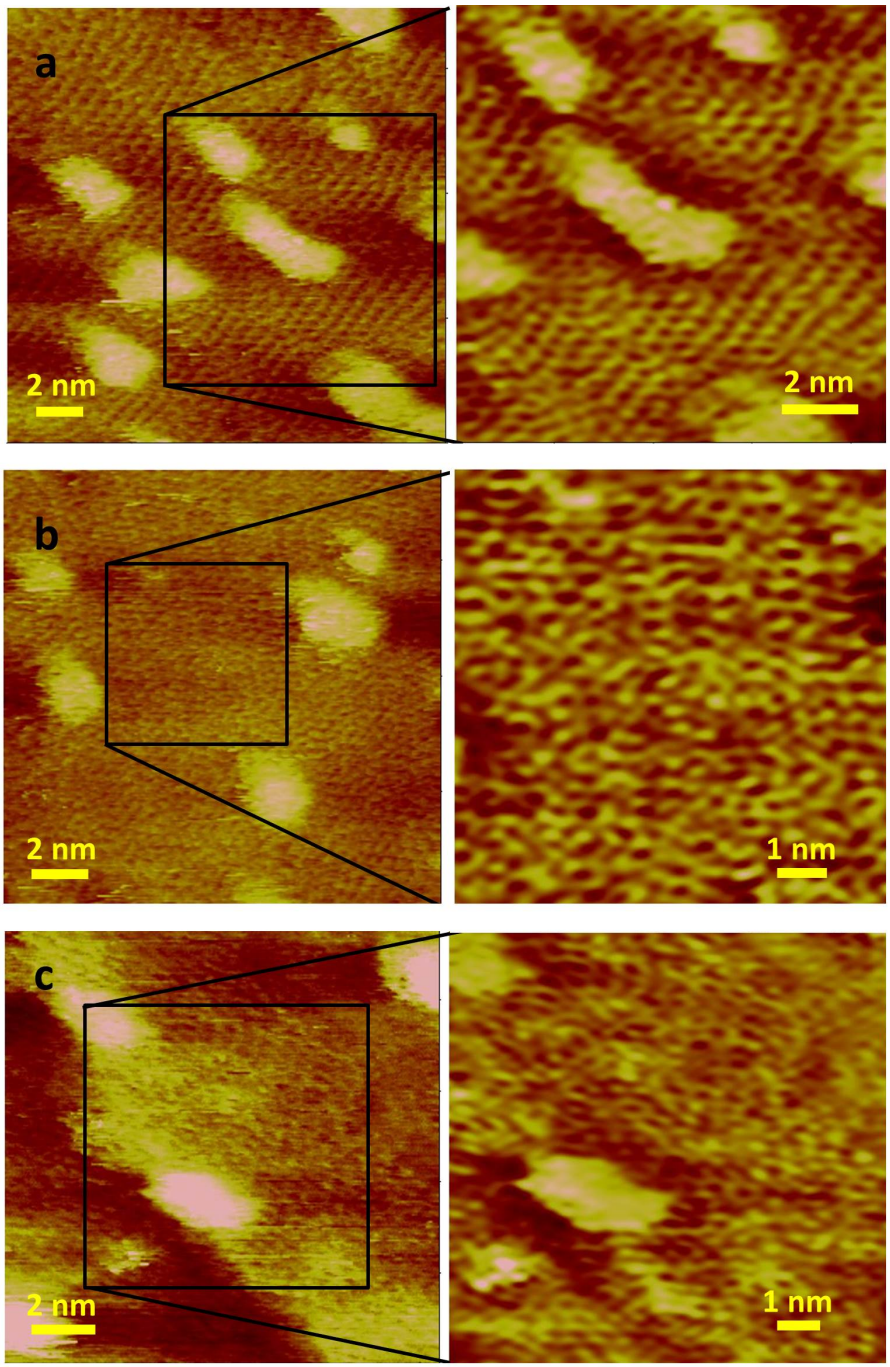

Figure 3.11: Oxidation of first layer germanene formed at -0.9 V. (a) E = -0.7 V. (b) E = -0.6 V. (c) E = 0.4. V. As potential was shifted progressively positive, the HC structures became increasingly disordered. Figure (c) appears to show a feature at a step edge where germanene layer grew like a sheet, extending over the step edge. Even with the disordering of the deposit at the more positive potentials, germanene rings were still present as positive as -0.4 V.

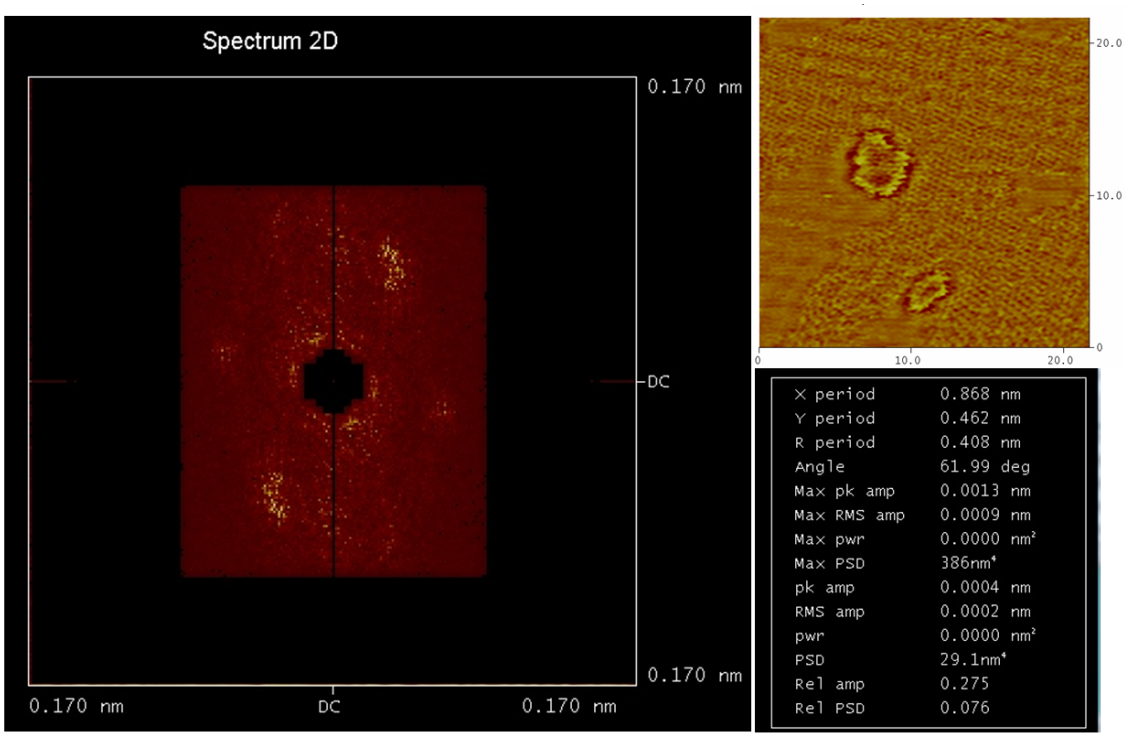

Figure 3.12: FFT analysis of Figure 6 image. Lattice periodicity is 0.41 ± 0.06 nm.

as the formation of some small pits, presumably due to hydrogen bubbles dislodging pieces of the germanene. Oxidation of the first layer of germanene tended to disorder the HC structure of the surface, but did little to decrease the Ge coverage, even at -0.4 V. It is assumed that some of the bonds present in the defective domain walls were probably more susceptible to oxidation than others, leaving a sufficient number of bonds to retain most of the first germanene layer.

3.6 Acknowledgments

Acknowledgement is made to the National Science Foundation, DMR # 1410109.

References

(1) Meng, L.; Wang, Y. L.; Zhang, L. Z.; Du, S. X.; Wu, R. T.; Li, L. F.; Zhang, Y.; Li, G.; Zhou, H. T.; Hofer, W. A.; Gao, H. J. Buckled Silicene Formation on Ir(111). *Nano Letters* **2013**, *13*, 685–690.

(2) Vogt, P.; De Padova, P.; Quaresima, C.; Avila, J.; Frantzeskakis, E.; Asensio, M. C.; Resta, A.; Ealet, B.; Le Lay, G. Silicene: Compelling Experimental Evidence for Graphenelike Two-Dimensional Silicon. *Physical Review Letters* **2012**, *108*.

(3) Fleurence, A.; Friedlein, R.; Ozaki, T.; Kawai, H.; Wang, Y.; Yamada-Takamura, Y. Experimental Evidence for Epitaxial Silicene on Diboride Thin Films. *Physical Review Letters* **2012**, *108*.

(4) Molle, A.; Grazianetti, C.; Chiappe, D.; Cinquanta, E.; Cianci, E.; Tallarida, G.; Fanciulli, M. Hindering the Oxidation of Silicene with Non-Reactive Encapsulation. *Advanced Functional Materials* **2013**, *23*, 4340–4344.

(5) Bianco, E.; Butler, S.; Jiang, S. S.; Restrepo, O. D.; Windl, W.; Goldberger, J. E. Stability and Exfoliation of Germanane: A Germanium Graphane Analogue. *ACS Nano* **2013**, *7*, 4414–4421.

(6) Roome, N. J.; Carey, J. D. Beyond Graphene: Stable Elemental Monolayers of Silicene and Germanene. *ACS Applied Materials & Interfaces* **2014**, *6*, 7743–7750.

(7) Ezawa, M. Monolayer Topological Insulators: Silicene, Germanene, and Stanene. *Journal of the Physical Society of Japan* **2015**, *84*.

(8) Marjaoui, A.; Stephan, R.; Hanf, M. C.; Diani, M.; Sonnet, P. Tailoring the germanene-substrate interactions by means of hydrogenation. *Physical Chemistry Chemical Physics* **2016**, *18*, 15667–15672.

(9) Liu, G.; Liu, S. B.; Xu, B.; Ouyang, C. Y.; Song, H. Y. First-principles study of the stability of free-standing germanene in oxygen atmosphere. *Journal of Applied Physics* **2015**, *118*.

(10) Scalise, E.; Houssa, M.; Pourtois, G.; van den Broek, B.; Afanas'ev, V.; Stesmans, A. Vibrational properties of silicene and germanene. *Nano Research* **2013**, *6*, 19–28.

(11) Nijamudheen, A.; Bhattacharjee, R.; Choudhury, S.; Datta, A. Electronic and Chemical Properties of Germanene: The Crucial Role of Buckling. *Journal of Physical Chemistry C* **2015**, *119*, 3802–3809.

(12) Cahangirov, S.; Topsakal, M.; Akturk, E.; Sahin, H.; Ciraci, S. Two- and One-Dimensional Honeycomb Structures of Silicon and Germanium. *Physical Review Letters* **2009**, *102*.

(13) Seixas, L.; Padilha, J. E.; Fazzio, A. Quantum spin Hall effect on germanene nanorod embedded in completely hydrogenated germanene. *Physical Review B* **2014**, *89*.

(14) Davila, M. E.; Xian, L.; Cahangirov, S.; Rubio, A.; Le Lay, G. Germanene: a novel two-dimensional germanium allotrope akin to graphene and silicene. *New Journal of Physics* **2014**, *16*.

(15) Davila, M. E.; Le Lay, G. Few layer epitaxial germanene: a novel two-dimensional Dirac material. *Scientific Reports* **2016**, *6*.

(16) Bampoulis, P.; Zhang, L.; Safaei, A.; van Gastel, R.; Poelsema, B.; Zandvliet, H. J. W. Germanene termination of Ge2Pt crystals on Ge(110). *Journal of Physics-Condensed Matter* **2014**, *26*.

(17) Derivaz, M.; Dentel, D.; Stephan, R.; Hanf, M. C.; Mehdaoui, A.; Sonnet, P.; Pirri, C. Continuous Germanene Layer on Al (111). *Nano Letters* **2015**, *15*, 2510–2516.

(18) Li, L. F.; Lu, S. Z.; Pan, J. B.; Qin, Z. H.; Wang, Y. Q.; Wang, Y. L.; Cao, G. Y.; Du, S. X.; Gao, H. J. Buckled Germanene Formation on Pt(111). *Advanced Materials* **2014**, *26*, 4820–+.

(19) Tsai, H. S.; Chen, Y. Z.; Medina, H.; Su, T. Y.; Chou, T. S.; Chen, Y. H.; Chueh, Y. L.; Liang, J. H. Direct formation of large-scale multi-layered germanene on Si substrate. *Physical Chemistry Chemical Physics* **2015**, *17*, 21389–21393.

(20) Stephan, R.; Hanf, M. C.; Derivaz, M.; Dentel, D.; Asensio, M. C.; Avila, J.; Mehdaoui, A.; Sonnet, P.; Pirri, C. Germanene on Al(111): Interface Electronic States and Charge Transfer. *Journal of Physical Chemistry C* **2016**, *120*, 1580–1585.

(21) Persichetti, L.; Jardali, F.; Vach, H.; Sgarlata, A.; Berbezier, I.; De Crescenzi, M.; Balzarotti, A. van der Waals Heteroepitaxy of Germanene Islands on Graphite. *Journal of Physical Chemistry Letters* **2016**, *7*, 3246–3251.

(22) Stickney, J. L.; Villegas, I.; Suggs, D. W.; Gregory, B. W. Electrochemical Atomic Layer Epitaxy (ECALE). *Abstracts of Papers of the American Chemical Society* **1991**, *201*, 289–Coll.

(23) Liang, X. H.; Kim, Y. G.; Gebergziabiher, D. K.; Stickney, J. L. Aqueous Electrodeposition of Ge Monolayers. *Langmuir* **2010**, *26*, 2877–2884.

(24) Ledina, M. A.; Liang, X.; G. Kim, Y.; Jung, J.; B., P.; Tsang, C.; Soriaga, M.; Stickney, J. L. Investigations into the Formation of Germanene using Electrochemical Atomic Layer Deposition (E-ALD). *ECS Transaction* **2015**, *66*, 129–140.

(25) Liang, X. H.; Jayaraju, N.; Thambidurai, C.; Zhang, Q. H.; Stickney, J. L. Controlled Electrochemical Formation of GexSbyTez using Atomic Layer Deposition (ALD). *Chemistry of Materials* **2011**, *23*, 1742–1752.

(26) Liang, X. H.; Zhang, Q. H.; Lay, M. D.; Stickney, J. L. Growth of Ge Nanofilms Using Electrochemical Atomic Layer Deposition, with a "Bait and Switch" Surface-Limited Reaction. *Journal of the American Chemical Society* **2011**, *133*, 8199–8204.

(27) Endres, F. Electrodeposition of a thin germanium film on gold from a room temperature ionic liquid. *Physical Chemistry Chemical Physics* **2001**, *3*, 3165–3174.

(28) Endres, F.; El Abedin, S. Z. Nanoscale electrodeposition of germanium on Au(111) from an ionic liquid: an in situ STM study of phase formation - Part I. Ge from GeBr4. *Physical Chemistry Chemical Physics* **2002**, *4*, 1640–1648.

(29) Endres, F.; El Abedin, S. Z. Nanoscale electrodeposition of germanium on Au(111) from an ionic liquid: an in situ STM study of phase formation - Part II. Ge from GeCl4. *Physical Chemistry Chemical Physics* **2002**, *4*, 1649–1657.

(30) Al-Salman, R.; Mallet, J.; Molinari, M.; Fricoteaux, P.; Martineau, F.; Troyon, M.; El Abedin, S. Z.; Endres, F. Template assisted electrodeposition of germanium and silicon nanowires in an ionic liquid. *Physical Chemistry Chemical Physics* **2008**, *10*, 6233–6237.

(31) Carim, A. I.; Gu, J. S.; Maldonado, S. Overlayer Surface-Enhanced Raman Spectroscopy for Studying the Electrodeposition and Interfacial Chemistry of Ultrathin Ge on a Nanostructured Support. *ACS Nano* **2011**, *5*, 1818–1830.

(32) Chandrasekharan, N.; Sevov, S. C. Anodic Electrodeposition of Germanium Films from Ethylenediamine Solutions of Deltahedral Ge-9(4-) Zintl Ions. *Journal of the Electrochemical Society* **2010**, *157*, C140–C145.

(33) Cummings, C. Y.; Bartlett, P. N.; Pugh, D.; Reid, G.; Levason, W.; Hasan, M. M.; Hector, A. L.; Spencer, J.; Smith, D. C. Supercritical Fluid Electrodeposition of Elemental Germanium onto Titanium Nitride Substrates. *Journal of the Electrochemical Society* **2015**, *162*, D619–D624.

(34) Cummings, C. Y.; Bartlett, P. N.; Pugh, D.; Reid, G.; Levason, W.; Hasan, M. M.; Hector, A. L.; Spencer, J.; Smith, D. C.; Marks, S.; Beanland, R. Electrodeposition of Protocrystalline Germanium from Supercritical Difluoromethane. *Chemelectrochem* **2016**, *3*, 726–733.

(35) Endres, F. Electrodeposition of nanosized germanium from GeBr4 and GeCl4 in an ionic liquid. *Electrochemical and Solid State Letters* **2002**, *5*, C38–C40.

(36) Endres, F. The electrodeposition of germanium from an ionic liquid: A minireview on the nanoscale processes. *Physical Chemistry Chemical Physics* **2002**, *2002*, 677–689.

(37) Endres, F.; El Abedin, S. Z. Electrodeposition of stable and narrowly dispersed germanium nanoclusters from an ionic liquid. *Chemical Communications* **2002**, 892–893.

(38) Fahrenkrug, E.; Gu, J. S.; Jeon, S.; Veneman, P. A.; Goldman, R. S.; Maldonado, S. Room-Temperature Epitaxial Electrodeposition of Single-Crystalline Germanium Nanowires at the Wafer Scale from an Aqueous Solution. *Nano Letters* **2014**, *14*, 847–852.

(39) Fink, C. G.; Dokras, V. M. Electrodeposition and Electrowinning of Germanium. *Journal of the Electrochemical Society* **1949**, *95*, 80–97.

(40) Hao, J.; Liu, X. X.; Li, N.; Liu, X. S.; Ma, X. X.; Zhang, Y.; Li, Y.; Zhao, J. P. Ionic liquid electrodeposition of 3D germanium-acetylene black-Ni foam nanocomposite electrodes for lithium-ion batteries. *Rsc Advances* **2014**, *4*, 60371–60375.

(41) Hao, J.; Li, N.; Ma, X. X.; Liu, X. X.; Liu, X. S.; Li, Y.; Xu, H. B.; Zhao, J. P. Ionic liquid electrodeposition of germanium/carbon nanotube composite anode material for lithium ion batteries. *Materials Letters* **2015**, *144*, 50–53.

(42) Hao, J.; Zhao, J. P.; Zhang, Y. W.; An, X. K.; Liu, X.; Li, Y.; Endres, F. Electrodeposition of Three Dimensionally Ordered Macroporous Germanium from Two Different Ionic Liquids. *Journal of Nanoscience and Nanotechnology* **2016**, *16*, 777–782.

(43) Ke, J.; Bartlett, P. N.; Cook, D.; Easun, T. L.; George, M. W.; Levason, W.; Reid, G.; Smith, D.; Su, W. T.; Zhang, W. J. Electrodeposition of germanium from supercritical fluids. *Physical Chemistry Chemical Physics* **2012**, *14*, 1517–1528.

(44) Lahiri, A.; El Abedin, S. Z.; Endres, F. UV-Assisted Electrodeposition of Germanium from an Air- and Water-Stable Ionic Liquid. *Journal of Physical Chemistry C* **2012**, *116*, 17739–17745.

(45) Lahiri, A.; Olschewski, M.; Carstens, T.; Abedin, S. Z.; Endres, F. Electrodeposition of Crystalline Gallium-Doped Germanium and SixGe1-x from an Ionic Liquid at Room Temperature. *Chemelectrochem* **2015**, *2*, 571–577.

(46) Martineau, F.; Namur, K.; Mallet, J.; Delavoie, F.; Endres, F.; Troyon, M.; Molinari, M. Electrodeposition at room temperature of amorphous silicon and germanium nanowires in ionic liquid. *Semiconductor Nanostructures Towards Electronic and Optoelectronic Device Applications Ii (Symposium K, E-Mrs 2009 Spring Meeting)* **2009**, *6*.

(47) Szekely, G. Electrodeposition of Germanium. *Journal of the Electrochemical Society* **1951**, *98*, 318–324.

(48) Wu, M. X.; Brooks, N. R.; Schaltin, S.; Binnemans, K.; Fransaer, J. Electrodeposition of germanium from the ionic liquid 1-butyl-1-methylpyrrolidinium dicyanamide. *Physical Chemistry Chemical Physics* **2013**, *15*, 4955–4964.

(49) Wu, M. X.; Vanhoutte, G.; Brooks, N. R.; Binnemans, K.; Fransaer, J. Electrodeposition of germanium at elevated temperatures and pressures from ionic liquids. *Physical Chemistry Chemical Physics* **2015**, *17*, 12080–12089.

(50) Kowalczyk, P.; Kozlowski, W.; Klusek, Z.; Olejniczak, W.; Datta, P. K. STM studies of the reconstructed Au(111) thin-film at elevated temperatures. *Applied Surface Science* **2007**, *253*, 4715–4720.

Chapter 4

Surface Enhanced Raman Spectroscopic Study of Germanene Layers Formed by Electrodeposition [1]

[1] Bui, N.; Jung, J.; Kim, Y.-G.; Soriaga, M. P.; Reber, T. J.; Stickney, J. To be submitted to ACS Nano.

4.1 Abstract

The electrochemical formation of germanene on Au(111) has been reproducibly verified in several studies. EC-STM images of the germanene layers displayed multiple small domains (2-3 nm) with clear evidence of the honeycomb structure. The electron-phonon coupling in germanene has shown to improve the quality of the deposit. In the present study, *in situ* surface enhanced Raman spectroscopy was used to probe the vibrational modes of germanene during the electrodeposition. After an exposure to a 780 nm laser (8mW, 3.1 µm spot size), prominent peaks at 200 cm^{-1} and 295 cm^{-1} were observed, suggesting a reconstruction of the initial germanene layers into a more ordered sheet. The first layer of germanene (200 cm^{-1}) is thought to adopt a different vibrational mode from the second layer (295 cm^{-1}), due to its interaction with the Au substrate. A Raman peak at 630 cm^{-1} is thought to be an overtone of 200 cm^{-1} peak. Another tiny peak at 165 cm^{-1} corresponds to the out-of plane vibration of Ge atoms in the second layer. The effect of H_2 evolution at more negative potentials seemed to disrupt the surface integrity, causing a physical rise of the deposit off the substrate. Without the second layer on top, the first Ge layer can be irreversibly removed from the surface through hydrogen evolution. Both EC-STM images and Raman spectra indicate that Ge can remain on the surface after its oxidation, making the coulometric data insufficient for the quantification of Ge deposits. The pH study suggests that the system can be better detected in a more basic solution. Photochemistry is thought to also be occurring as photoelectrons generated on the germanene deposit can induce the formation of a H_2 bubble at the annealed spot, from which its size increases as solution gets more acidic. When Te is deposited on a Ge-covered Au substrate, the 200 cm^{-1} peak corresponding to the first Ge layer disappeared, indicating that Te atoms have sunk down, displacing the Ge layer that bonds to Au. Oxidation of the Ge layers showed that the 200 cm^{-1} eventually turned into a broad peak at 295 cm^{-1}.

4.2 Introduction

Germanene is a 2D allotrope of Ge that exhibits a hexagonal arrangement similar to graphene.[1–3] Despite a thriving number of reports on its structures and formation,[4–10] knowledge of germanene's growth is still limited and much about its behavior remains to be explored. The elements from the same group IV (C, Si, Ge, and Sn) are expected to have comparable properties. Similar to graphene and silicene, germanene is thought to be a topological insulator by having both bulk gapped states and gapless states at the edges.[11–18] The electrons in germanene are also thought to behave as if they are massless,[19] leading to a few order of magnitude increment in their mobility.[20] Unlike graphene, the two-dimentionality in silicene and germanene does not require all the atoms in the honeycomb structure to form a perfectly flat sheet.[21] A mixture of sp^2 and sp^3 characters is widely expected for silicene and germanene as their stable structures would likely adopt a slight buckling in height.[22] The buckled structure makes germanene innately less rigid than graphene with a completely flat arrangement. One challenge with germanene synthesis is that there is no known form of graphite-like germanene. The covalent bonds in bulk Ge are also deemed too strong to be broken, thus limiting its synthesis to mostly a bottom-up growth method, except for one group that has reported the deintercalation of $CaGe_2$ to form germanane (GeH_x).[23] The diversity of its properties continues to inspire promising research in both theoretical and experimental avenues.[24–61]

The fabrication of germanene has mostly been studied in the UHV system where germanene is slowly evaporated by molecular beam epitaxy (MBE) in a clean and inert environment.[37,62–68] However, the complexity of the set up tends to limit its accessibility and scalability. Electrodeposition has been considered a low-cost method that can produce of high-quality materials. One example is the Damascene process of Cu used in the creation of microstructures for electronic applications. The electrodeposition of Ge has been performed in many different media.[69–81] From aqueous

solution, Ge deposition revealed the formation of small domains with honeycomb structures indicative of germanene growth. Its deposition has been done on many different substrates,[37,62–66] including Au.[67,68] Previous reports have shown that EC-STM can be a powerful tool to access the growth mechanism at the interfaces between Au and Ge.[82–86]

The ability to image the surface with EC-STM, however, often comes with a high cost of time, experience, and often luck. Raman spectroscopy, on the other hand, can be a much more versatile tool if the meaning of each signal can be deconvoluted by pairing with known surface processes from EC-STM. With the enhancement effect from both the localized plasmon and polariton resonance, surface enhanced Raman spectroscopy (SERS) can be very valuable for an instant detection of vibrational modes of very minute features.[87–92] The SERS substrates are intentionally made with irregular features to create some large fields that allow photon to interact more strongly and for a prolong period of time with the surface, resulting in the enhancement of the signal. For a system that is only one nm thick, such as Ge(aq), an exponential increase in the photon output is necessary. The present study aims to provide a more detailed picture of how germanene are formed on the surface, step by step, probed by both EC-STM and *in situ* SERS. The spectroscopic technique is simple, fast, giving room for more complex experimental designs by coupling with a modified flow cell system.

The effect of laser crystallization on germanene deposit has been previously documented. When germanene starts to form a second layer, a Raman peak at 295 cm-1 corresponding to a free-standing sheet was observed. In the presence of Au, the electrons in the germanene first layer are expected to interact differently. The annealing effect from the laser is not simply the result of substrate heating, as the more energetic laser at 532 nm with equivalent power density could not produce the crystallization effect as the 780 nm laser. The report also indicated that the germanene peak at 295

cm^{-1} can easily be detected with 532 nm laser, if the area has been formerly exposed and annealed by the 780 nm laser.

To improve the quality of the germanene deposit requires a better understanding of all the factors that directly influence its formation. Several questions remaining from the recent study include a better understanding of what happen to the first layer of germanene bonding to the Au substrate and what kind of reaction is occurring during the annealing process. A new vibrational mode at 200 cm^{-1} was thought to correspond to the first layer. The effect of pH from the present study suggests that photochemistry is also occurring and that induces the formation of hydrogen bubble at the annealed spot.

4.3 Experimental

4.3.1 *In situ* Surface-Enhanced Raman Spectroscopy (SERS)

Raman spectra were collected using a DXR Raman Microscope from Thermo Scientific, with an 8 mW 780 nm laser as the excitation source. The spot size was estimated to be around 3.1 µm in diameter. A home-built Raman electrochemical flow cell was used to perform *in situ* SERS. The quartz cell window was positioned under a 10x objective, through which the laser was focused onto the deposit surface. A cell was designed so that solutions could be flowed through the cell while taking spectra. Some experiments require solutions to be switched from blank to GeO_2 or TeO_2 under potential control to perform some analytical studies. A computer was used to program solutions flow as well as potential. All solutions were degassed prior to use, to minimize oxygen. The Au SERS substrates were made in house using 600 nm polystyrene spheres as templates.[93,94] Before each Raman experiment, Au slide was cleaned with concentrated nitric acid for 30 s follows by multiple rinses with ultrapure H_2O. Afterward, the electrode was cleaned electrochemically with 0.1 M sulfuric acid using -0.2 V and 1.4 V as scanning windows. The instrumental set up

and an example of a SERS substrate are shown in Figure 4.1. The schematics of how *in situ* SERS is able to detect signal from just a few monolayers thick germanene are illustrated in Figure 4.2.

4.3.2 Electrochemical Scanning Tunneling Microscopy (EC-STM)

The set up for EC-STM was as described from previous report. Nanoscope III (Digital Instruments, Santa Barbara, CA) was used to take spectra under constant current mode. The imaging surface was an Au(111) facet of the Au bead single crystal. Before each experiment, the electrochemical cell was cleaned with Nochromix and rinsed with ultrapure H_2O. The Au bead was melted using a finely controlled H_2/O_2 flame and annealed under H_2 atmosphere. The STM tip was made from 0.25 mm diameter Tungsten wire etched in 0.6 M KOH at 16 V AC. To image in solution, the tip must be coated with nail polish to limit Faradaic current to only at the apex. The cell and the scanning head were encapsulated in a N_2 purged environment.

4.3.3 Chemicals

Ge solutions for EC-STM studies were made from 99.999% GeO_2 from Alfa Aesar and 99.99% $KClO_4$ trace metal basis from Aldrich. All solutions were purged with nitrogen before the electrochemical cell was assembled. Ge solutions for Raman studies were made from 99.98% GeO_2 from Alfa Aesar, and 70% concentrated $HClO_4$ acid from GFS Chemicals. Ultrapure 18 MΩ H_2O was used to clean all glassware and prepare solutions. All electrochemical cells were set up with a three-electrode configuration using Ag/AgCl (3M Cl^-) as the reference. Ge solutions contain 1mM GeO_2 and 50-100 mM ClO_4^- as electrolyte. All experiments were done at pH 9.0, except those in Figures 10 where the study of pH dependent was specifically conducted. pH 9.0 solution used 50 mM $Na_2B_4O_7$ (Baker Analyzed A.C.S. Reagent) as buffer and pH 4.6

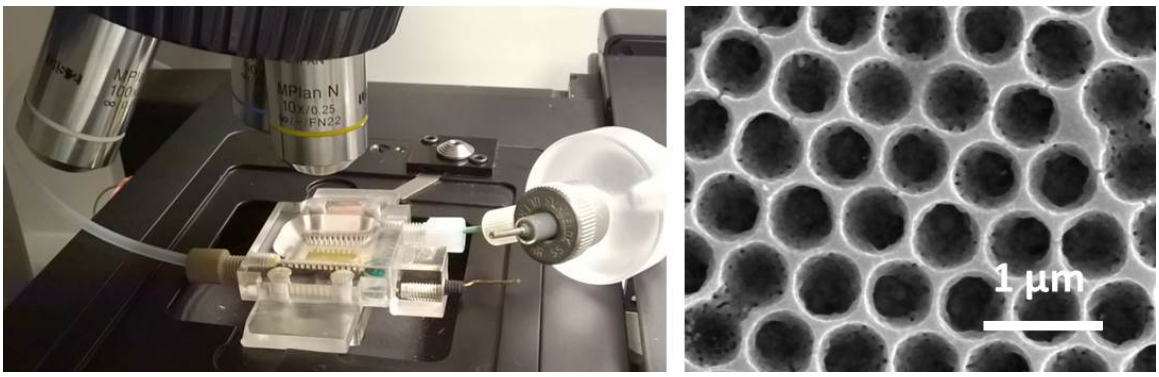

Figure 4.1: Instrumental set up for the *in situ* Surface Enhanced Raman Spectroscopy measurement. 8 mW 780 nm laser was focus onto a 3.1 µm spot size through a 10x objective. A modified flow cell system was designed to enable solution exchanged while having potential control. SEM image shows the surface of an Au SERS substrate containing multiple 0.6 µm diameter hollow spheres.

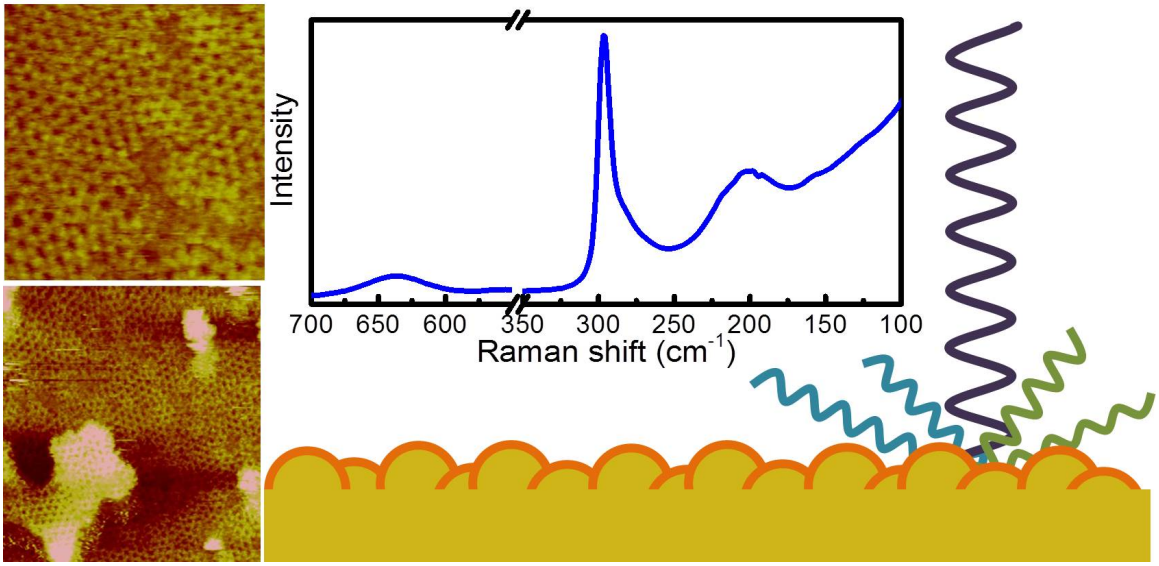

Figure 4.2: Schematic of an *in situ* SERS process. Raman signal was obtained from just a few layers of germanene.

solution used 50 mM sodium acetate (Baker Analyzed A.C.S. Reagent). Te solution contains 0.2 mM TeO_2 (99.995%, Aldrich), 50 mM $Na_2B_4O_7$, and 0.1 M ClO_4^-.

4.4 Results and Discussion

Figure 4.3 shows the Raman spectra as a function of the applied potential, from -0.3 V to -0.9 V. EC-STM images from previous report suggested that Ge deposition begins at around -0.7 V. As expected, there was no Raman peak corresponds to Ge from -0.3 V to -0.6 V, since only Au reconstruction was occurring between these potentials.

There were two peaks of Ge, 200 cm^{-1} and 630 cm^{-1}, appearing at -0.7 V and continuing to grow as potential was bias to -0.9 V. Since the intensities of these two peaks were proportional to each other, the 630 cm^{-1} was thought to be an overtone of 200 cm^{-1}. Results from EC-STM suggested that germanene precursors were growing along the face-center-cubic (fcc) region of the herringbone (HB) reconstruction from -0.7 to -0.85 V (Figures 4.3); and at -0.9 V, a complete sheet of germanene was observed where the Au HB relaxed and the lines were displaced by Ge atoms, forming new Au islands on the surface that are also covered with germanene rings. The first layer of germanene bonding to the Au substrate appeared to have a different vibrational mode from the one expected at around 300 cm^{-1} from the theoretical calculation. It is proposed here that the interaction between the Au and the first germanene layer has induced some strains onto its vibrational mode, thus red-shifting the energy from 300 cm^{-1} to a lower wavenumber (200 cm^{-1}). Previous report has shown that the germanene peak at 297 cm^{-1} will yet appear until the second layer was formed at -1.0 V. Because 297 cm^{-1} was calculated for a free-standing sheet of germanene, when the second layer was more liberated from the Au substrate than first layer, it can adopt a higher vibrational mode as expected for germanene.

Figure 4.4a shows an experiment where Ge was first deposit at -0.9 V, after which solution was exchanged into blank at the same bias. The peaks for Ge at 200 cm^{-1} and

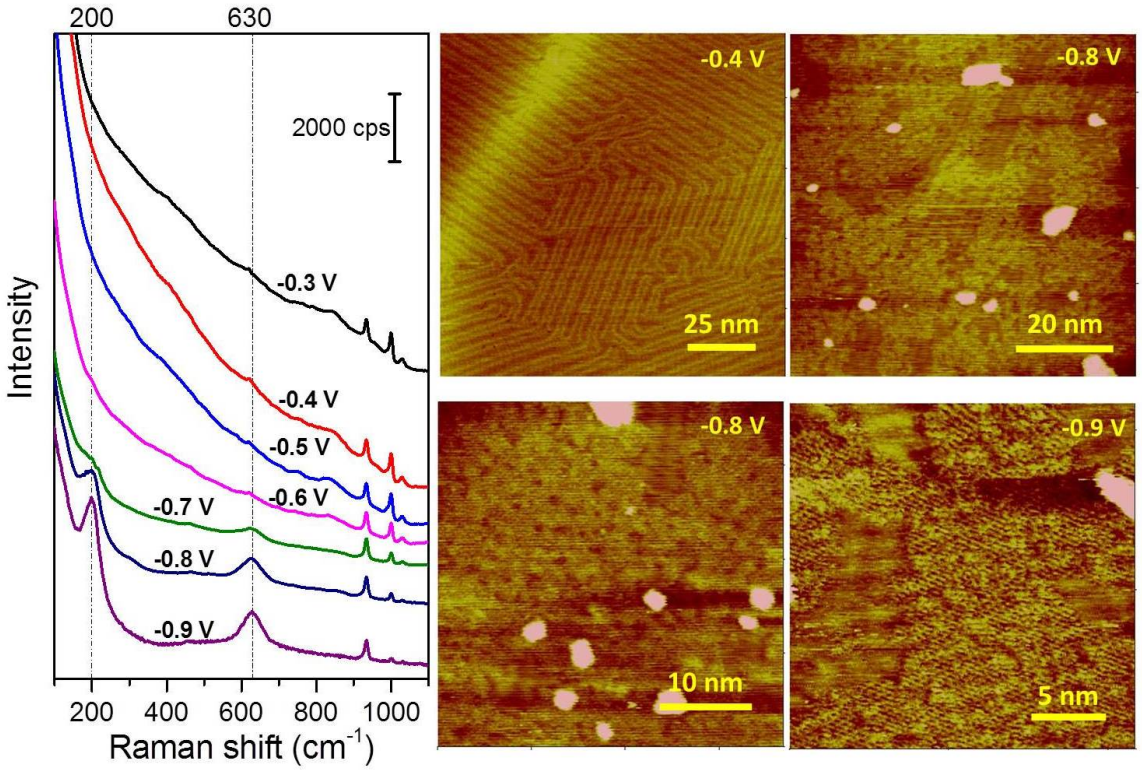

Figure 4.3: EC-STM images and *in situ* SERS spectra of the surface transition from the precursor stage to the first germanene layer. Ge deposition begins at -0.7 V where they nucleate in the fcc region of substrate. As potential gets close to -0.9 V, these domains expand and eventually merge together, expelling the Au HB from the surface, forming new islands. The Raman peak at 200 cm^{-1} corresponds to the first layer that strongly interacts with Au substrate. The peak at 630 cm^{-1} is its overtone.

630 cm^{-1} also appeared in blank, despite continuous rinsing, suggesting that the first germanene layer is stable and chemically bonding to the Au substrate. As expected from previous report, the annealing effect from 780 nm laser was also observed (Figure 4.4b). The Ge peaks were visible after 10 s of exposure to 8 mW 780 nm laser. The intensity seemed to saturate at an exposure dose of 100 s. To avoid complication from varying exposure dose, all of the Raman spectra in the present report were done in 100 s exposure to 8 mW 780 nm laser, except those in Figure 4.4 where variation of doses was intentionally studied.

Figure 4.5a shows a full Raman spectrum of germanene first and second layers. The 200 cm^{-1} peak corresponds to the first layer of germanene that is strongly interacting with Au substrate. The 630 cm^{-1} peak is attributed to its overtone. The second layer starts to show the vibrational mode of germanene free-standing sheet at 295 cm^{-1}. There is another tiny peak at 156 cm^{-1} that could be the out-of plane vibration of the Ge atoms. The intensity of this peak is expected to be much lower than the G-like peak at 295 cm^{-1}, and its presence was characteristic of the buckling arrangement in germanene. Formation of the 200 cm^{-1} peak requires an annealing step of the first germanene layer prior to depositing the second layer. Figure 4.5b shows an experiment where the electrode was stepped to -1.1 V without a pre-annealing step at -0.9 V where the surface was covered with only the first layer. It seems that once the second layer has formed, it prevents the annealing process to occur on the first layer, and thus the peak at 200 cm^{-1} was not observed. The potential was then stepped back to -0.9 V to reduce the effect of hydrogen evolution, without causing any oxidation to the electrode surface. However, there was still no indication of the peak 200 cm^{-1}.

Figures 4.6a-c describe the effect of hydrogen evolution on the Ge layers and their Raman signals. EC-STM images have previously documented the chaotic rearrangement of the Ge layers when the potential was bias more negatively than -1.0 V. A surface disruption was thought to occur with pin holes forming at defects and domain

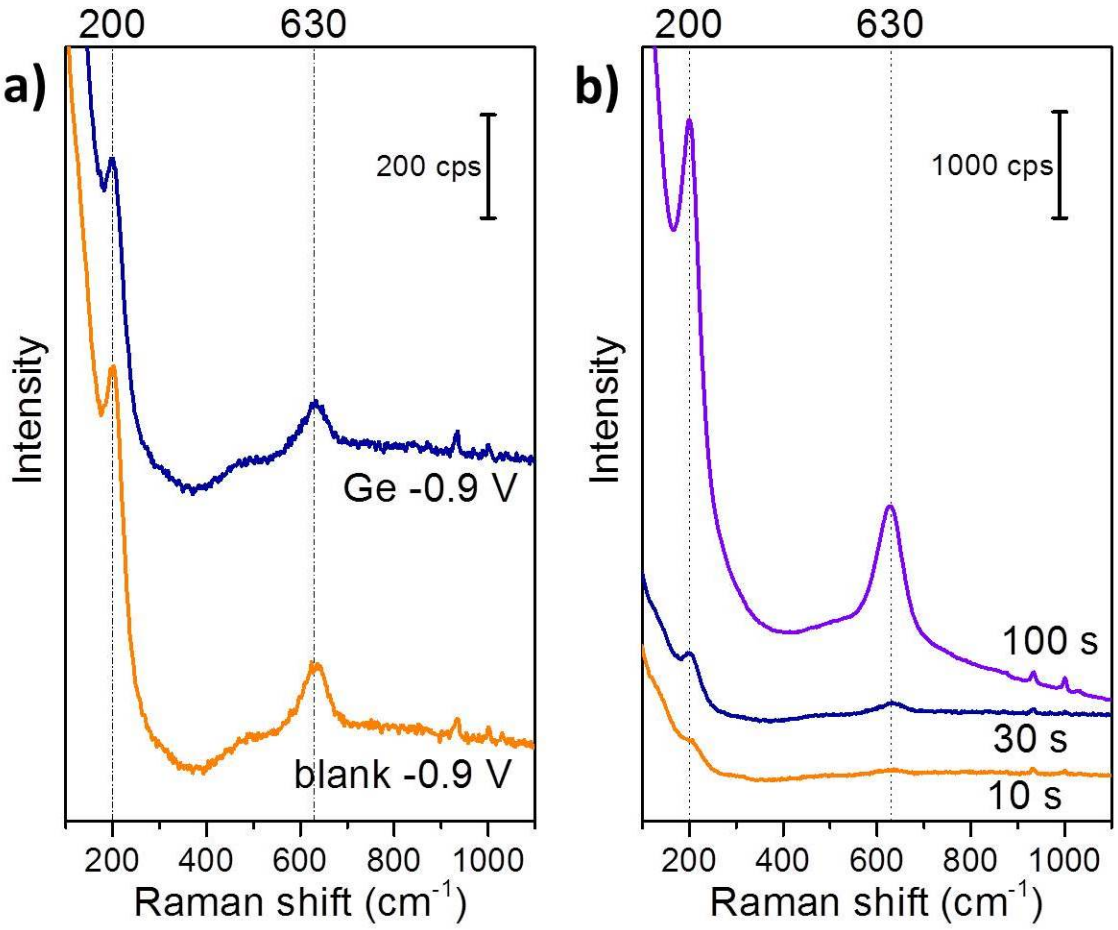

Figure 4.4: (a) Blue: Ge was deposited at -0.9 V. Yellow: solution is changed to blank, potential is held at -0.9 V. Peak 200 cm^{-1} corresponds to Ge species that are chemically bonding to the surface. (b) Laser crystallization effect after 10 s, 30 s, and 100 s exposures to 8 mW 780 nm laser. Signal intensity was saturated at 100 s exposure.

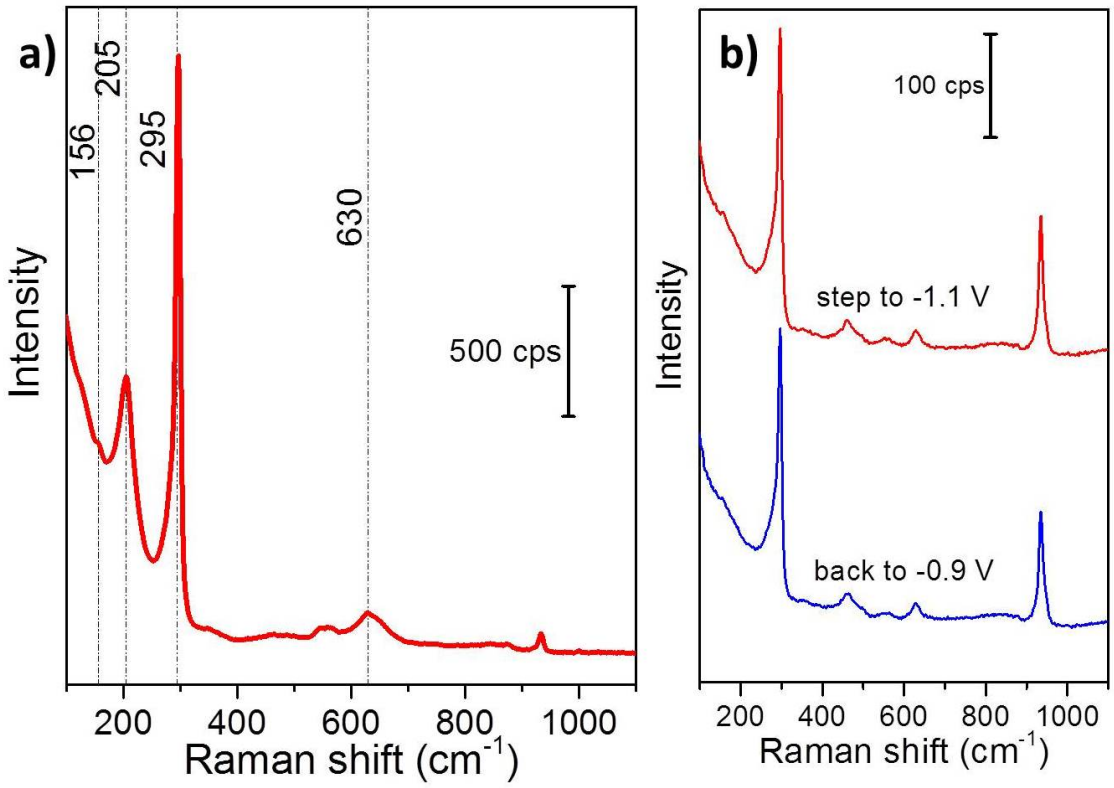

Figure 4.5: (a) A complete Raman spectrum of the first and second layer germanene. 630 cm^{-1} is the overtone of 200 cm^{-1}, which corresponds to the first layer germanene strongly interacting with Au. 295 cm^{-1} is the second layer germanene that is more liberated from the substrate. 156 cm^{-1} is the out-of plane vibration of germanene atoms in the second layer. (b) To form the 200 cm^{-1} peak, the first layer needs to be annealed before the second layer. Red: In Ge solution, potential was stepped directly from the open circuit potential (OCP) to -1.1 V without pre-annealing/exposing the surface at -0.9 V to the 780 nm laser. Blue: Potential is stepped down to -0.9 V from -1.1 V to reduce the hydrogen evolution. The peak at 200 cm^{-1} was not observed in either case, suggesting that forming of the second layer too quickly has prevented the annealing process to occur on the first layer.

edges. Figure 4.6a shows the sequential Raman spectra of the Ge layers from -0.9 V, to -1.0 V, then to -1.1 V and back to -0.9 V. The spectrum at -1.1 V displays a loss of 200 cm^{-1} peak and a decrease in 295 cm^{-1} peak's intensity. This could be explained through the effect of hydrogen evolution. As hydrogen bubbles evolve from the surface, they lift off the Ge layers so they are no longer in contact with Au, which would make the 200 cm^{-1} disappears. The increase in distance from the surface could also reduce the plasmonic resonance effect from the substrate, abating the peak intensity at 295 cm^{-1}. When potential was stepped back to -0.9 V, the effect of hydrogen was mitigated, thus allowing the 200 cm^{-1} to redevelop and the 295 cm^{-1} peak's intensity to rise.

Figure 4.6b illustrated another experiment where hydrogen evolution had irreversibly changed the Raman signal of the first germanene layer at 200 cm^{-1}. The surface was first deposited with one layer of Ge at -0.9 V, after which the solution was exchanged to blank and the potential was stepped consecutively from -0.9 V to -1.0 V, then to -1.1 V, and back to -0.9 V. When there was only one Ge layer on the surface, the hydrogen evolution occurring at -1.0 V was enough to remove the 200 cm^{-1} peak. Without the second layer on top to suppress the removal of the deposit from the surface, the signal at 200 cm^{-1} was not restored even after the potential was stepped back to -0.9 V to avoid hydrogen evolution. Figure 4.6c shows a similar result to Figure 4.6a, but instead of executing in Ge solution as in 4.6a, the experiment was carried out in blank. After the deposition of the first layer and a partial second layer at -0.9 V and -1.0 V in Ge solution, to form both peaks at 200 cm^{-1} and 295 cm^{-1}, the cell was rinsed with blank and the potential was changed from -1.0 V to -1.1 V, and follows by -0.9 V. Similar to Figure 4.6a and b, the peak at 200 cm^{-1} disappeared at more negative potential. However in the presence of the second layer, it became harder to remove the first layer completely off the surface. When the potential was stepped back to -0.9 V, the first layer peak at 200 cm^{-1} reappeared when there is a

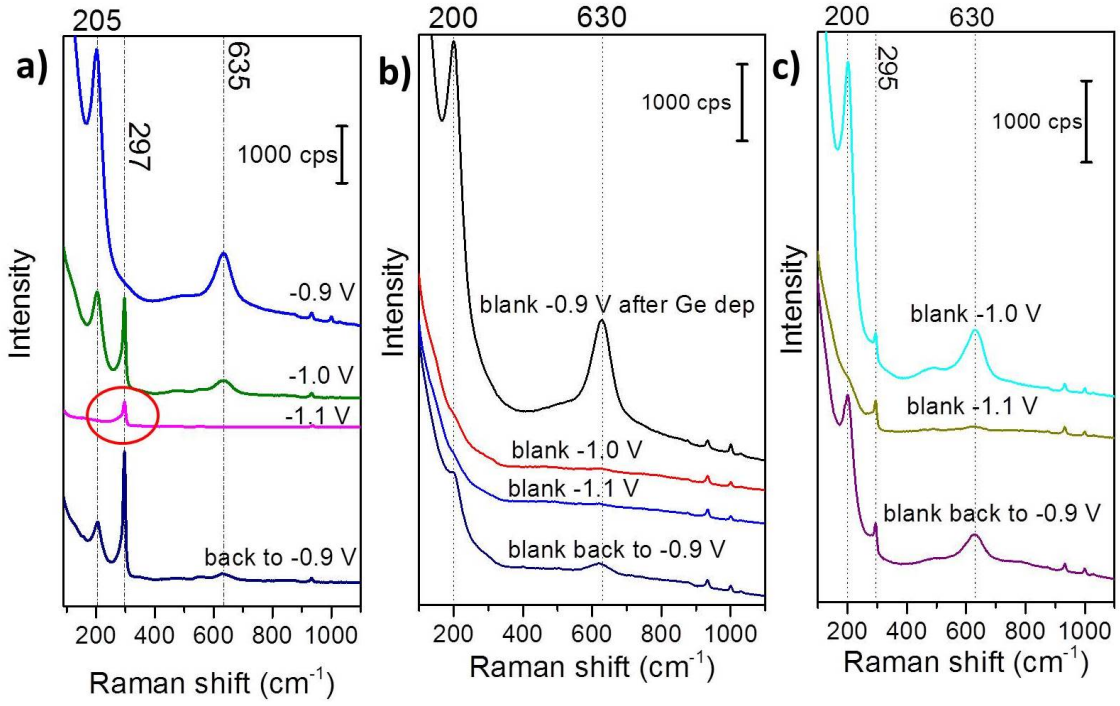

Figure 4.6: (a) Raman spectra of one germanene layer at -0.9 V, two layers at -1.0 V, hydrogen evolution at -1.1 V, and alleviation of hydrogen at -0.9 V. Formation of hydrogen at negative potential caused the 200 cm^{-1} peak to disappear while also decreased the intensity of the 295 cm^{-1} peak. (b) Without the second layer on top, the first layer can be irreversibly removed from the surface. Ge is first deposited at -0.9 V. Solution is exchanged to blank and E was changed consecutively to -1.0 V, -1.1 V and back to -0.9 V. (c) With the second layer on top, the first layer can be retained on the surface and the 200 cm-1 peak regrew when E was stepped positively from -1.1 V to -0.9 V.

second layer on top (4.6a and c), as opposed to being irreversibly delaminated from the surface (4.6b).

Oxidation of the 200 cm^{-1} and the 295 cm^{-1} as a function of potential was monitored through changes in the Raman signal (Figures 4.7a and b). In Figure 4.7a, only one layer of Ge was deposited at -0.9 V to form the 200 cm^{-1} peak. In Figure 4.7b, after forming the first layer at -0.9 V, potential was held at -1.0 V to form the second layer (295 cm^{-1} peak). In both cases, following the Ge layers' formation, potential was then stepped positively sequentially every 0.1 V apart to oxidize off the surface. Interestingly, the 200 cm^{-1} gradually disappeared and turned into a broad peak at around 295 cm^{-1}. In Figure 4.7a, there was no Raman peak initially at 295 cm^{-1} since only the first layer was deposited. However, starting at -0.5 V, there was an emergence of the peak 295 cm^{-1} after the 200 cm^{-1} peak disappeared. This suggests that once the layer is no longer bonding to the surface, it could take on the vibrational mode of a free-standing sheet at 295 cm^{-1}. The same behavior was observed in Figure 4.7b where the peak at 295 cm^{-1} got broaden from merging with the 200 cm^{-1} peak.

The Ge species seemed to hang around the surface way passed its oxidation point. According to the CVs of Ge at pH 9.0, the last Ge oxidation peak occurs at -0.18 V. By the time the potential reaches 1.0 V, all Ge must have been completely oxidized from the surface. However, there is still a Raman signal at 295 cm^{-1} at 1.0 V (Figure 4.7a), suggesting that Ge species are hovering over the Au. Only when the substrate was oxidized to 0.5 V can Ge be completely removed from the surface.

Figures 4.8a-d display EC-STM images of the oxidation of the second Ge layer. Conditions to form the second layer were similar to what were described previously, except without the annealing step from the 780 nm laser. Potential was first held at -0.9 V to form the first layer, and then stepped to -1.0 V to form the second layer. Once the second layer was formed, the potential was stepped positively every 0.1 V apart to observe the oxidation process. Sequence of STM images were recorded

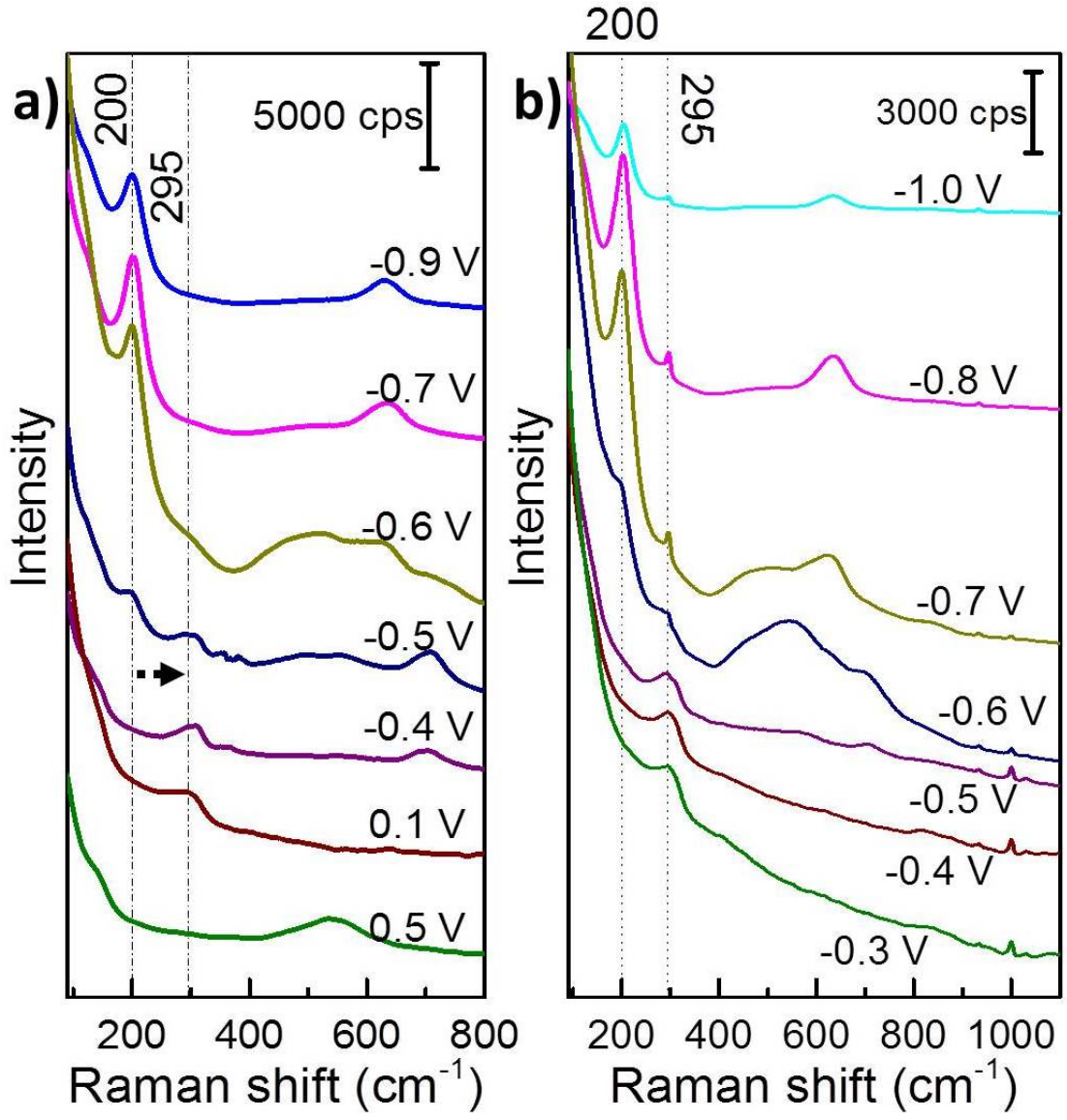

Figure 4.7: (a) Raman spectra illustrating the oxidation process of the first germanene layer. From top to bottom, the Ge layer is oxidized slowly every 0.1 V apart. At -0.5 V, the 200 cm^{-1} peak turned into a broad peak at 295 cm^{-1}. Even after oxidation, Ge stayed around the surface (0.1 V). Only when the Au is completely oxidized at 0.5 V can Ge be removed (b) Raman spectra illustrating the oxidation process of two layers of germanene.

successively at -0.7, -0.6, -0.3 and -0.1 V, with a couple minutes between. Starting at -0.7 V, the sheet broke down into smaller domains with random shapes of around 10 nm in each width and length dimension. The line of breakage probably had followed the site of defects inevitably resulted from the former nucleation and growth process. As the potential got further positive, these Ge domains rearranged gradually from their random shapes to some round islands, and floated on top of the substrate. Such weak bonding between these domains and the substrate further suggested that only Van der waals interaction were holding them together. Similar to the Raman results discussed in Figure 4.7a, these Ge islands would remain on the surface for a long time unless the Au substrate was oxidized to 0.5 V and reduced back to -0.3 V.

In Figures 4.9a-b, the effect of pH on the Raman signals was also investigated, as different surface transitions have been documented previously between pH 4.6 and pH 9.0. Figure 4.9a compares the intensity of the 200 cm^{-1} peak formed in similar condition at different pH. At pH 11.1 and 9.0, the first Ge layer was formed at -0.9 V, while at pH 4.6 it was at -0.7 V. Figure 4.9b examines the intensity of the 295 cm^{-1} peak formed at -1.0 V in pH 9.0 and 11.0 and at -0.8 V in pH 4.7. It seems that the system works better at more basic pH, as the Raman intensity is consistently higher as the solution becomes more basic. Future studies are needed to determine whether this phenomenon was due to hydrogen evolution that could vary the SERS effect on detecting the signal at different pH, or simply better quality germanene was forming at pH 11.1.

Interestingly, at the exact spot where the laser was focused on, a micron size bubble would reproducibly form at approximately the same potential to form the second layer. The size of the bubble also gets progressively larger as the solution becomes more acidic. This correlation suggested that the bubble might be filled with H_2, and photochemistry is thought to be occurring on the annealed spot. When infrared photon with the correct energy (780 nm) was applied, it created electron-hole pairs in

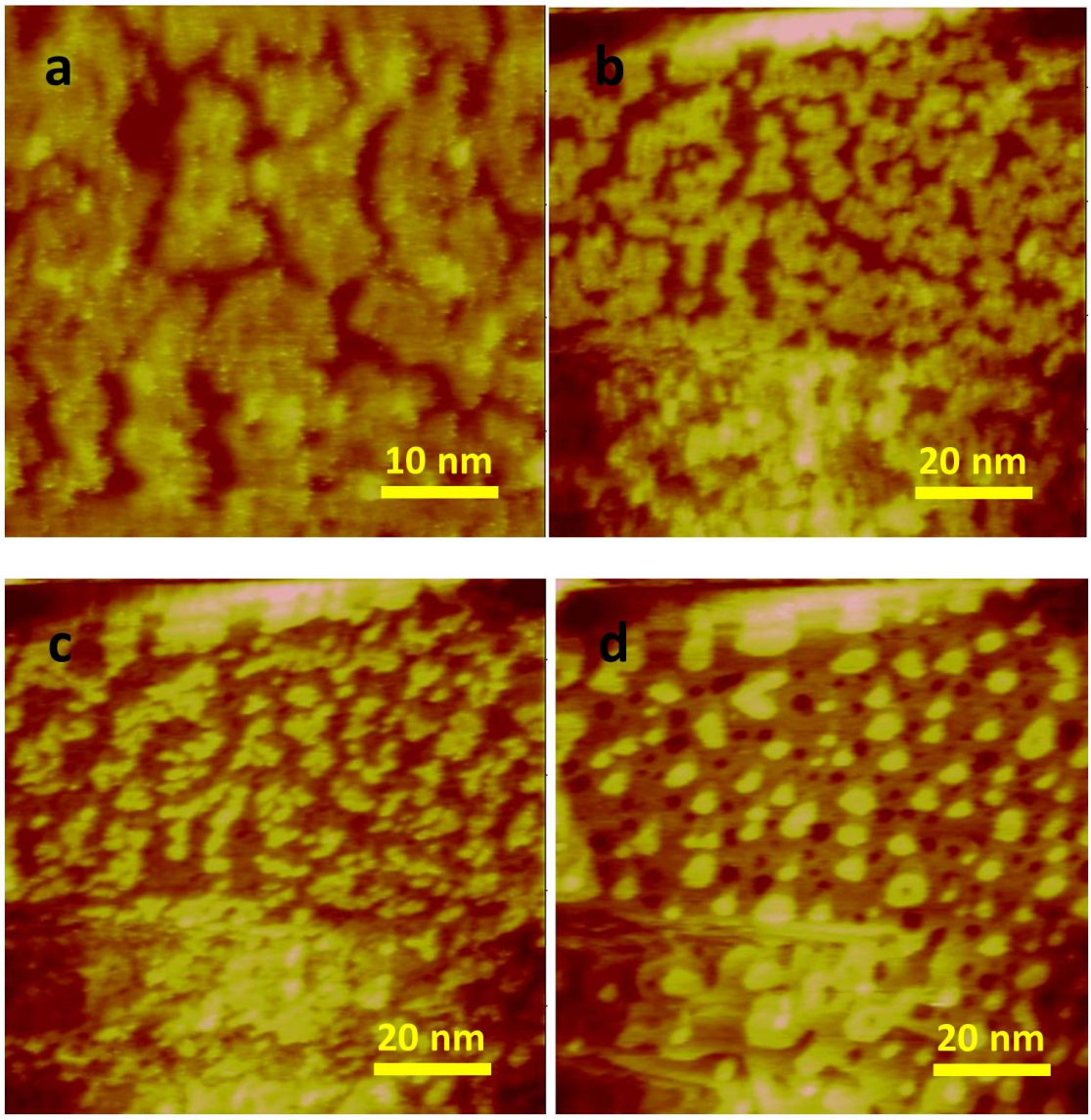

Figure 4.8: Oxidation of the Ge second layer formed at -1.0 V. The layer broke down at defects and oxidized gradually at the edges, which led to formation of round features floating on top of the surface. The resulting pitted surface suggested some alloying from the deposition. (a) E = -0.7 V, t = 0 min. (b) E = -0.6 V, t = 7 min. (c) E = -0.3 V, t = 10 min. (d) E = -0.1 V, t = 12 min.

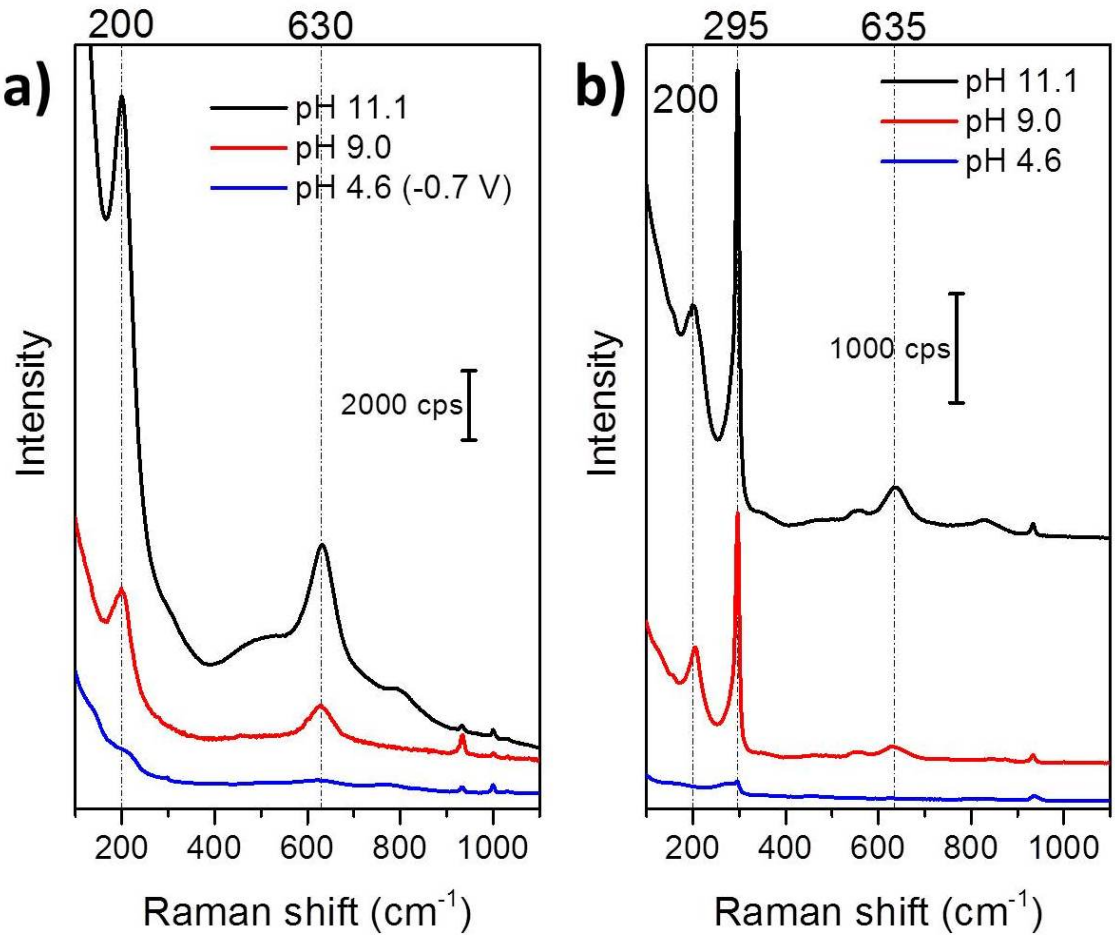

Figure 4.9: pH dependent study on Raman intensity of (a) peak 200 cm^{-1} and 630 cm^{-1} (b) peak 295 cm^{-1}.

the germanene deposit. These photon-induced electrons can shift the Fermi level up, and when the energy level is above that needed to split H_2O, H_2 bubbles are created. No bubble was observed when the same photon energy and density was incident on the Au substrate. Addition of two atomic layers of germanene should not have changed the thermal conductivity of the surface significantly. Combination of these factors and the passiveness of the 532 nm laser confirm that photochemistry is contributing to the formation of ordered germanene sheet.

Reinvestigation into the bait and switch E-ALD cycle using *in situ* Raman gives forth to a better understanding of what processes are occurring on the surface of the electrode. Figure 4.10b shows how the oxidative stripping of Ge changes as Te depositing on the surface. In the red curve, Ge was first deposited on the Au substrate at -1.3 V for 60 s. The oxidative stripping of this process resulted in a bulk Ge peak at -0.3 V and a Ge UPD at -1.0 V. In the green curve, the deposition of Ge was repeated exactly as the red curve, but follows by a solution exchange to Te where it was deposited at -0.9 V for 10 s. There was no extra Ge deposited in the green curve from the red curve. The Ge UPD charge seemed to have merged with the Ge bulk charge at -0.3 V, indicating that Te has displaced the first layer of Ge bonding to the Au substrate. The schematic in Figure 4.10c is to illustrate this rearrangement between Te and Ge, when Te was depositing on a few monolayers of Ge on Au. Figure 4.10a shows a step by step of how the surface was changing with Te depositing and stripped from Ge layers. After the formation of two Ge layers, as indicated by both peaks at 200 cm^{-1} and 295 cm^{-1}, Te was deposited at -0.9 V, where a Te peak at 122 cm^{-1} was observed. The Ge peak at 200 cm^{-1} disappears, suggesting that Te has gone underneath the Ge layers and bonded with Au. Interestingly, the intensity of the peak at 295 cm^{-1} also decreases as compared to having just two layers of Ge on the surface. There could be a few possible interpretations for this phenomenon. One is that Te has disrupted the layers of Ge, making them more disordered, and thus

reducing the peak's intensity. Another possibility is that while Te is bonding to the Au substrate, Ge layers were no longer in direct contact with Au, thus weakened the plasmonic effect, causing a decrease in intensity. Given that there was no observable shift in the peak position towards amorphous Ge (270 cm^{-1}), the later interpretation is deemed more likely. When the majority of Te was stripped from the surface at -1.3 V, the 295 cm^{-1} peak regrew in intensity, but the 200 cm^{-1} peak was permanently absent afterward. Similar to the result from Figure 4.10b where there was always a Te oxidation peak at around 0.15 V, Te was thought to have irreversibly bonded to Au, preventing a direct contact between Ge and the substrate.

4.5 Conclusion

Formation of the first and second layer germanene on Au was investigated using a combination of *in situ* SERS and EC-STM. Exposure to a 780 nm laser (8 mW, 3.1 µm crystallizes the deposit to a more ordered sheet. Vibrational spectrum of the first germanene layer exhibits a Raman peak at 200 cm^{-1} and an overtone at 630 cm^{-1}. The second layer adopts a G-like peak at 295 cm^{-1} and another vibrational mode at 165 cm^{-1} that was attributed to the buckling arrangement. Hydrogen evolution was undesirable as it can cause irreversible surface rupture, especially to the first layer. Ge species stayed on the surface even after its oxidation at 0.1 V. The peak at 200 cm^{-1} eventually turns into a broad peak at 295 cm^{-1} after Ge is oxidized. EC-STM images also displayed some floating islands of Ge hovering over the Au substrate. Basic solution resulted in higher Raman signals and smaller hydrogen bubble at the annealed spot, suggesting that photochemistry on germanene is causing the reduction of H_2O. Au-Te bond seems to be more favorable than Au-Ge bond, as Te depositing on a few layers of Ge can go underneath the deposit and bond with the Au substrate.

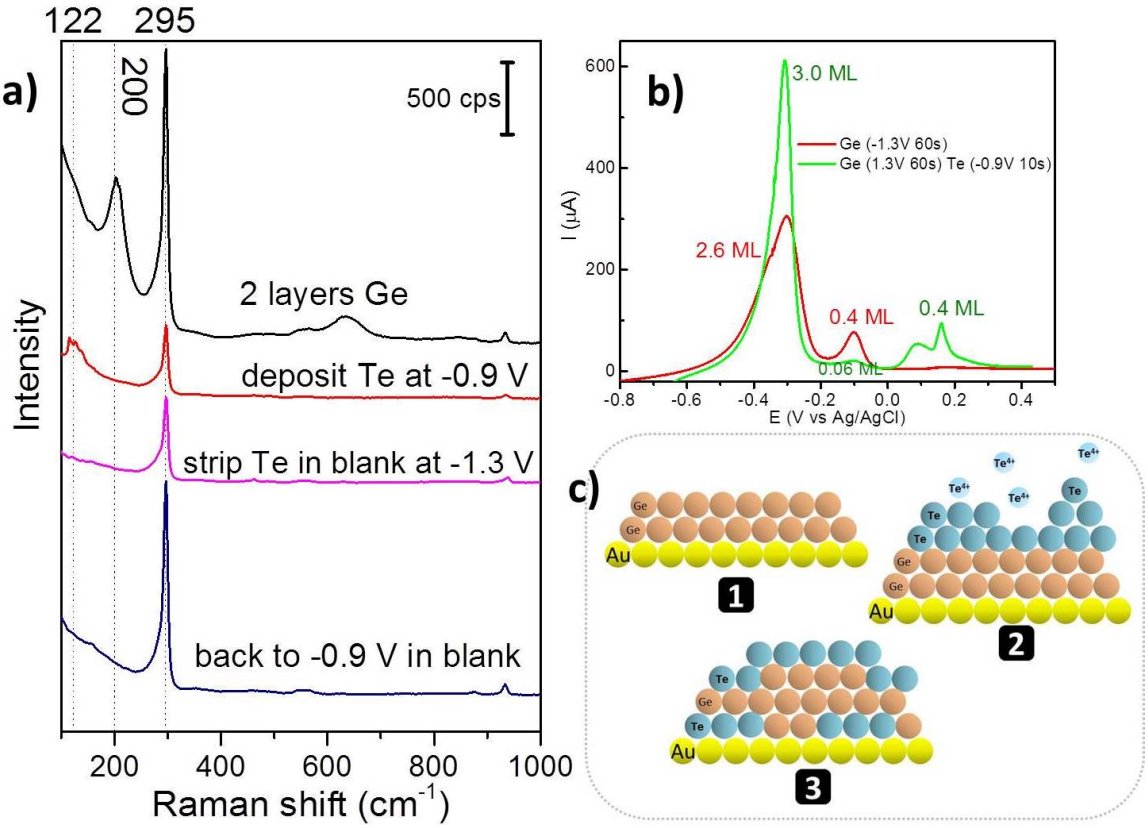

Figure 4.10: (a) Raman spectra obtained from each step in the bait and switch E-ALD cycle. Deposition of Te irreversibly removed the 200 cm^{-1} peak. (b) Voltammetric responses of Te depositing on a Ge covered Au substrate. Te displaced the first layer of Ge bonding to Au. The oxidation peak of Ge UPD at -0.15 V got significantly reduced when Te was present. (c) Schematic of how Te went underneath the Ge layers to bond with Au.

4.6 Acknowledgments

Support from the National Science Foundation, DMR # 1410109, is gratefully acknowledged. The research was in part carried out through the Joint Center for Artificial Photosynthesis at the California Institute of Technology, a DOE Energy Innovation Hub, supported through the Office of Science of the U.S. Department of Energy under Award Number DE-SC0004993, which provided support for Y.-G.K. and M.P.S. to perform the EC-STM experiments.

References

(1) Cahangirov, S.; Topsakal, M.; Akturk, E.; Sahin, H.; Ciraci, S. Two- and One-Dimensional Honeycomb Structures of Silicon and Germanium. *Physical Review Letters* **2009**, *102*.

(2) Lebegue, S.; Eriksson, O. Electronic structure of two-dimensional crystals from ab initio theory. *Physical Review B* **2009**, *79*.

(3) Acun, A.; Zhang, L.; Bampoulis, P.; Farmanbar, M.; van Houselt, A.; Rudenko, A. N.; Lingenfelder, M.; Brocks, G.; Poelsema, B.; Katsnelson, M. I.; Zandvliet, H. J. W. Germanene: the germanium analogue of graphene. *Journal of Physics-Condensed Matter* **2015**, *27*.

(4) Le Lay, G.; Salomon, E.; Angot, T.; Davila, M. E. Increasing the lego of 2D electronics materials: silicene and germanene, graphene's new synthetic cousins. *Micro- and Nanotechnology Sensors, Systems, and Applications Vii* **2015**, *9467*.

(5) Zhang, L.; Bampoulis, P.; van Houselt, A.; Zandvliet, H. J. W. Two-dimensional Dirac signature of germanene. *Applied Physics Letters* **2015**, *107*.

(6) Zhang, X.; Guo, Z. X.; Cao, J. X.; Xiao, S. G.; Ding, J. W. Atomic and electronic structures of silicene and germanene on GaAs(111). *Acta Physica Sinica* **2015**, *64*.

(7) Chen, M. X.; Zhong, Z.; Weinert, M. Designing substrates for silicene and germanene: First-principles calculations. *Physical Review B* **2016**, *94*.

(8) Chen, X. P.; Sun, X.; Jiang, J. K.; Liang, Q. H.; Yang, Q.; Meng, R. S. Electrical and Optical Properties of Germanene on Single-Layer BeO Substrate. *Journal of Physical Chemistry C* **2016**, *120*, 20350–20356.

(9) Fukaya, Y.; Matsuda, I.; Feng, B. J.; Mochizuki, I.; Hyodo, T.; Shamoto, S. Asymmetric structure of germanene on an Al(111) surface studied by total-reflection high-energy positron diffraction. *2d Materials* **2016**, *3*.

(10) Gou, J.; Zhong, Q.; Sheng, S. X.; Li, W. B.; Cheng, P.; Li, H.; Chen, L.; Wu, K. H. Strained monolayer germanene with 1 x 1 lattice on Sb(111). *2d Materials* **2016**, *3*.

(11) Si, C.; Liu, J. W.; Xu, Y.; Wu, J.; Gu, B. L.; Duan, W. H. Functionalized germanene as a prototype of large-gap two-dimensional topological insulators. *Physical Review B* **2014**, *89*.

(12) Ezawa, M. Monolayer Topological Insulators: Silicene, Germanene, and Stanene. *Journal of the Physical Society of Japan* **2015**, *84*.

(13) Goswami, P. Effect of disorder in the transition from topological insulator to valley-spin polarized state in silicene and Germanene. *Indian Journal of Physics* **2015**, *89*, 677–686.

(14) Huang, C. X.; Zhou, J.; Wu, H. P.; Deng, K. M.; Jena, P.; Kan, E. Quantum Phase Transition in Germanene and Stanene Bilayer: From Normal Metal to Topological Insulator. *Journal of Physical Chemistry Letters* **2016**, *7*, 1919–1924.

(15) Matthes, L.; Bechstedt, F. Influence of edge and field effects on topological states of germanene nanoribbons from self-consistent calculations. *Physical Review B* **2014**, *90*.

(16) Singh, N.; Schwingenschlogl, U. Topological phases of silicene and germanene in an external magnetic field: Quantitative results. *Physica Status Solidi-Rapid Research Letters* **2014**, *8*, 353–356.

(17) Ezawa, M. Photo-Induced Topological Superconductor in Silicene, Germanene, and Stanene. *Journal of Superconductivity and Novel Magnetism* **2015**, *28*, 1249–1253.

(18) Zhang, R. W.; Ji, W. X.; Zhang, C. W.; Li, S. S.; Li, P.; Wang, P. J. New family of room temperature quantum spin Hall insulators in two-dimensional germanene films. *Journal of Materials Chemistry C* **2016**, *4*, 2088–2094.

(19) Wang, Y. Y.; Li, J. Z.; Xiong, J. H.; Pan, Y. Y.; Ye, M.; Guo, Y.; Zhang, H.; Quhe, R.; Lu, J. Does the Dirac cone of germanene exist on metal substrates? *Physical Chemistry Chemical Physics* **2016**, *18*, 19451–19456.

(20) Ye, X. S.; Shao, Z. G.; Zhao, H. B.; Yang, L.; Wang, C. L. Intrinsic carrier mobility of germanene is larger than graphene's: first-principle calculations. *Rsc Advances* **2014**, *4*, 21216–21220.

(21) Nijamudheen, A.; Bhattacharjee, R.; Choudhury, S.; Datta, A. Electronic and Chemical Properties of Germanene: The Crucial Role of Buckling. *Journal of Physical Chemistry C* **2015**, *119*, 3802–3809.

(22) Scalise, E.; Houssa, M.; Pourtois, G.; van den Broek, B.; Afanas'ev, V.; Stesmans, A. Vibrational properties of silicene and germanene. *Nano Research* **2013**, *6*, 19–28.

(23) Bianco, E.; Butler, S.; Jiang, S. S.; Restrepo, O. D.; Windl, W.; Goldberger, J. E. Stability and Exfoliation of Germanane: A Germanium Graphane Analogue. *ACS Nano* **2013**, *7*, 4414–4421.

(24) Houssa, M.; Scalise, E.; Sankaran, K.; Pourtois, G.; Afanas'ev, V. V.; Stesmans, A. Electronic properties of hydrogenated silicene and germanene. *Applied Physics Letters* **2011**, *98*.

(25) Houssa, M.; Scalise, E.; van den Broek, B.; Pourtois, G.; Afanas'ev, V. V.; Stesmans, A. Interaction of Germanene With (0001)ZnSe Surfaces: A Theoretical Study. *Semiconductors, Dielectrics, and Metals for Nanoelectronics 11* **2013**, *58*, 209–215.

(26) Li, L. Y.; Zhao, M. W. First-principles identifications of superstructures of germanene on Ag(111) surface and h-BN substrate. *Physical Chemistry Chemical Physics* **2013**, *15*, 16853–16863.

(27) Yan, J. A.; Stein, R.; Schaefer, D. M.; Wang, X. Q.; Chou, M. Y. Electron-phonon coupling in two-dimensional silicene and germanene. *Physical Review B* **2013**, *88*.

(28) Kaloni, T. P. Tuning the Structural, Electronic, and Magnetic Properties of Germanene by the Adsorption of 3d Transition Metal Atoms. *Journal of Physical Chemistry C* **2014**, *118*, 25200–25208.

(29) Kaloni, T. P.; Schreckenbach, G.; Freund, M. S.; Schwingenschlogl, U. Current developments in silicene and germanene. *Physica Status Solidi-Rapid Research Letters* **2016**, *10*, 133–142.

(30) Huang, L. F.; Gong, P. L.; Zeng, Z. Phonon properties, thermal expansion, and thermomechanics of silicene and germanene. *Physical Review B* **2015**, *91*.

(31) Li, X. D.; Wu, S. Q.; Zhou, S.; Zhu, Z. Z. Structural and electronic properties of germanene/MoS2 monolayer and silicene/MoS2 monolayer superlattices. *Nanoscale Research Letters* **2014**, *9*.

(32) Zhang, L.; Bampoulis, P.; Rudenko, A. N.; Yao, Q.; van Houselt, A.; Poelsema, B.; Katsnelson, M. I.; Zandvliet, H. J. W. Structural and Electronic Properties of Germanene on MoS2. *Physical Review Letters* **2016**, *116*.

(33) Liang, P.; Liu, Y.; Xing, S.; Shu, H. B.; Tai, B. Electronic and magnetic properties of germanene: Surface functionalization and strain effects. *Solid State Communications* **2016**, *226*, 19–24.

(34) Padilha, J. E.; Pontes, R. B. Electronic and transport properties of structural defects in monolayer germanene: An ab initio investigation. *Solid State Communications* **2016**, *225*, 38–43.

(35) Pang, Q.; Li, L.; Zhang, C. L.; Wei, X. M.; Song, Y. L. Structural, electronic and magnetic properties of 3d transition metal atom adsorbed germanene: A first-principles study. *Materials Chemistry and Physics* **2015**, *160*, 96–104.

(36) Pang, Q.; Zhang, C. L.; Li, L.; Fu, Z. Q.; Wei, X. M.; Song, Y. L. Adsorption of alkali metal atoms on germanene: A first-principles study. *Applied Surface Science* **2014**, *314*, 15–20.

(37) Persichetti, L.; Jardali, F.; Vach, H.; Sgarlata, A.; Berbezier, I.; De Crescenzi, M.; Balzarotti, A. van der Waals Heteroepitaxy of Germanene Islands on Graphite. *Journal of Physical Chemistry Letters* **2016**, *7*, 3246–3251.

(38) Roome, N. J.; Carey, J. D. Beyond Graphene: Stable Elemental Monolayers of Silicene and Germanene. *ACS Applied Materials & Interfaces* **2014**, *6*, 7743–7750.

(39) Rupp, C. J.; Chakraborty, S.; Anversa, J.; Baierle, R. J.; Ahuja, R. Rationalizing the Hydrogen and Oxygen Evolution Reaction Activity of Two-Dimensional Hydrogenated Silicene and Germanene. *ACS Applied Materials & Interfaces* **2016**, *8*, 1536–1544.

(40) Trivedi, S.; Srivastava, A.; Kurchania, R. Silicene and Germanene: A First Principle Study of Electronic Structure and Effect of Hydrogenation-Passivation. *Journal of Computational and Theoretical Nanoscience* **2014**, *11*, 781–788.

(41) Gurel, H. H.; Ozcelik, V. O.; Ciraci, S. Effects of charging and perpendicular electric field on the properties of silicene and germanene. *Journal of Physics-Condensed Matter* **2013**, *25*.

(42) Ozcelik, V. O.; Durgun, E.; Ciraci, S. New Phases of Germanene. *Journal of Physical Chemistry Letters* **2014**, *5*, 2694–2699.

(43) Ozcelik, V. O.; Kecik, D.; Durgun, E.; Ciraci, S. Adsorption of Group IV Elements on Graphene, Silicene, Germanene, and Stanene: Dumbbell Formation. *Journal of Physical Chemistry C* **2015**, *119*, 845–853.

(44) Yang, K.; Cahangirov, S.; Cantarero, A.; Rubio, A.; D'Agosta, R. Thermoelectric properties of atomically thin silicene and germanene nanostructures. *Physical Review B* **2014**, *89*.

(45) Liu, G.; Liu, S. B.; Xu, B.; Ouyang, C. Y.; Song, H. Y. First-principles study of the stability of free-standing germanene in oxygen atmosphere. *Journal of Applied Physics* **2015**, *118*.

(46) Tomberli, B.; Rahemtulla, A.; Kim, E.; Roorda, S.; Kycia, S. Germanene-like defects in amorphous germanium revealed by three-dimensional visualization of high-resolution pair-distribution functions. *Physical Review B* **2015**, *92*.

(47) Ge, X. J.; Yao, K. L.; Lu, J. T. Comparative study of phonon spectrum and thermal expansion of graphene, silicene, germanene, and blue phosphorene. *Physical Review B* **2016**, *94*.

(48) Kuang, Y. D.; Lindsay, L.; Shi, S. Q.; Zheng, G. P. Tensile strains give rise to strong size effects for thermal conductivities of silicene, germanene and stanene. *Nanoscale* **2016**, *8*, 3760–3767.

(49) Marjaoui, A.; Stephan, R.; Hanf, M. C.; Diani, M.; Sonnet, P. Tailoring the germanene-substrate interactions by means of hydrogenation. *Physical Chemistry Chemical Physics* **2016**, *18*, 15667–15672.

(50) Mortazavi, B.; Dianat, A.; Cuniberti, G.; Rabczuk, T. Application of silicene, germanene and stanene for Na or Li ion storage: A theoretical investigation. *Electrochimica Acta* **2016**, *213*, 865–870.

(51) Tahir, M.; Zhang, Q. Y.; Schwingenschlogl, U. Floquet edge states in germanene nanoribbons. *Scientific Reports* **2016**, *6*.

(52) Zhao, J.; Zeng, H. Chemically functionalized germanene for spintronic devices: a first-principles study. *Physical Chemistry Chemical Physics* **2016**, *18*, 9809–9815.

(53) Zhou, S.; Zhao, J. J. Electronic Structures of Germanene on MoS2: Effect of Substrate and Molecular Adsorption. *Journal of Physical Chemistry C* **2016**, *120*, 21691–21698.

(54) Hattori, A.; Tanaya, S.; Yada, K.; Araidai, M.; Sato, M.; Hatsugai, Y.; Shiraishi, K.; Tanaka, Y. Edge states of hydrogen terminated monolayer materials: silicene, germanene and stanene ribbons. *Journal of Physics-Condensed Matter* **2017**, *29*.

(55) Qin, Z. H.; Pan, J. B.; Lu, S. Z.; Yan, S.; Wang, Y. L.; Du, S. X.; Gao, H. J.; Cao, G. Y. Direct Evidence of Dirac Signature in Bilayer Germanene Islands on Cu(111). *Advanced Materials* **2017**, *29*.

(56) Shih, P. H.; Chiu, Y. H.; Wu, J. Y.; Shyu, F. L.; Lin, M. F. Coulomb excitations of monolayer germanene. *Scientific Reports* **2017**, *7*.

(57) Wang, X. Q.; Wu, Z. G. Intrinsic magnetism and spontaneous band gap opening in bilayer silicene and germanene. *Physical Chemistry Chemical Physics* **2017**, *19*, 2148–2152.

(58) Bechstedt, F.; Matthes, L.; Gori, P.; Pulci, O. Infrared absorbance of silicene and germanene. *Applied Physics Letters* **2012**, *100*.

(59) Matthes, L.; Gori, P.; Pulci, O.; Bechstedt, F. Universal infrared absorbance of two-dimensional honeycomb group-IV crystals. *Physical Review B* **2013**, *87*.

(60) Matthes, L.; Pulci, O.; Bechstedt, F. Optical properties of two-dimensional honeycomb crystals graphene, silicene, germanene, and tinene from first principles. *New Journal of Physics* **2014**, *16*.

(61) Zhang, R. W.; Zhang, C. W.; Ji, W. X.; Li, F.; Ren, M. J.; Li, P.; Yuan, M.; Wang, P. J. Tunable electronic properties in the van der Waals heterostructure of germanene/germanane. *Physical Chemistry Chemical Physics* **2015**, *17*, 12194–12198.

(62) Bampoulis, P.; Zhang, L.; Safaei, A.; van Gastel, R.; Poelsema, B.; Zandvliet, H. J. W. Germanene termination of Ge2Pt crystals on Ge(110). *Journal of Physics-Condensed Matter* **2014**, *26*.

(63) Derivaz, M.; Dentel, D.; Stephan, R.; Hanf, M. C.; Mehdaoui, A.; Sonnet, P.; Pirri, C. Continuous Germanene Layer on Al (111). *Nano Letters* **2015**, *15*, 2510–2516.

(64) Stephan, R.; Hanf, M. C.; Derivaz, M.; Dentel, D.; Asensio, M. C.; Avila, J.; Mehdaoui, A.; Sonnet, P.; Pirri, C. Germanene on Al(111): Interface Electronic States and Charge Transfer. *Journal of Physical Chemistry C* **2016**, *120*, 1580–1585.

(65) Li, L. F.; Lu, S. Z.; Pan, J. B.; Qin, Z. H.; Wang, Y. Q.; Wang, Y. L.; Cao, G. Y.; Du, S. X.; Gao, H. J. Buckled Germanene Formation on Pt(111). *Advanced Materials* **2014**, *26*, 4820–+.

(66) Tsai, H. S.; Chen, Y. Z.; Medina, H.; Su, T. Y.; Chou, T. S.; Chen, Y. H.; Chueh, Y. L.; Liang, J. H. Direct formation of large-scale multi-layered germanene on Si substrate. *Physical Chemistry Chemical Physics* **2015**, *17*, 21389–21393.

(67) Davila, M. E.; Le Lay, G. Few layer epitaxial germanene: a novel two-dimensional Dirac material. *Scientific Reports* **2016**, *6*.

(68) Davila, M. E.; Xian, L.; Cahangirov, S.; Rubio, A.; Le Lay, G. Germanene: a novel two-dimensional germanium allotrope akin to graphene and silicene. *New Journal of Physics* **2014**, *16*.

(69) Szekely, G. Electrodeposition of Germanium. *Journal of the Electrochemical Society* **1951**, *98*, 318–324.

(70) Al-Salman, R.; Mallet, J.; Molinari, M.; Fricoteaux, P.; Martineau, F.; Troyon, M.; El Abedin, S. Z.; Endres, F. Template assisted electrodeposition of germanium and silicon nanowires in an ionic liquid. *Physical Chemistry Chemical Physics* **2008**, *10*, 6233–6237.

(71) Chandrasekharan, N.; Sevov, S. C. Anodic Electrodeposition of Germanium Films from Ethylenediamine Solutions of Deltahedral Ge-9(4-) Zintl Ions. *Journal of the Electrochemical Society* **2010**, *157*, C140–C145.

(72) Liang, X. H.; Jayaraju, N.; Thambidurai, C.; Zhang, Q. H.; Stickney, J. L. Controlled Electrochemical Formation of GexSbyTez using Atomic Layer Deposition (ALD). *Chemistry of Materials* **2011**, *23*, 1742–1752.

(73) Liang, X. H.; Kim, Y. G.; Gebergziabiher, D. K.; Stickney, J. L. Aqueous Electrodeposition of Ge Monolayers. *Langmuir* **2010**, *26*, 2877–2884.

(74) Liang, X. H.; Zhang, Q. H.; Lay, M. D.; Stickney, J. L. Growth of Ge Nanofilms Using Electrochemical Atomic Layer Deposition, with a "Bait and Switch" Surface-Limited Reaction. *Journal of the American Chemical Society* **2011**, *133*, 8199–8204.

(75) Cummings, C. Y.; Bartlett, P. N.; Pugh, D.; Reid, G.; Levason, W.; Hasan, M. M.; Hector, A. L.; Spencer, J.; Smith, D. C. Supercritical Fluid Electrodeposition of Elemental Germanium onto Titanium Nitride Substrates. *Journal of the Electrochemical Society* **2015**, *162*, D619–D624.

(76) Cummings, C. Y.; Bartlett, P. N.; Pugh, D.; Reid, G.; Levason, W.; Hasan, M. M.; Hector, A. L.; Spencer, J.; Smith, D. C.; Marks, S.; Beanland, R. Electrodeposition of Protocrystalline Germanium from Supercritical Difluoromethane. *Chemelectrochem* **2016**, *3*, 726–733.

(77) Ke, J.; Bartlett, P. N.; Cook, D.; Easun, T. L.; George, M. W.; Levason, W.; Reid, G.; Smith, D.; Su, W. T.; Zhang, W. J. Electrodeposition of germanium from supercritical fluids. *Physical Chemistry Chemical Physics* **2012**, *14*, 1517–1528.

(78) Lahiri, A.; El Abedin, S. Z.; Endres, F. UV-Assisted Electrodeposition of Germanium from an Air- and Water-Stable Ionic Liquid. *Journal of Physical Chemistry C* **2012**, *116*, 17739–17745.

(79) Wu, M. X.; Brooks, N. R.; Schaltin, S.; Binnemans, K.; Fransaer, J. Electrodeposition of germanium from the ionic liquid 1-butyl-1-methylpyrrolidinium dicyanamide. *Physical Chemistry Chemical Physics* **2013**, *15*, 4955–4964.

(80) Wu, M. X.; Vanhoutte, G.; Brooks, N. R.; Binnemans, K.; Fransaer, J. Electrodeposition of germanium at elevated temperatures and pressures from ionic liquids. *Physical Chemistry Chemical Physics* **2015**, *17*, 12080–12089.

(81) Fahrenkrug, E.; Gu, J. S.; Jeon, S.; Veneman, P. A.; Goldman, R. S.; Maldonado, S. Room-Temperature Epitaxial Electrodeposition of Single-Crystalline Germanium Nanowires at the Wafer Scale from an Aqueous Solution. *Nano Letters* **2014**, *14*, 847–852.

(82) Endres, F. Electrodeposition of a thin germanium film on gold from a room temperature ionic liquid. *Physical Chemistry Chemical Physics* **2001**, *3*, 3165–3174.

(83) Endres, F. The electrodeposition of germanium from an ionic liquid: A mini-review on the nanoscale processes. *Physical Chemistry Chemical Physics* **2002**, *2002*, 677–689.

(84) Endres, F. Electrodeposition of nanosized germanium from GeBr4 and GeCl4 in an ionic liquid. *Electrochemical and Solid State Letters* **2002**, *5*, C38–C40.

(85) Endres, F.; El Abedin, S. Z. Electrodeposition of stable and narrowly dispersed germanium nanoclusters from an ionic liquid. *Chemical Communications* **2002**, 892–893.

(86) Endres, F.; El Abedin, S. Z. Nanoscale electrodeposition of germanium on Au(111) from an ionic liquid: an in situ STM study of phase formation - Part I. Ge from GeBr4. *Physical Chemistry Chemical Physics* **2002**, *4*, 1640–1648.

(87) Vanduyne, R. P.; Haushalter, J. P. Surface-Enhanced Resonance Raman-Spectroscopy of Adsorbates on Semiconductor Electrode Surfaces - Tris (Bipyridine) Ruthenium(II) Adsorbed on Silver-Modified N-GaAs(100). *Journal of Physical Chemistry* **1983**, *87*, 2999–3003.

(88) Zou, S. Z.; Weaver, M. J. Surface-enhanced Raman scattering of ultrathin cadmium chalcogenide films on gold formed by electrochemical atomic-layer epitaxy: Thickness-dependent phonon characteristics. *Journal of Physical Chemistry B* **1999**, *103*, 2323–2326.

(89) Gichuhi, A.; Boone, B. E.; Shannon, C. Resonance Raman scattering and scanning tunneling spectroscopy of CdS thin films grown by electrochemical atomic layer epitaxy - thickness dependent phonon and electronic properties. *Journal of Electroanalytical Chemistry* **2002**, *522*, 21–25.

(90) McFarland, A. D.; Young, M. A.; Dieringer, J. A.; Van Duyne, R. P. Wavelength-scanned surface-enhanced Raman excitation spectroscopy. *Journal of Physical Chemistry B* **2005**, *109*, 11279–11285.

(91) Rath, S.; Sen, S.; Nozaki, S.; Tona, M.; Ohtani, S.; Jain, K. P. Detection of Low-Density Ge Nanoparticles Using Surface-Enhanced Raman Spectroscopy. *Advanced Science Letters* **2009**, *2*, 377–380.

(92) Carim, A. I.; Gu, J. S.; Maldonado, S. Overlayer Surface-Enhanced Raman Spectroscopy for Studying the Electrodeposition and Interfacial Chemistry of Ultrathin Ge on a Nanostructured Support. *ACS Nano* **2011**, *5*, 1818–1830.

(93) Abdelsalam, M. E.; Bartlett, P. N.; Baumberg, J. J.; Cintra, S.; Kelf, T. A.; Russell, A. E. Electrochemical SERS at a structured gold surface. *Electrochemistry Communications* **2005**, *7*, 740–744.

(94) Mahajan, S.; Baumberg, J. J.; Russell, A. E.; Bartlett, P. N. Reproducible SERRS from structured gold surfaces. *Physical Chemistry Chemical Physics* **2007**, *9*, 6016–6020.

Chapter 5

Conclusion and Future Studies

In the introduction chapter, a short overview of E-ALD was provided, in addition to a discussion about the flow cell system and some important characterization techniques such as EC-STM and *in situ* SERS. The motivation behind E-ALD is that it offers an attractive low-cost, yet comparable deposit quality alternative to the gas-phase methodology such as molecular beam epitaxy and chemical vapor deposition. The development of E-ALD and the optimization of its instrumental set up over the last 27 years have made the study of the electrodeposition of a wide range of materials possible.[1–8] Recently, a new variant of E-ALD, called PP-ALD, was derived to improve the deposition rate.[9,10]

Chapter 2 presented the study about the electrodeposition of ZnS nanofilms using PP-ALD. The method PP-ALD is a subset of E-ALD where the electrochemical surface-limited reaction, called underpotential deposition (UPD), of each element is preserved by pulsing the potential rather than exchanging solution. The chemistry to form ZnS from Zn^{2+} and thiosulfate ion was proven to be feasible, thus promising a common route to grow other similar binary compounds such as SnS and CuS. For example, the combination between Sn and thiosulfate is deemed to be more complicated because of Sn's stability in solution. According to the Pourbaix diagram, Sn will form a passivation layer of SnO_2 at pH 3-9, where thiosulfate would be stable. Precipitation of Sn can happen at pH as acidic as 1, where Sn solution is already considered most stable. Any pHs higher than 1 would result in an instant precipitation

of Sn. The chemistry of Sn thus requires working with some complexing agents such as citrate or EDTA, if a PP-ALD process were to be realized for Sn and thiosulfate.

The chemistry of ZnS should eventually be combined with other binary compounds to form CZTS. While the Sn and Se/S system is still being developed, the binary compound CuSe has been studied previously.[10] The chemistry to form CuSe is straightforward where Cu and Se are first codeposited cathodically following by an oxidative potential to strip off any excess Cu. No known instability was observed with CuSe. The ZnS system, however, seems to dissolve in acidic solution (pH $\sim$ 1). Therefore, to combine their chemistry together, the CuSe system should be maintained at pH $\sim$ 5 where it is considered optimal for ZnS to grow.

Chapter 3 highlighted the use of EC-STM to study the electrodeposition of germanene. Near atomic resolution of germanene's characteristic honeycomb structure was observed. The precursor stage seems to vary with pH. At pH 9.0, germanene initially deposits in the fcc region of the Au reconstruction, after which the surface is relaxed and the remaining HB lines are displaced by Ge atoms. The electrodeposition of germanene results in a large coverage containing some small domains with average size of 2-3 nm. Defects are observed between domain walls where ring structures other than 6-member can form. Exposure to a 780 nm laser at 8 mW, 3.1 µm spot size, can crystallize the surface and form the Raman peak signature of germanene at 295 cm^{-1}.

Chapter 4 examined the growth of germanene using both *in situ* SERS and EC-STM. Compare to EC-STM, Raman spectroscopy is a much more versatile method that can provide instant information on the vibrational modes of the bonding in the material. The enhancement effect from the SERS substrate makes it possible to detect signal from feature as little as a single atomic layer of germanene. Due to its interaction with the Au substrate, the first layer germanene adopts a different vibration mode from the second layer. Hydrogen evolution can significantly reduce the intensity of the second layer peak at 295 cm^{-1} while completely remove the first

layer peak at 200 cm^{-1}, suggesting that the deposit might be lifted off the surface at negative potential. Without protection from the second layer, the first layer can be irreversibly removed from the surface in hydrogen evolution region. When Te went underneath layers of Ge to bond with Au substrate, the peak for the first layer at 200^{-1} has permanently disappear.

EC-STM image of an annealed surface has yet been achieved. The challenge with such experiment is the thermal drift that occurs after the surface is crystalized with the laser. There are some evidences that part of the crystallization process was due to the heating effect. Designing such experiment requires setting up a 780 nm laser with enough power density to incident on the Au(111) facet of the Au bead. Afterward, the system needs to cool down sufficiently before engaging the tip to start imaging.

So far, germanene seems to only be stable in solution with potential control. In order for it to become applicable to material integration, its chemical and structural stability must be studied. UHV-EC is a set up that can be used to analyze electrodeposited thin films without contamination from air exposure. Germanene layers can be formed electrochemically in an antechamber that is filled with Ar gas. The antechamber is then pumped down with cryosorption pumps in order to be open to the UHV main chamber. The sample can be transferred to the main chamber for analysis with LEED, Auger and XPS. The antechamber can be designed so that a 780 nm laser can be focused onto the sample to anneal the surface before transferring to the main chamber. Once the surface is crystallized, the LEED pattern can be obtained to deduce the structural arrangement of the first germanene layer with respect to the Au substrate underneath. XPS can be used to study its susceptibility to oxidation over time.

Cyclic voltammetry shows that the last Ge oxidation peak occurs at -0.15 V, but both Raman spectra and EC-STM images suggest that Ge remain on the surface at potential as positive as 0.1 V. Those Ge species that hang around the surface can

be analyzed with XPS, as their chemical shift contains information on how much the layers have been oxidized after being removed from Au.

The photochemistry that occurs on germanene is not well understood. Some questions remaining include why the 531 nm laser with the same power density cannot perform the annealing effect as the 780 nm laser, and how much thermal energy from the absorption is contributing to the crystallization. The Raman peak of the first layer is also red-shifted to a lower vibrational mode, compared to a calculated free-standing sheet of germanene. These questions could be more clarified by using a different SERS substrate from Au, such as Cu. The vibrational mode of the first layer can be different on Cu than on Au, but the second layer should remain at the same place. Hydrogen overpotential is also higher on Cu than on Au, making the effect of hydrogen bubble formation due to photochemistry less likely.

Reflectance measurements can be used to potentially explore the optical properties of germanene. A tentative set up is illustrated in Figure 5.1. The reflectance of pure Au SERS substrate is first measured, then Ge is deposited at different potentials (-0.9 V, -1.0 V, and -1.1 V) to compare how much light is absorbed by the Ge layers. This assumes any unabsorbed light would reflect to the Si detector, but effect from the light scattering should also be taken into account in data interpretation. The light penetration depth is expectedly not surface sensitive. Therefore, variation in reflectivity from the Au substrate should also be considered. The current output from the Si detector is connected to a photocurrent measurement circuit before entering the lock-in-amplifier. The light is chopped to modulate only the effect due to the light source.

Thicker Ge films deposited using Bait and Switch E-ALD have been performed on Cu substrates.[11] However, majority of the spots exhibit only an amorphous Ge peak at 270 cm^{-1}. It is proposed here to subsequently anneal the surface with 780 nm laser for every cycle of E-ALD. This could potentially result in a crystalline

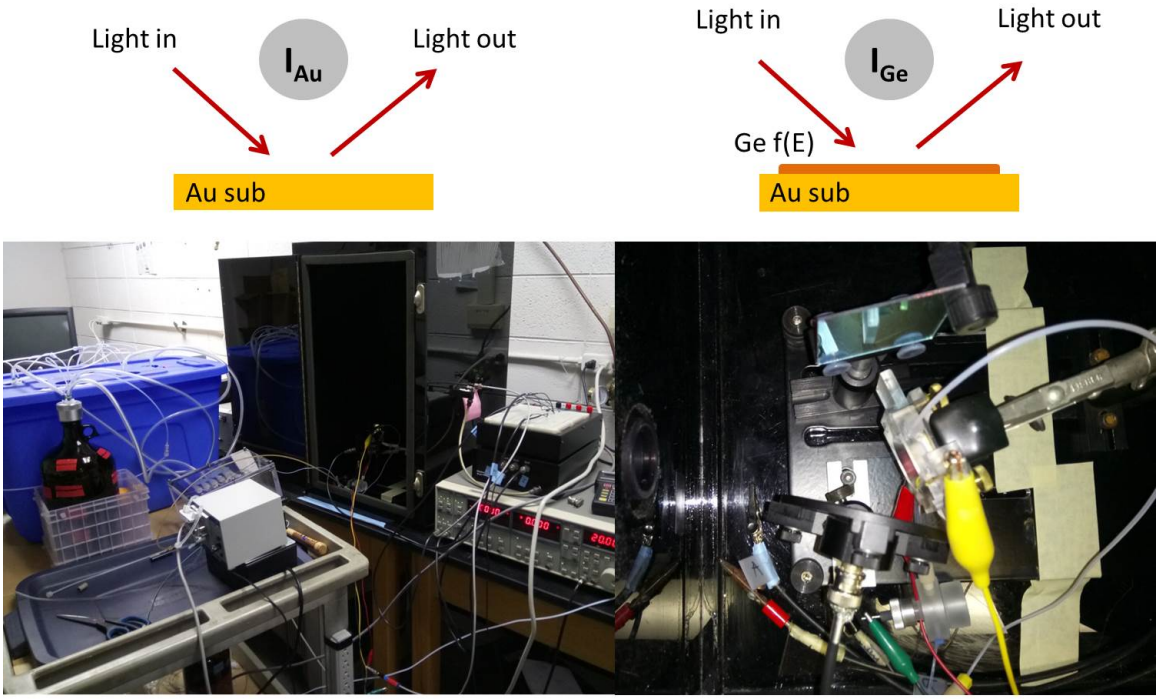

Figure 5.1: Reflectance measurements of Ge layers

deposit of multiplayers Ge films. Once thicker deposit is formed, it can be conveniently characterized with diffraction techniques such as XRD and TEM to understand its crystallinity, diffraction pattern, and potentially layered structure. One foreseeable challenge with this experiment is that when Te is reductively stripped off the surface, Te rings are observed to stick around, as indicated by the Raman peak at 122 cm^{-1} and the appearance of some floating amorphous features under the optical microscope. These Te rings can also be annealed by the laser as the 122 cm^{-1} peak gets sharper with more laser exposure. Moreover, Te's removal from underneath can be random and thus disruptive to the layer of Ge formed in earlier step. The formation of germanane, the hydrogenated form of germanene, has yet been intensively studied, partially due to the lack of theoretical information on its vibrational modes. In his report, Carim et al. has discussed a possible formation of GeH_x during the electrodeposition at negative potential ($<$ 1.0 V vs Ag/AgCl), observed by *in situ* SERS.[12] However, some of those Raman peaks between 1800 and 2000 cm^{-1} suggestive of germanane were not observed in the studies presented in Chapter 4. The lack of such peaks does not necessarily indicate that GeH_x is not forming at these conditions. There might have been some subtle differences in the experimental set up, thus more investigations are needed to better understand the behavior of Ge at more negative potentials.

References

(1) Gregory, B. W.; Stickney, J. L. Electrochemical Atomic Layer Epitaxy (ECALE). *Journal of Electroanalytical Chemistry* **1991**, *300*, 543–561.

(2) Villegas, I.; Stickney, J. L. Preliminary Studies of Gaas Deposition on Au(100), (110), and (111) Surfaces by Electrochemical Atomic Layer Epitaxy. *Journal of the Electrochemical Society* **1992**, *139*, 686–694.

(3) Colletti, L. P.; Teklay, D.; Stickney, J. L. Thin-Layer Electrochemical Studies of the Oxidative Underpotential Deposition of Sulfur and Its Application to the Electrochemical Atomic Layer Epitaxy Deposition of Cds. *Journal of Electroanalytical Chemistry* **1994**, *369*, 145–152.

(4) Colletti, L. P.; Stickney, J. L. Optimization of the growth of CdTe thin films formed by electrochemical atomic layer epitaxy in an automated deposition system. *Journal of the Electrochemical Society* **1998**, *145*, 3594–3602.

(5) Venkatasamy, V.; Jayaraju, N.; Cox, S. M.; Thambidurai, C.; Mathe, M.; Stickney, J. L. Deposition of HgTe by electrochemical atomic layer epitaxy (EC-ALE). *Journal of Electroanalytical Chemistry* **2006**, *589*, 195–202.

(6) Venkatasamy, V.; Jayaraju, N.; Cox, S. M.; Thambidurai, C.; Stickney, J. L. Studies of Hg((1-x))Cd(x)Te formation by electrochemical atomic layer deposition and investigations into bandgap engineering. *Journal of the Electrochemical Society* **2007**, *154*, H720–H725.

(7) Kim, J. Y.; Stickney, J. L. Ultrahigh vacuum surface studies of the electrochemical atomic layer deposition of indium telluride on n-type GaAs(100). *Journal of Physical Chemistry C* **2008**, *112*, 5966–5971.

(8) Gebregziabiher, D. K.; Kim, Y. G.; Thambidurai, C.; Ivanova, V.; Haumesser, P. H.; Stickney, J. L. Electrochemical atomic layer deposition of copper nanofilms on ruthenium. *Journal of Crystal Growth* **2010**, *312*, 1271–1276.

(9) Czerniawski, J. M.; Stickney, J. L. Electrodeposition of In_2Se_3 Using Potential Pulse Atomic Layer Deposition. *Chemistry of Materials* **2016**.

(10) Czerniawski, J. M.; Perdue, B. R.; Stickney, J. L. Potential Pulse Atomic Layer Deposition of Cu_2Se. *Chemistry of Materials* **2016**, *28*, 583–591.

(11) Liang, X. H.; Kim, Y. G.; Gebergziabiher, D. K.; Stickney, J. L. Aqueous Electrodeposition of Ge Monolayers. *Langmuir* **2010**, *26*, 2877–2884.

(12) Carim, A. I.; Gu, J. S.; Maldonado, S. Overlayer Surface-Enhanced Raman Spectroscopy for Studying the Electrodeposition and Interfacial Chemistry of Ultrathin Ge on a Nanostructured Support. *ACS Nano* **2011**, *5*, 1818–1830.